The Pennsylvania State University
The Graduate School
College of Engineering

ACTIVE ENERGY HARVESTING FOR PIEZOELECTRIC DYNAMIC SYSTEMS

A Dissertation in
Electrical Engineering
by
Cheng Luo

Submitted in Partial Fulfillment
of the Requirements
for the Degree of

Doctor of Philosophy

May 2010

The dissertation of Cheng Luo was reviewed and approved* by the following:

Heath F. Hofmann
Associate Professor of Electrical Engineering
Dissertation Advisor, Chair of Committee

Jeffrey S. Mayer
Associate Professor of Electrical Engineering

Qiming Zhang
Professor of Electrical Engineering

John D. Mitchell
Professor of Electrical Engineering

George A. Lesieutre
Professor of Aerospace Engineering

Kenneth Jenkins
Professor of Electrical Engineering
Head of Electrical Engineering

*Signatures are on file in the Graduate School.

Abstract

Interest in the use of piezoelectric materials for electrical energy generation has increased over the years. The interface circuit between the piezoelectric device and electrical load plays an important role in the energy harvesting process. Most of the previous techniques are mainly passive, based on AC-DC diode-bridge rectifier circuits. However, since the diode-bridge rectifier circuit can only emulate a resistive load, while the internal impedance of a piezoelectric device is essentially capacitive, the impedance matching condition can not be satisfied, and so generally the power harvesting ability of the passive technique is very low. The semi-active techniques represented by the synchronized switch harvesting on inductor(SSHI) technique improves performance over the passive techniques by inverting the piezoelectric voltage in phase with the device velocity, but its performance drops dramatically at off-resonance frequencies because it does not guarantee impedance matching at off-resonance frequencies. The newly proposed active energy harvesting technique actively applies electrical boundary conditions to the piezoelectric device, and experimental results showed that the active technique can boost the harvested power dramatically under quasi-static conditions.

In previous work, the active energy harvesting experiments were all implemented under the quasi-static assumption, and the device displacement was assumed to be constant regardless of the applied voltage. However, in many practical applications, especially systems where the energy harvesting device possesses resonance frequency, the quasi-static assumption does not hold. Furthermore, the resonance frequency of a mechanical system is often changing and hard to estimate because of the variation of device parameters, and so previous techniques based on certain resonance frequencies may not be effective. Also, for a practical system, it is more likely that the excitation force instead of the displacement is fixed. Hence we seek to develop a more practical active energy harvesting technique for a real dynamic system application.

In this dissertation, the active energy harvesting technique for a spring-mass-damper piezoelectric dynamic system under a constant-magnitude force excitation is investigated. First the model of a piezoelectric dynamic system is built, and from this model we derive a general expression for the harvested power. It is shown that the harvested power is proportional to the integral of the product of the device voltage and velocity, and the optimal control voltage that results in maximum energy harvesting is derived. It is also shown that for any excitation frequency, the optimal control voltage is always trying to shift the system's resonance frequency to the excitation frequency, and the equivalent load impedance matches the internal impedance of the electromechanical system. The harvested power can therefore always be maximized at any excitation frequency. Simulation results are shown to prove the theory.

In practical implementation, the circuit efficiency and change of device parameters make the situation much more complicated, and the theoretically predicted optimal control voltage may not be accurate. We propose an adaptive control algorithm that can find the optimal control voltage adaptively. The method is based on sequential quadratic interpolation, and only information that can be easily measured from the circuit is needed to implement the control. Simulation results show good behavior of the controller.

Circuits used to implement the active harvesting technique are proposed, including a full-bridge converter with a flyback converter, dead-time insertion circuit, current and voltage regulator, current and voltage sensing circuit, PWM and drive signal generation circuit, etc. All the circuits are built on a stand-alone PCB board. Experimental results show that the active technique can harvest five times more power than the passive technique at off-resonance frequencies.

Table of Contents

List of Figures

List of Tables

Acknowledgments

I would like to express my sincere appreciation to my adviser Dr. Heath Hofmann for his guidance and support to me. It was him who brought me to the field of power electronics and energy harvesting in which I am most interested. His knowledgable research experiences and rigorous research attitude benefit me for my entire study and research.

I greatly appreciate all my committee members for their help and support to my work. Especially, I am very thankful to Dr. George Lesieutre and his graduate student Jeffrey Kauffman from Aerospace Engineering for their great help on the mechanical system setup and measurements, without them I can not get a good understanding of the mechanical system. I am also grateful to Dr. Jeffrey Mayer for his help on the implementation of the adaptive algorithm on MATLAB Simulink, Dr. John Mitchell for his review and suggestion of the dissertation, and Dr. Qiming Zhang for his guidance on the mechanical analysis.

I would like to thank my previous labmates Geng Tian, Dr. Guanghui Wang, and Dr. Yiming Liu for their help in various aspects. Dr. Yiming Liu and Geng Tian's previous work on quasi-static energy harvesting is an important foundation for this work. Dr. Guanghui Wang's skilled knowledge and experiences helped me greatly in the circuit design. I can not go so far without their help.

Finally I want to say thank you to my parents and my girlfriend Shan for their continuous love, support and help for my entire life all these years. I am reminded all the time that the research is not all that important.

Chapter 1

Introduction

1.1 Motivation

Electrical energy harvesting is the generation of electrical energy/power from ambient energy sources. There are many types of energy sources, such as solar, thermal gradient, tide, .etc, but a common ambient energy source is mechanical motion. In practice, resonance spring-mass systems are often employed to enhance the magnitude of the ambient mechanical motion. For applications using mechanical motion, certain forms of electromechanical energy conversion are necessary to generate the electrical energy, one of which could be the electro-active materials, particularly materials processing piezoelectric property, or piezoelectric materials. Such materials will generate a electric field, and hence a voltage for an applied force, and conversely, the application of a voltage to piezoelectric materials will cause them to change size (i.e., strain) in proportion to the applied voltage.

Interest in the use of piezoelectric materials for energy generation has increased over the years. With the simultaneous decrease in size and power requirements for microelectronics, it is conceivable that some circuits could be powered by extracting energy directly from the environment in which the circuit operates. There are many ways to extract ambient energy, but piezoelectric systems do so by conversion of mechanical energy. Excitations could be in the form of applied load, pressure, or vibration. Some example applications for which this has been studied include various loading conditions, such as impact (Xu et. al., 1996, 1998), resonance (Goldfarb and Jones, 1999), human movement (Schmidt, 1992; Kymissis et. al.,

1998; Shenck, 1998), and acoustic energy (Mandurino et. al., 2001) [3] [4] [5] [6] [7]. Some other applications of the piezoelectric energy harvesting can also be found in [8] [9] [10] [11] [12] [13] [14] [15] [16] [17]. Moreover, piezoelectric devices also feature vibration damping capability during energy harvesting, as described in [18] [19] [20] [21].

Researchers and engineers have made enormous progress in energy harvesting technologies in the last decade, including new active materials [22] [23] [24] [25] [25], better device design [11] [26] [27] [28] [29] [30], new circuits and controls [30] [31] [32] [33] [34] [35] [36] [37] [38] [39] [40] [41] [42](passive techniques) [43] [44] [45] [46] [47] [48](semi-active techniques) [22] [23] [1] [2] [49] (active techniques) , and new energy storage devices [50]. However, current technologies still do not meet the requirements of many demanding applications, such as harvesting power from low mechanical vibrations. First, the current technologies do not generate enough power, especially under size and weight restrictions. Second, for a vibration power harvester with a mechanical resonance, the power harvesting bandwidth is usually narrowed down to a few Hz around its resonance frequency, and a slight frequency shift results in a steep power output reduction.

The interface circuit between the piezoelectric device and electrical load plays an important role in the energy harvesting process. In both academia and industry, the predominant energy harvesting circuits under investigation are based on the passive AC-DC diode-rectifier circuit and the semi-active SSHI (synchronized switch harvesting on inductor) circuit. Research on active energy harvesting has not been established as one of the major research topics. The advantages of active energy harvesting lie in the fact that it can push the harvested energy to the limits of the piezoelectric devices by applying appropriate boundary conditions, and the benefits are even more apparent when the mechanical system is driven at an excitation frequency that differs from its resonance frequency. Liu et. al. first systematically studied the active energy harvesting approaches from mechanical excitations using piezoelectric and electrostrictive materials in [1]. Tian et. al. experimentally implemented the active energy technique to harvest electric power from a PVDF material using an ultra-low-power stand-alone interface circuit under quasi-static assumptions in [2] [49].

In previous work, the active energy harvesting experiments were all imple-

mented under the quasi-static assumption. However, in many practical applications, especially systems where the device possesses a mechanical resonance frequency, the quasi-static assumption does not hold. Furthermore, the resonance frequency of a mechanical dynamic system is often changing and hard to estimate because of the variation of device parameters, so previous techniques based on a certain resonance frequency may not be effective. Moreover, in previous techniques the device displacement is often assumed to be fixed regardless of the applied voltage. However, in a real dynamic system a more appropriate assumption should be that the external excitation force to the system is fixed. In this case, the control algorithm will be much different. We seek to develop a more practical active energy harvesting technique for a real piezoelectric dynamic system.

In this dissertation, we focus on a dynamic spring-mass-damper piezoelectric energy harvesting system that is externally excited by a constant-magnitude sinusoidal force. The mechanical and electrical models for the piezoelectric dynamic system are first derived, then the active energy harvesting technique for the dynamic system is developed, and adaptive control algorithms that maximize the harvested energy with information that can be easily obtained from the circuit are proposed. Finally the circuit implementation of the active technique is developed and the experimental results are shown to verify the theory.

1.2 Thesis Overview

Chapter 2 contains the introduction and analysis of the piezoelectric devices, focusing on the constitutive model and the equivalent electrical model of the piezoelectric devices under both quasi-static and dynamic conditions. The identification of the parameters for a dynamic system is then derived based on short-circuit and open-circuit tests.

Chapter 3 reviews the existing energy harvesting techniques for piezoelectric dynamic systems. The general mathematical expression for harvested energy is derived. Previous passive, semi-active, and active techniques are analyzed and compared to each other. The principle of the active energy harvesting technique is introduced in detail.

Chapter 4 develops the active energy harvesting technique for a piezoelectric

dynamic system. The theoretical optimal control voltage and maximum harvested power are derived and verified by simulations. Adaptive control algorithms are proposed for practical applications where the circuit efficiency is not unity and the device parameters may have variation.

Chapter 5 shows the circuits used to implement the active technique. The main power electronic interface circuit is developed with supporting control circuitry. Both dSPACE and microcontroller are used to implement the adaptive control algorithms. The selection of circuit components is discussed, and the power consumption for each part of circuit is analyzed.

Chapter 6 gives the experimental setup and results. The active technique is experimentally tested and compared with the theory. The good agreement shows the validity of the proposed active energy harvesting technique. The power harvesting result of the active technique is also compared with the result of the passive technique, and shows the significant advantage over the passive technique, especially at off-resonance frequencies.

Chapter 7 concludes the dissertation and presents future works.

Chapter 2

Piezoelectric Devices

2.1 Quasi-Static Model of Piezoelectric Devices

Piezoelectricity is a mutual coupling between mechanical strain/stress and electrical field/charge, which can be described by the following linear constitutive equations. [51]

$$\begin{aligned} S_{ij} &= s^E_{ijkl} T_{ij} + d_{ijm} E_m, \\ D_n &= d_{nkl} T_{kl} + \epsilon^T_{mn} E_m, \end{aligned} \tag{2.1}$$

where S_{ij} and T_{kl} are the mechanical strain and stress tensors, and D_n and E_m are the electric displacement and field vectors, respectively. In (2.1) the Einstein summation convention is used. Monolithic piezoelectric materials are rarely used as stand-alone devices, as the generated strain of a piezoelectric material is small, even under high field. Piezoelectric materials, especially ceramics such as PZT, are relatively stiff and require a large stress to be effectively strained. They are therefore often embedded into mechanical structures, constituting devices. These structures include unimorph/bimorph cantilever beams [51], matrix composite structures, and cymbal structures [51]. Piezoelectric materials themselves are also often laminated into multilayer structures or made into fibers to further reduce voltage levels or enhance their robustness [51]. Although the constitutive equations of piezoelectricity are in tensor form, a piezoelectric device can often be described by scalar equations. Under the quasi-static assumption, which neglects mechanical dynamic behavior, linear, frequency-independent equations that represent the device are

written as follows:

$$\begin{aligned} Q &= CV + dF, \\ \delta &= dV + F/k, \end{aligned} \tag{2.2}$$

where δ is the deflection or displacement of the device, Q is the electrical charge on the electrodes of the device, F is the force exerted on the device, V is the voltage across the electrodes, k is the stiffness of the device under constant voltage, d is the general piezoelectric coefficient, and C is the capacitance under constant force. Equation (2.2) reveals that application of electrical voltage V to the piezoelectric device generates mechanical strain δ, and application of mechanical force F to the device generates electrical charge Q.

By differentiating both sides of the first equation in (2.2), and denoting $I = -\dot{Q}$ as the device output current, the constitutive equations (2.2) can be rewritten as

$$\begin{aligned} I = -\dot{Q} &= -C'\dot{V} - kd\dot{\delta}, \\ F &= k\delta - kdV, \end{aligned} \tag{2.3}$$

where $C' = C - kd^2 = C(1 - k_c^2)$ is the capacitance under fixed displacement, and k_c^2 is the electromechanical coupling factor. The equivalent circuit model of the piezoelectric system can then be shown as in Fig. 2.1 by modeling the piezoelectric effect as an transformer with mechanical parameters in the primary side and electrical parameters in the secondary side. $v = \dot{\delta}$ denotes the device velocity.

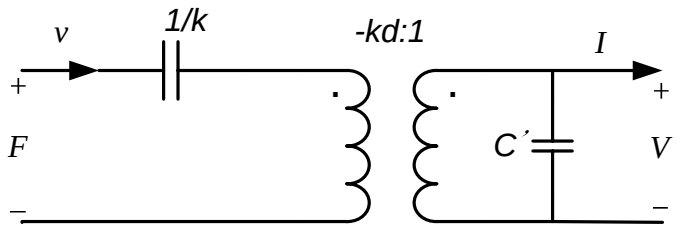

Figure 2.1. Circuit model for quasi-static piezoelectric device

From the circuit model, it can be easily shown that the open-circuit voltage is given by

$$V_{OC} = -\frac{dF}{C}. \tag{2.4}$$

Noting that the open-circuit voltage is directly proportional to the applied

force. The short-circuit current is given by

$$I_{SC} = -j\omega dF. \tag{2.5}$$

The expression of the equivalent electrical impedance can then be obtained by dividing the open-circuit voltage by short-circuit current,

$$Z = \frac{V_{OC}}{I_{SC}} = \frac{1}{j\omega C}. \tag{2.6}$$

2.2 Model of Piezoelectric Devices in Dynamic Systems

A typical dynamic piezoelectric energy harvesting system is a cantilever beam with tip mass, as shown in Fig. 2.2(a). A piezoelectric bimorph is often chosen for the beam, so that the vibration of the end mass will cause deformation to the bimorph, which will then generate an alternative voltage at the output. The system can also be modeled by a simple spring, mass, and damper system, as shown in Fig. 2.2(b), where m is the mass, b is the damping coefficient, the spring coefficient k is the device stiffness, y is the base displacement and x is the free displacement of the mass. The spring represents the ideal compliance, the mass is an energy storage element, and the damper accounts for internal mechanical losses.

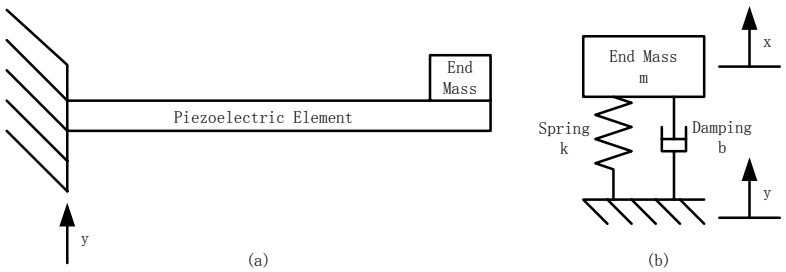

Figure 2.2. (a) Piezoelectric dynamic energy harvesting system, (b) Spring-mass-damper model.

The constitutive equations for the piezoelectric dynamic system are given by

$$\begin{aligned} I &= -\dot{Q} = -C'\dot{V} - kd\dot{\delta}, \\ -m\ddot{y} &= m\ddot{\delta} + b\dot{\delta} + k\delta - kdV, \end{aligned} \tag{2.7}$$

where $\delta = x - y$ is the relative displacement of the mass with respect to the base. The base acceleration can be treated as a force excitation to the dynamic system $F = -m\ddot{y}$. For the secondary equation in (2.7), if we do not consider the last term $-kdV$, the equation becomes the standard dynamic equation for a spring-mass-damper system. But for systems with piezoelectric material as the beam, the application of electrical voltage to the piezoelectric material will affect the displacement of the end mass, which will then in turn change the output current from the first equation in (2.7), resulting in energy harvesting.

The equivalent circuit model for the dynamic electromechanical system can also be established as in Fig. 2.3. The internal mechanical impedance of the system is given by

$$Z_m = b + j(\omega m - \frac{k}{\omega}). \tag{2.8}$$

It can be shown that the magnitude of Z_m will be minimum at the frequency $\omega = \sqrt{\frac{k}{m}}$, which is known as the natural frequency of the system.

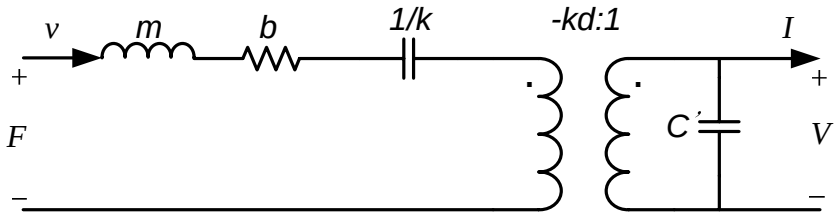

Figure 2.3. Circuit model for piezoelectric dynamic system

The energy harvesting can then be understood as the output power of the circuit, and from the impedance matching point of view, the load impedance should match the internal impedance of the system to maximize the output power. Therefore, to achieve maximum energy harvesting under certain force excitation, the equivalent mechanical load impedance should be $b + j(\frac{k}{\omega} - \omega m)$. Assuming the equivalent force excitation is sinusoidal with a constant magnitude of F_m, the

maximum harvested power is then given by

$$P_{max} = \frac{F_m^2}{8b}. \tag{2.9}$$

We note that this value is the maximum available power of the system, which is independent of the excitation frequency, independent of the electromechanical coupling coefficient, and only depends on the magnitude of the excitation force and damping coefficient.

Assuming the actual electrical load on the right side of Fig. 2.3 is $Z_l = Z_r + jZ_i$, the equivalent mechanical impedance is given by

$$Z_{eq} = k^2 d^2 \frac{Z_l}{1 + j\omega C' Z_l} = k^2 d^2 \frac{Z_r + jZ_i}{1 - \omega C' Z_i + j\omega C' Z_r}. \tag{2.10}$$

At the impedance matching condition, we have the following relationship:

$$\begin{gathered} k^2 d^2 \frac{Z_r + jZ_i}{1 - \omega C' Z_i + j\omega C' Z_r} = b + j(\frac{k}{\omega} - \omega m), \\ \Rightarrow \\ \frac{Z_r + j[Z_i - \omega C'(Z_r^2 + Z_i^2)]}{1 - 2\omega C' Z_i + \omega^2 C'^2 (Z_r^2 + Z_i^2)} = \frac{b + j(\frac{k}{\omega} - \omega m)}{k^2 d^2}. \end{gathered} \tag{2.11}$$

By making the real part and imaginary part of the left side of equation (2.11) equal to those of the right side respectively, the optimal electrical load Z_l can be obtained.

On the other hand, we can obtain the equivalent electrical parameters for Fig. 2.3. The open-circuit voltage of the circuit can be shown to be

$$V_{OC} = \frac{kdF}{\omega^2 C' m - Ck - j\omega C' b}. \tag{2.12}$$

The short-circuit current of the circuit is given by

$$I_{SC} = \frac{j\omega kdF}{\omega^2 m - k - j\omega b}. \tag{2.13}$$

Therefore the equivalent electrical impedance of the dynamic system can be

determined by dividing the open-circuit voltage by the short-circuit current,

$$Z_e = \frac{V_{OC}}{I_{SC}} = \frac{\omega^2 m - k - j\omega b}{\omega^2 C' b + j\omega(\omega^2 C' m - Ck)}. \tag{2.14}$$

To make the electrical impedance match, the electrical load connected to the piezoelectric device should be the complex conjugate of Z_e,

$$Z_{opt} = real(Z_e) - j \cdot imag(Z_e) = \frac{\omega^2 m - k + j\omega b}{\omega^2 C' b - j\omega(\omega^2 C' m - Ck)}. \tag{2.15}$$

It can be shown that equation (2.15) and (2.11) actually give us the same result.

2.3 Parameter Identification of the Piezoelectric Dynamic System

To analyze a piezoelectric dynamic system, we must know all the parameters of the system. The two parameters that can be directly measured are the end mass m and the piezoelectric device capacitance C under constant force. All the other parameters need to be estimated from these two values. Although the piezoelectric constant d can usually be obtained from the device's datasheet, this constant is sensitive to the environment and we can not rely on the datasheet's value.

First we perform a short-circuit test to obtain the short-circuit resonance frequency (natural frequency) of the system. Under short-circuit conditions, the second equation of (2.7) becomes

$$-m\ddot{y} = m\ddot{\delta} + b\dot{\delta} + k\delta, \tag{2.16}$$

and the ratio of relative displacement δ and base displacement y can be obtained by applying the Laplace transform

$$\left|\frac{\Delta(s)}{Y(s)}\right| = \frac{s^2}{s^2 + 2\zeta\omega_n s + \omega_n^2}, \tag{2.17}$$

where $\zeta = \frac{b}{2\sqrt{mk}}$ is the damping ratio, and $\omega_n = \sqrt{\frac{k}{m}}$ is the natural frequency of the system. [52]

For a sinusoidal base excitation, the base displacement can be represented by $y(t) = Ysin(\omega t)$; the corresponding relative displacement is also sinusoidal and can be obtained from (2.17) as

$$\delta(t) = \frac{(\frac{\omega}{\omega_n})^2}{\sqrt{(1-(\frac{\omega}{\omega_n})^2)^2 + (2\zeta\frac{\omega}{\omega_n})^2}} Ysin(\omega t - \phi), \tag{2.18}$$

where $\phi = arctan(\frac{b\omega}{k-\omega^2 m})$ is the phase angle between the relative displacement and base displacement, which will be 90° at the natural frequency. The damping ratio ζ can then be obtained by evaluating (2.18) at the natural frequency ω_n as

$$\zeta = \frac{Y}{2\Delta}, \tag{2.19}$$

where Δ is the magnitude of the relative displacement.

With the knowledge of the mass m, the device stiffness can be obtained as

$$k = m\omega_n^2, \tag{2.20}$$

and the damping coefficient is given by

$$b = 2\zeta\sqrt{mk} = \frac{Ym\omega_n}{\Delta}. \tag{2.21}$$

For the dynamic system there are two resonances since the piezoelectric structure exhibits a different short-circuit and open-circuit stiffness. Hence we also need to perform an open-circuit test to find out the open-circuit resonance frequency. The open-circuit resonance frequency and short-circuit resonance frequency can then be related by

$$\omega_{oc} = \omega_n\sqrt{1+k_e^2}, \tag{2.22}$$

where $k_e^2 = \frac{kd^2}{C-kd^2}$ is the alternative electromechanical coupling coefficient of the system. It should be noted that k_e^2 is different from the conventional electromechanical coupling coefficient k_c^2. For a weakly-coupled system in which k_e^2 is small, the open-circuit resonance frequency will be very close to the short-circuit resonance frequency, while for a strongly-coupled system with large k_e^2, the open-circuit resonance frequency will be further away from the short-circuit resonance frequency.

The alternative coupling coefficient can then be calculated directly from (2.22):

$$k_e^2 = (\frac{\omega_{oc}}{\omega_n})^2 - 1. \tag{2.23}$$

Finally, with the knowledge of the device capacitance C under constant force, the piezoelectric coefficient d can be calculated as

$$d = \sqrt{\frac{Ck_e^2}{k(1+k_e^2)}}. \tag{2.24}$$

Chapter 3

Review of Energy Harvesting Techniques

Typically, energy harvesting systems based on piezoelectric devices can be summarized to have three core components: piezoelectric devices, electric energy storage, and the power electronic interface. With other necessary components, the overall energy harvesting system is shown in Fig. 3.1.

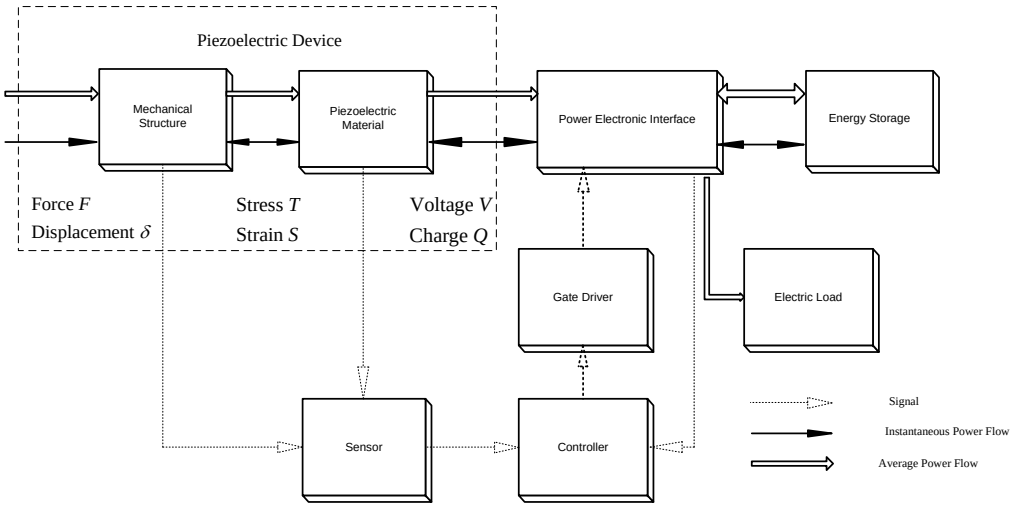

Figure 3.1. Energy harvesting system

In this chapter we will review the existing energy harvesting techniques, focusing on the interface circuit between the energy storage and piezoelectric device.

3.1 Mathematical Expression of Harvested Electric Energy

Converting mechanical energy to electrical energy using piezoelectric devices has been the choice for many energy harvesting applications. The amount of energy that can be harvested is measured by the net amount of energy transferred to the electrical side.

For a general dynamic model as described in equation (2.7), the mechanical energy provided to the system is given by

$$W_{mech} = \int F\dot{\delta}dt = \frac{1}{2}m\dot{\delta}^2 + \int b\dot{\delta}^2 dt + \frac{1}{2}k\delta^2 - kd\int V\dot{\delta}dt. \tag{3.1}$$

According to this equation, the energy provided by the external driving force is distributed into the kinetic energy, the mechanical losses, the elastic energy, and the energy converted into electricity by the piezoelectric element, which is given by

$$W_{conv} = -kd\int V\dot{\delta}dt. \tag{3.2}$$

The average power converted is understood as the energy converted in one period multiplied by the frequency of excitation. Thus the average power converted into electricity by the piezoelectric element depends both on the amplitude and phase difference between the piezoelectric voltage and the first derivative of the displacement (velocity). Under open-circuit conditions, V and $\dot{\delta}$ are 90° out of phase, and so the average power converted into electricity is obviously zero. When a load or the energy harvesting circuit is connected to the piezoelectric device, the phase difference between V and $\dot{\delta}$ tends to change. Thus, the average converted power defined in equation (3.2) is not zero, but the impedance mismatching between the piezoelectric device and load directly reduces the piezoelectric voltage amplitude, which in turn reduces the power that can be harvested. Therefore maximization of the average converted power can be interpreted in this case as determining the optimal piezoelectric voltage magnitude and phase angle to satisfy the impedance matching condition.

3.2 Passive Techniques

The mechanical input power comes from ambient vibrations which may vary in proportion. To compensate for temporary level reductions of the surrounding vibration, or to overcome a power spike generated by the electronic load, an energy storage device must be included in the circuit. Moreover, the piezoelectric element delivering an alternating voltage, an AC-to-DC power converter must interface the energy storage device and the piezoelectric element. These considerations lead naturally to a circuit, herein called the interface circuit, used in most of the piezoelectric energy harvesting systems reported in the literature. [43]

The most simple interface is an AC-DC diode-bridge rectifier followed by a filtering capacitance C_f, as shown in Fig. 3.2. In this circuit, the electrical energy is provided directly to the storage cell through the diode-bridge rectifier. The filtering capacitor is chosen to be large enough so that the rectified voltage V_{bus} is essentially constant to have a stable DC output voltage. The typical waveforms of

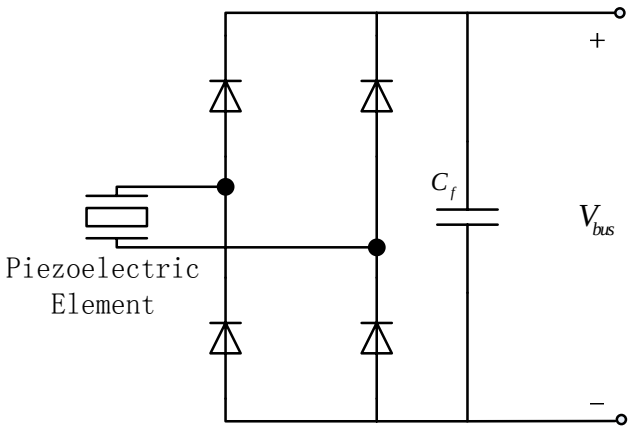

Figure 3.2. AC-DC rectifier based energy harvesting circuit

the displacement and current are shown in Fig. 3.3. The circuit is open circuited if the piezoelectric voltage is less than the bus voltage, and the outgoing piezoelectric element current is null. When the piezoelectric voltage reaches the bus voltage, the bridge conducts and the piezoelectric voltage is blocked at the bus voltage. The conduction in the rectifier diodes is blocked again when the piezoelectric voltage starts decreasing. Hence, the piezoelectric voltage either varies proportionally with the displacement when the rectifying bridge is blocking, or is kept equal to the bus voltage when the bridge conducts. Since the diode-bridge circuit does not require

the knowledge of the state of the piezoelectric device, only allows unidirectional power flow from the piezoelectric device to the storage, and can only emulate resistive load, it is defined as the passive technique.

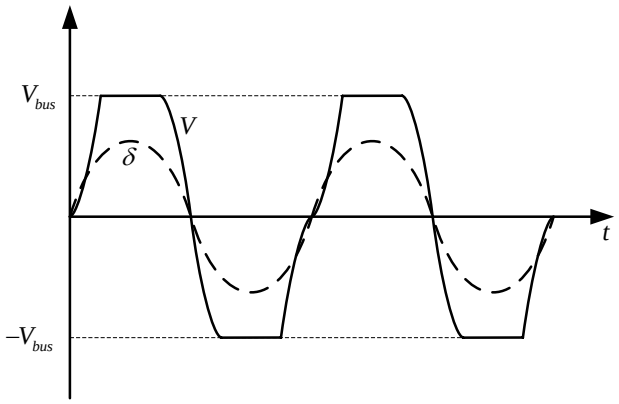

Figure 3.3. Typical waveforms of the displacement δ and voltage V for the rectifier circuit

Piezoelectric devices are often modeled as a current source in parallel with their internal electrode capacitance, as shown in Fig. 3.4, and the source current is the short-circuit current I_{SC}. The piezoelectric device together with the diode

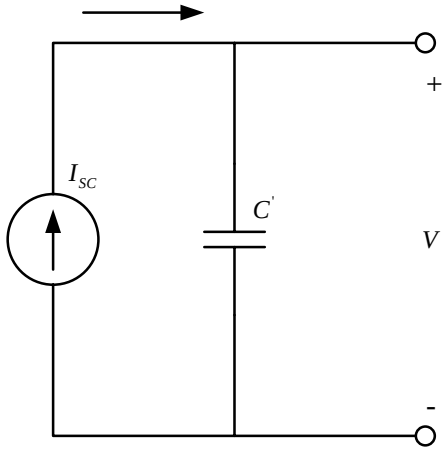

Figure 3.4. Equivalent current source model of the piezoelectric device

rectifier can be treated as a DC voltage source with an internal impedance, given a sufficiently large filter capacitance. Therefore under the concept of electrical impedance matching, the output energy will be maximized if the actual voltage of the storage cell is half of the source's open-circuit voltage, which is also the

peak value of the open-circuit AC voltage of the piezoelectric device under certain excitation.

In actual applications, the storage cell voltage is often fixed, which may not satisfy the impedance matching condition, so an additional interface between the diode-bridge and the storage cell is required to satisfy the impedance match condition and maximize the harvested energy. A typical such interface is a switch-mode step-down DC-DC converter reported by Ottman et. al. [37] [38] The resulting energy harvesting circuit is shown in Fig. 3.5.

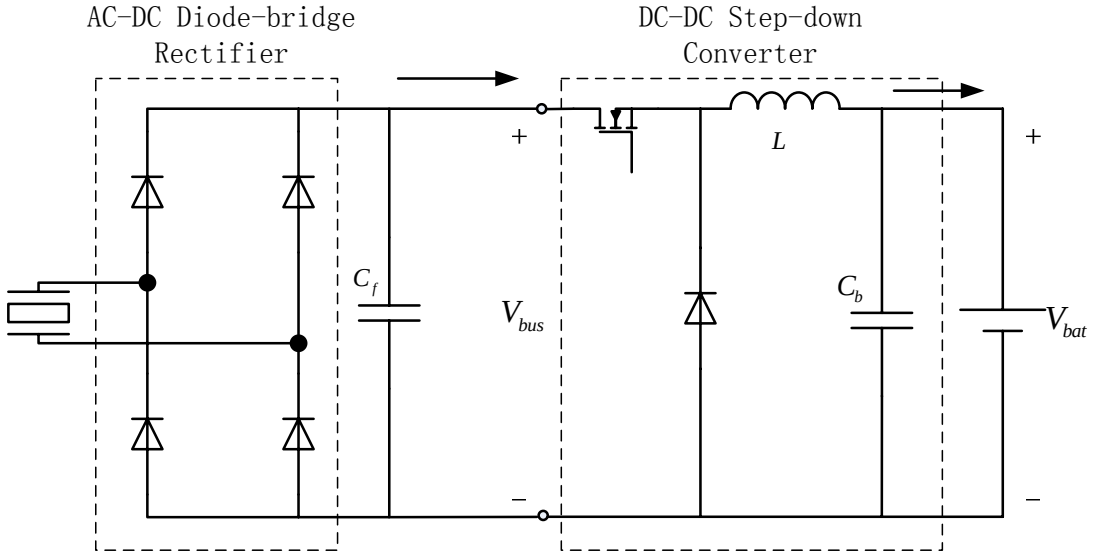

Figure 3.5. AC-DC diode-bridge rectifier circuit with step-down DC-DC converter

In most cases, the power levels associated with energy harvesting are extremely low, hence the power electronic interface is required to be designed in a low-power manner. The discontinuous conduction mode (DCM) of the switched DC-DC converter is reputed for its low power performance[53] [54] [55] [56]. Under this condition, the duty-cycle of the DC-DC converter is given by

$$D = \sqrt{\frac{4V_{bus}\omega LC' f_s}{\pi(V_{bus} - V_{bat})}}, \tag{3.3}$$

where f_S is the switching frequency of the switch and ω is the excitation frequency. To get the maximum power we want the bus voltage to be half of the open-circuit voltage, and so by substituting $V_{bus} = \frac{1}{2}V_{OC} = \frac{I_p}{2\omega C'}$ into equation (3.3), the optimal

duty cycle can be calculated. The maximum power is then given by

$$P = \frac{I_{SC}^2}{2\pi\omega C'}. \tag{3.4}$$

The step-down converter discussed above has superior performance when the input voltage is larger than the output voltage, but it does not function when the input voltage is lower than the output, and if the input voltage is much higher than the output voltage, the efficiency of the step-down converter suffers. Moreover, the optimal duty cycle depends on the load voltage, which needs to be adaptively adjusted in real time. Thus, another DC-DC converter topology without such problems is desired. The transformer-isolated flyback converter is credited for its small component count and simpler control algorithm, and the power switch for the flyback converter is on the lower side of the circuit, which yields great simplification of the gate driver circuit. The passive energy harvesting interface based on the flyback converter is shown in Fig. 3.6.

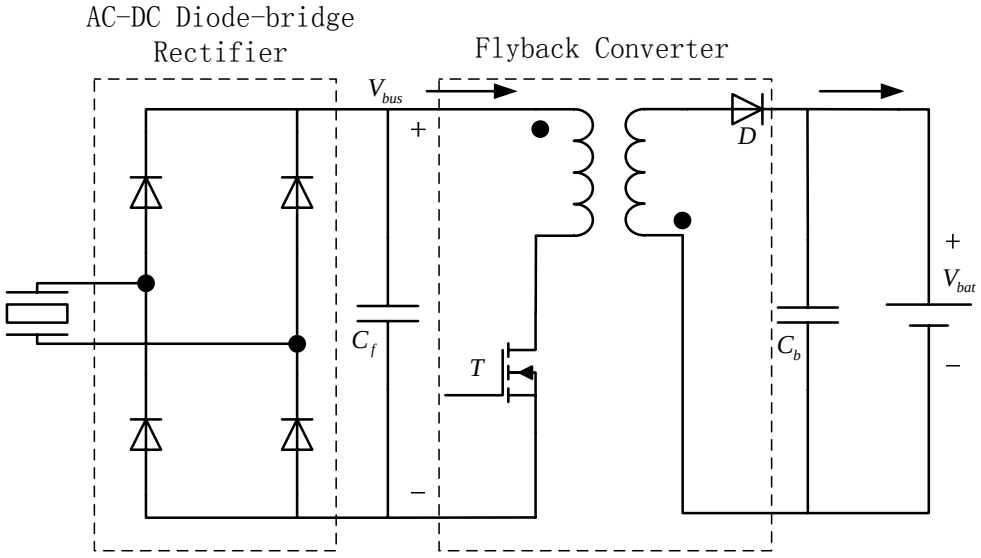

Figure 3.6. AC-DC diode-bridge rectifier circuit with flyback converter

This circuit also works in the DCM condition, and it can be shown that the optimal duty cycle is

$$D_{optmal} = \sqrt{\frac{4L\omega C' f_s}{\pi}}, \tag{3.5}$$

and the maximum harvested power is the same as in (3.4).

Thus, in this case, the optimized constant duty cycle rather than adaptive control will greatly reduce the complexity and power loss of the power electronic interface. Moreover, unlike the step-down converter, the optimal duty cycle of the flyback converter does not depend on the output voltage, so that it is valid for a wide range of excitation. The reason why there exists a constant optimal duty cycle for the flyback converter is that the flyback transformer provides an electrical isolation between the load and source, and so seen from the rectified voltage source, the input resistance of the flyback converter is a value only depending on the duty-cycle.

Behrens et. al. recently proposed a method to adaptively simulate the optimal impedance to harvest the maximum energy [40] [57]. In their case they deal with non-periodic excitations and the optimal energy harvesting requires a nonlinear load impedance. Since their method is resistive impedance matching based, we still consider it as a passive technique.

In above applications, piezoelectric devices are modeled as the current source in parallel with their internal electrode capacitance. This model is based on the assumption that the internal current source of the generator is independent of the impedance of the external load. This is equivalent to assuming that the electromechanical coupling is very weak. Hence if the system is a relatively strongly-coupled system, this current source model will be no longer valid, and the results by the above techniques may differ from the actual values.

In contrast, Shu et. al. developed a more general analytic expression for the power harvesting of a standard AC-DC diode-bridge rectifier circuit with resistive load [58] [59] [60]. If we denote $\Omega = \frac{\omega}{\omega_n}$, where ω is the actual excitation frequency, and $r = C'\omega_n R$, where R is the actual load resistance, the harvested power can be expressed as

$$P = \frac{F_m^2}{\omega_n m} \frac{1}{(r\Omega + \pi/2)^2} \frac{k_e^2 \Omega^2 r}{(2\zeta + \frac{2k_e^2 r}{(r\Omega+\pi/2)^2})^2 \Omega^2 + (1 - \Omega^2 + \frac{\Omega k_e^2 r}{r\Omega+\pi/2})^2}. \tag{3.6}$$

Despite the complexity of this power expression, it reveals that the harvested power by the standard AC-DC rectifier is not only related to the excitation force magnitude F_m, the excitation frequency ω and the load resistance R, but also related to the overall electromechanical coupling coefficient k_e^2 and the mechanical

damping ratio ζ. It can be shown that, for a strongly-coupled system with the excitation frequency near the natural frequency, the standard AC-DC rectifier circuit is good enough to harvest most of the power of a system. However, the harvested power will decrease dramatically at off-resonance frequencies [58] [59] [60]. Moreover, the maximum available power of the system can never be obtained by the rectifier circuit because a diode-bridge rectifier allows only unidirectional power flow and hence can only simulate a resistive load, while the internal impedance of the dynamic system is capacitive in nature. Therefore the mechanical impedance of the system can never be perfectly matched using the rectifier circuit, and a certain amount of energy will be lost due to the mismatching of the impedance. In other words, the passive approach only controls the voltage magnitude across the piezoelectric device without controlling the phase angle of the voltage; thus, the equivalent load impedance can be controlled to some extent, but can not satisfy the impedance matching condition. To make a perfect impedance match we need an inductive load to cancel the capacitive component of the internal impedance, which requires bidirectional power flow circuits to realize this.

3.3 Semi-active Techniques

The basic idea of the semi-active energy harvesting techniques is to shape the voltage across the piezoelectric element in order to reduce the phase shift between the voltage and velocity and at the same time increase the voltage magnitude. Guyomar et. al. reported two types of semi-active energy harvesting techniques as synchronous charge extraction technique and synchronized switch harvesting on inductor (SSHI) technique. The SSHI technique can be further divided into parallel SSHI and series SSHI, but the basic principles of the two techniques are essentially the same. The circuit configurations for the synchronous charge extraction technique, parallel SSHI and series SSHI are shown in Fig. 3.7(a), Fig. 3.8(a) and Fig. 3.9(a), respectively. [43] [44] [46]

The basic principle of the two techniques is very similar. For both techniques, the switch in the circuit is blocking for most of the operation time, and when the displacement of the device reaches a maximum or a minimum, the switch is turned on. The differences between the two circuits occur when the switch is turned on.

For the synchronous charge extraction circuit, when the switch is turned on, the device voltage drops to zero and the energy stored in the piezoelectric capacitance is converted into magnetic energy in the inductor. Then the switched is turned off and the device voltage will change with the displacement from the zero value. The voltage and displacement waveforms are shown in Fig. 3.7(b).

For the SSHI circuits, when the switch is turned on, the inductance and the device capacitance establish an L-C oscillation circuit. The switch is turned off after a half electrical period, resulting in a fast voltage sign inversion on the piezoelectric element. The device voltage will then change with the displacement from the inversion. The voltage and displacement waveforms for parallel and series SSHI are shown in Fig. 3.8(b) and Fig. 3.9(b), respectively.

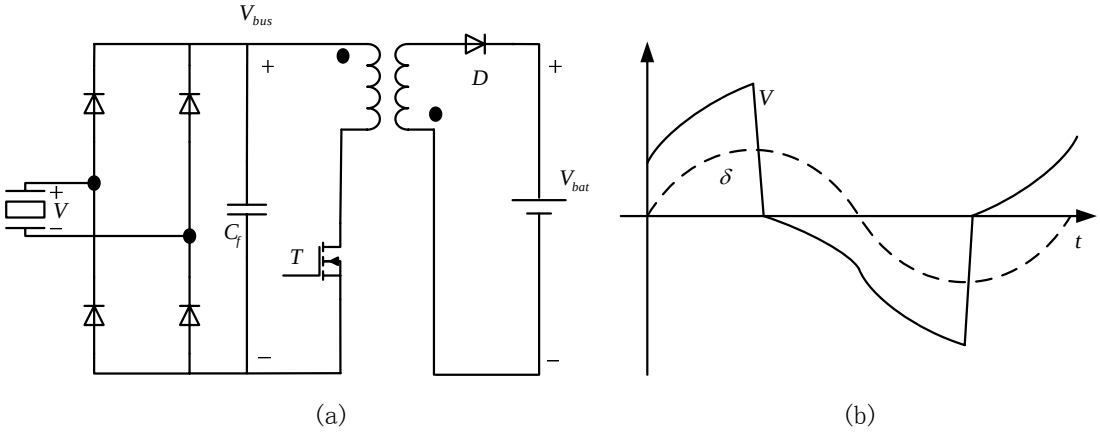

Figure 3.7. (a) synchronous charge extraction circuit, (b) voltage V and displacement δ waveforms

For both techniques, the mentioned switching operation ensures that the voltage and the displacement of the device are 90° out of phase, and so the voltage and the velocity will have the same phase, resulting in maximum energy harvesting according to (3.2) under certain displacement (in their case they assume the piezoelectric constant d to be negative). SSHI is better than the synchronous charge extraction technique in that it reverses the voltage value when the switch is turned on so that the device voltage magnitude is higher than that of the synchronous charge extraction technique. But for the SSHI circuit, the harvested power greatly relates to the quality factor of the inductor, because the oscillation response will be small for a low quality factor L-C circuit, and so the reversed voltage value

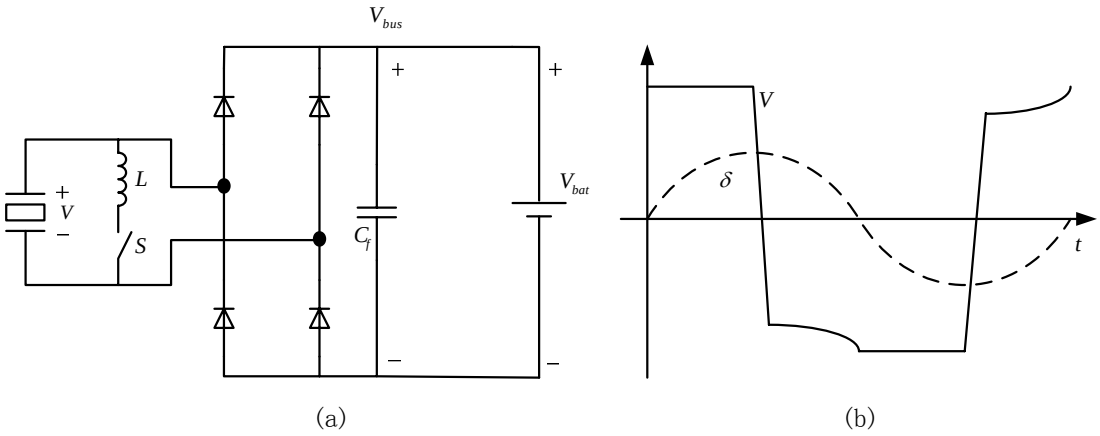

Figure 3.8. (a) parallel SSHI circuit, (b) voltage V and displacement δ waveforms

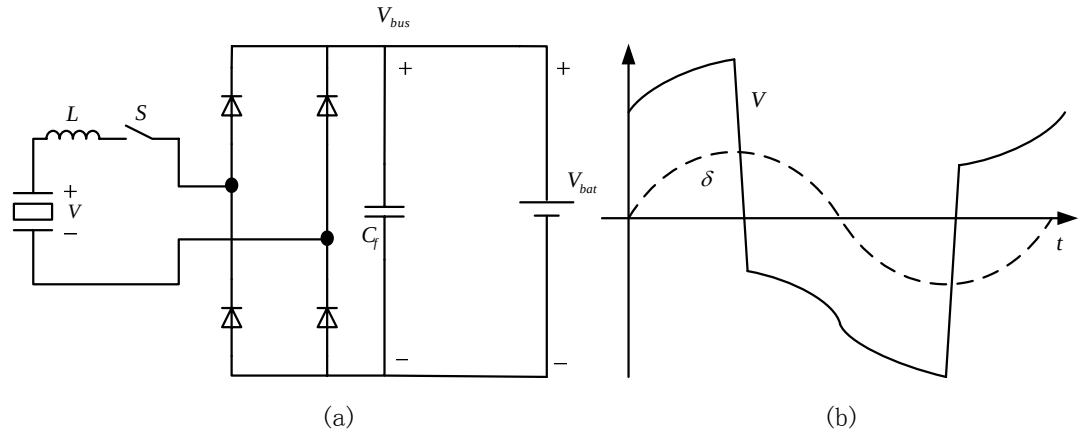

Figure 3.9. (a) series SSHI circuit, (b) voltage V and displacement δ waveforms

will also be low, resulting in smaller power harvesting. Moreover, the maximum power harvesting also requires an optimal rectifier voltage or optimal resistive load for the SSHI circuit, and so an additional DC-DC interface is needed to achieve the optimal rectifier voltage, while there is no such problem for the synchronous charge extraction technique.

To further improve the harvested energy of the SSHI circuit, Mehraeen et. al. proposed an improved SSHI technique by compensating and hence increasing the device voltage level via externally injecting current to the piezoelectric material after each voltage inversion [47]. The compensation circuit is shown in Fig. 3.10. The new switches in the above compensation circuit are synchronized with the original inverting switches by using an adequate delay in order to end the inversion

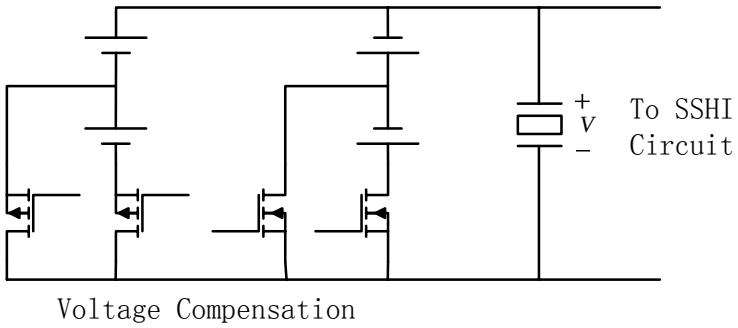

Figure 3.10. Voltage compensation circuit for SSHI

process and establish the new voltage in the original power inversion circuitry. The voltage compensation switches are then closed consecutively to allow the transfer of energy to the piezoelectric clamped capacitor, thus compensating the voltage in each half cycle. This method was shown to be able to increase the harvested power by 50%, however, the compensation circuit is too complicated; it needs additional voltage sources and four switches for just one stage, which will consume a large amount of power. These limitations should be taken into account for practical applications.

Recently, Lallart et. al. proposed a new energy harvesting scheme named Double Synchronized Switch Harvesting (DSSH). This technique is very similar to SSHI, but an additional buck-boost converter is added to the SSHI circuit to improve the performance; the circuit configuration is shown in Fig. 3.11 [48]. The

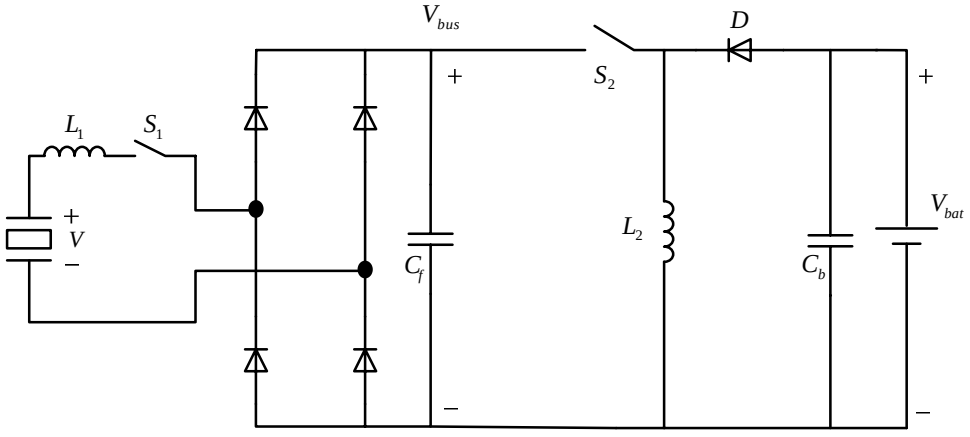

Figure 3.11. Circuit configuration for DSSH

paper compares the performance of the DSSH technique with the synchronous

charge extraction method and the standard rectifier circuit, and shows that the DSSH can ensures an optimal harvested power regardless of the load connected, because of the buck-boost converter. This technique has basically the same principle as SSHI, while the additional intermediate capacitor and Buck-Boost converter can improve the performance at the cost of more circuit components and more losses.

In references [43] and [44] by Guyomar et. al., the maximum harvested power for the basic parallel SSHI is given by

$$P_{max} = \frac{\omega k^2 d^2 \delta_M^2}{\pi C'(1 - e^{\frac{\pi}{2q}})}, \tag{3.7}$$

where ω is the excitation frequency, δ_M is the magnitude of the displacement, and q is the quality factor of the inductor. It was reported that their SSHI technique can boost power harvesting by 8 times compared to the diode-bridge rectifier circuit. However, their result was based on the assumption of a weakly-coupled system with a constant-magnitude end mass displacement, and ideally if the quality factor q is infinity, the harvested power will also be infinity. Obviously this is impractical, because with the development of materials, the electromagnetic coupling is tending to become stronger, and in practice it is the excitation force that is often fixed. Under force excitation, the magnitude of the displacement is not fixed and will change with the applied voltage. In this case, the power harvested by the basic SSHI technique is derived by Shu. et al in [60] as shown in the following:

$$P = \frac{F_m^2}{\omega_n m} \frac{1}{(\frac{1-q}{2} r\Omega + \pi/2)^2} \frac{k_e^2 r}{(2\zeta + \frac{2(1+\frac{r\Omega}{2\pi}(1-q^2))k_e^2 r}{(\frac{1-q}{2} r\Omega + \pi/2)^2})^2}. \tag{3.8}$$

The result in (3.8) is based on the assumption that the external excitation force and the velocity of the mass are in-phase, and it only applies for systems operating at the natural frequency. Shu et. al. also proposed an improved SSHI analysis [60], where the harvested power is given by

$$P = \frac{F_m^2}{\omega_n m} \frac{1}{(\frac{1-q}{2} r\Omega + \pi/2)^2} \frac{k_e^2 \Omega^2 r}{(2\zeta + \frac{2(1+\frac{r\Omega}{2\pi}(1-q^2))k_e^2 r}{(\frac{1-q}{2} r\Omega + \pi/2)^2})^2 \Omega^2 + (1 - \Omega^2 + \frac{\frac{1-q}{2}\Omega k_e^2 r}{\frac{1-q}{2} r\Omega + \pi/2})^2}. \tag{3.9}$$

This result gives the same maximum power as (3.8) at the natural frequency,

yet it can also predict the power harvesting at off-resonance frequencies. If the voltage inversion is perfect (quality factor $q = \infty$), the maximum power can reach the power limit at the natural frequency because in this case the equivalent load impedance can perfectly match the internal impedance of the system.

Compared to the passive techniques, since the phase of the device voltage with respect to the velocity of the mass can be regulated to be the same, the SSHI technique can greatly increase the harvested energy according to (3.2). However, this is based on the assumption that the displacement of the mass will not be affected by the applied voltage and has a constant magnitude, which is not true for most cases. For a constant-magnitude force excitation, since the displacement will be affected by the applied voltage, the same phase of voltage and velocity can not guarantee that the integration in (3.2) is the largest and the power is maximized. It is only true at the natural frequency, as will be seen later on, but at off-resonance frequencies, the equivalent load impedance when the voltage and velocity are in phase does not match the internal impedance, and so the harvested power will decrease accordingly. The impedance mismatching is due to the fact that the diode-bridge converter is still a unidirectional interface circuit and so it is unable to realize an arbitrary impedance that matches the internal impedance for all the frequencies. That is why we call them semi-active techniques, compared to the active techniques we will introduce in the next section, which actively control both the phase and amplitude of the device voltage through a power electronic interface and can realize an arbitrary impedance to the system.

3.4 Active Techniques

Active energy harvesting is a technique that can push energy harvesting to the limits of the piezoelectric device, the power electronic circuitry, or the mechanical structure. Rather than passively accepting the electrical condition generated by the mechanical excitation, the interface circuit could also be responsible for actively applying electrical boundary conditions, such as voltage magnitude and phase, to the piezoelectric device for each energy conversion cycle. Because of the mutual coupling of the piezoelectric devices, an optimized electrical boundary condition could effectively increase the mechanical energy flow into the energy harvester.

We note that there are physical limits of piezoelectric devices, both mechanical and electrical, such as forces, and strains that might crack the device, and breakdown electric fields or depoling voltages. The active energy harvesting technique requires the knowledge of the piezoelectric device state to operate, but it has higher levels of energy harvesting ability, and most important, the power flow is often bidirectional in nature. In the following subsections the basic principle of the active energy harvesting technique is described, and a practical implementation is introduced under quasi-static assumptions.

3.4.1 Boundary Condition Integration Model

The piezoelectric energy conversion process can be graphically presented in the force-displacement and voltage-charge planes illustrated in Fig. 3.12. [1]

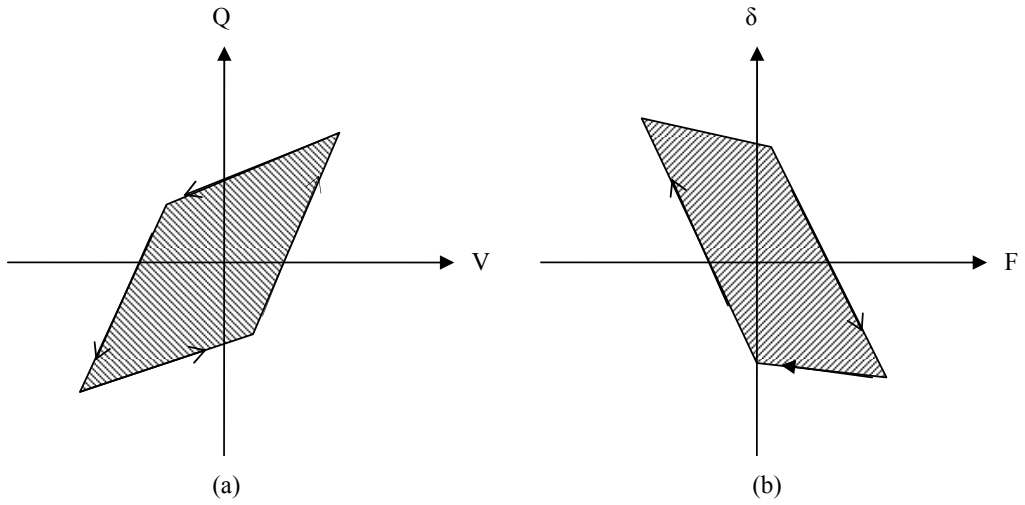

Figure 3.12. Illustration of energy harvesting cycle. (a) electrical domain where shaded area represents the converted electrical energy during one cycle (b) mechanical domain where shaded area represents input mechanical energy for once cycle [1]

An energy conversion cycle is the enclosed mechanical and electrical path the device traverses during one period of mechanical excitation. The enclosed area of the electrical path is calculated as follows:

$$W_e = \oint V dQ = \int_0^T V i dt. \tag{3.10}$$

Equation (3.10) yields time integration of the instantaneous electrical power, which represents the total converted electrical energy over a period. Similarly, it can be shown that the enclosed area in the mechanical domain:

$$W_m = \oint F d\delta, \tag{3.11}$$

which represents the mechanical energy that is converted to electrical energy. If losses in the device are ignored, this mechanical energy is always equal to the output electrical energy. In other words, the two enclosed areas in both domains are equal, though of different shapes. Equation (3.11) also provides intuition into the active energy harvesting approach. In the case of a non-electroactive material, this integration would be zero. However, in the case of a piezoelectric device, the displacement of the device can be adjusted electrically. Hence, for a given mechanical force F, the displacement δ and the integrated area in equation (3.11) can be increased electrically, and hence the amount of mechanical energy to be converted can be increased as well. It is this ability to control the amount of mechanical energy in the device that is converted to electrical energy that makes the active approach so attractive.

The plots in Fig. 3.12 also tell us the instantaneous power flow direction at any state of the device. For example, in the electrical plane a trajectory that is downwards in the I or IV quadrants or upwards in the II or III quadrants, represents negative power, which indicates that power flows from the device to the electrical circuit, and vice versa. This in turn brings up an important point; the power electronic circuitry connected to the piezoelectric device must be capable of bidirectional power flow to implement active energy harvesting approaches.

3.4.2 Quasi-static Active Energy Harvesting Techniques

Under quasi-static assumptions, Tian et. al. implemented a voltage-controlled active energy harvesting for a PVDF material [2] [49]. The typical energy conversion cycle for the voltage-controlled active energy harvesting is shown in Fig. 3.13.

In trajectories $1-2$ and $3-4$, the voltage across the device is kept constant by the power electronic circuitry while the applied force changes from its maximum or minimum value. In trajectories $2-3$ and $4-1$, the power electronic circuitry

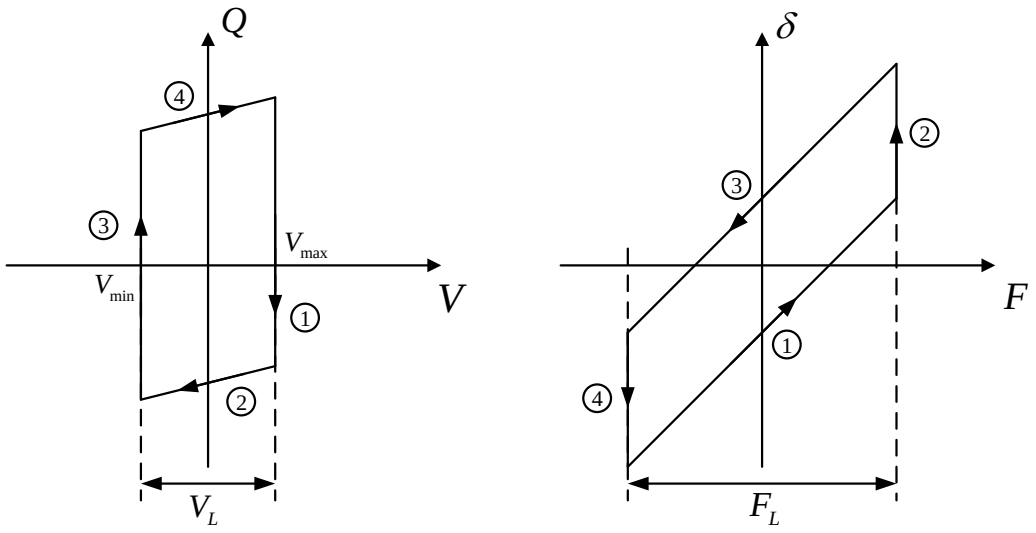

Figure 3.13. Energy conversion cycle for voltage control under quasi-static condition [2]

changes the voltage when the force is at its maximum or minimum values. The typical waveforms are shown in Fig. 3.14. Through this control, the phase angle between the device voltage and the force is always 90°, and since under quasi-static condition, the force and device displacement will have the same phase according to equation (2.2) given piecewise-constant device voltage, the device voltage and displacement will also be 90° out of phase, resulting in maximum harvested energy. Here the displacement is assumed to be fixed-magnitude under the quasi-static condition.

The above control was implemented via a power electronic full-bridge converter which allows bidirectional power flow. From equation (3.2) it seems that, for certain displacement, we should push the magnitude of the applied voltage to the limit of the device to get the maximum energy. It is not the case, however, when we take the efficiency of the power electronic circuit into account. It can be shown that the optimal applied voltage is given by

$$V_{opt} = 2\frac{\eta^2}{1-\eta^2}V_{OC}. \tag{3.12}$$

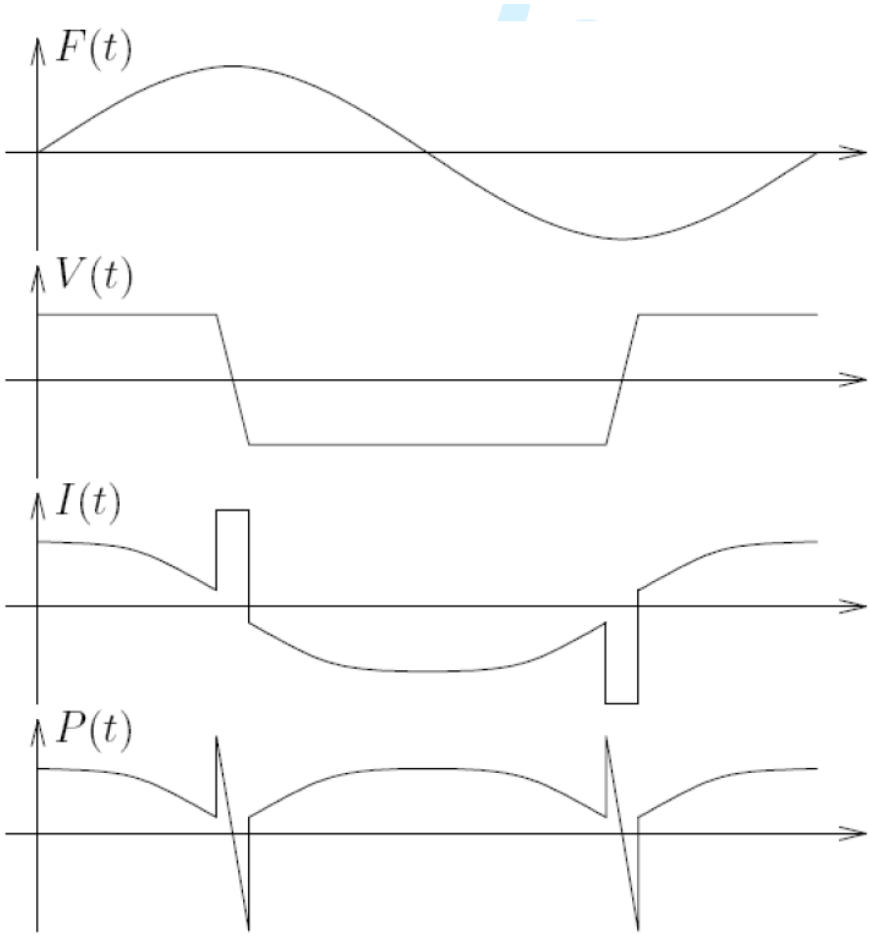

Figure 3.14. Typical waveforms for active technique under quasi-static condition, from top to bottom: force, voltage, current, and power. [2]

and the maximum harvested energy per cycle is given by

$$W_{max} = \frac{\eta^3}{1-\eta^2} C V_{OC}^2, \tag{3.13}$$

where V_{OC} is the peak-peak value of the open-circuit voltage and η is the efficiency of the power electronic circuit. Equation (3.12) and (3.13) indicate that both the optimal voltage and the harvested energy are greatly related to the efficiency of the power electronic circuit. Under the ideal efficiency of 1, the maximum harvested energy tends to infinity and the actual harvested energy is only constrained by the physical limitation of the device. So the design of an efficient power electronic interface circuit is critical for active energy harvesting.

3.5 Discussion

Despite the differences between passive, semi-active and active energy harvesting techniques, the energy harvesting ability of a piezoelectric dynamic system strongly depends upon the characteristics of the system itself, especially the alternative electromechanical coupling coefficient k_e^2 and the mechanical damping ratio ζ. If we consider the impedance matching condition, the optimal load impedance in (2.15) that matches the internal impedance of the piezoelectric system can be rewritten as

$$Z_{opt} = \frac{k^2 d^2 \omega^2 b + j\omega^3 C' b^2 + j\omega(\omega^4 C' m^2 - \omega^2 mk(C + C') + Ck^2)}{\omega^4 C'^2 b^2 + \omega^2 (\omega^2 C' m - Ck)^2}. \tag{3.14}$$

At short-circuit and open-circuit resonance frequencies, the term $j\omega(\omega^4 C' m^2 - \omega^2 mk(C + C') + Ck^2)$ in the numerator of (3.14) will be zero, and so the optimal load impedance can be simplified as (3.15) and (3.16) at short-circuit resonance frequency and open-circuit resonance frequency, respectively:

$$Z_{opt} = \frac{b}{k^2 d^2} \frac{1}{1 + \frac{4}{R_C^2}} (1 + j\frac{2}{R_C}), \tag{3.15}$$

$$Z_{opt} = \frac{b}{(1 + k_e^2) k^2 d^2} \frac{R_C^2}{4} (1 + j\frac{2\sqrt{1 + k_e^2}}{R_C}), \tag{3.16}$$

where $R_C = \frac{k_e^2}{\zeta}$ represents the ratio of the alternative electromechanical coupling coefficient to the mechanical damping ratio.

For a system operating near short-circuit or open-circuit resonance frequencies, (3.15) and (3.16) reveal that for a weakly-coupled system, or the ratio $R_C = \frac{k_e^2}{\zeta} << 1$, the imaginary part of Z_{opt} will be much larger than the real part, and so for the passive diode-bridge rectifier circuit which can only emulate a resistive load, the load impedance will be very far away from the optimal load impedance; therefore, the power harvesting will be much smaller than the maximum available power. Whereas for semi-active (typically, SSHI) and active techniques, this optimal load impedance can be realized (for SSHI this is only true at short-circuit resonance frequency), and so the harvested power can reach the power limit $\frac{F_m^2}{8b}$ and is much larger than that of the passive technique. However, for a strongly-coupled system,

or $R_C = \frac{k_e^2}{\zeta} >> 1$, the imaginary part of Z_{opt} will be negligible, and so the optimal load impedance will be mainly resistive and the passive diode-bridge rectifier can also realize a fairly good impedance matching. So the power harvested by the passive technique can be very close to the maximum available power of the system at both the short-circuit and open-circuit resonance frequencies; although, at the open-circuit frequency the optimal load resistance of the rectifier will be much larger than that at the short-circuit resonance frequency according to (3.16). Hence the passive diode-bridge rectifier circuit is often good enough for a strongly-coupled system operating near resonance frequencies.

At off-resonance frequencies, however, the maximum power harvested by the passive technique will drop significantly as the excitation frequency goes away from resonance frequencies because the imaginary part of the optimal load impedance will increase dramatically. In contrast, the SSHI technique will have a better performance because the technique can emulate a complex impedance; although, the impedance can not perfectly match the internal impedance at frequencies different from the natural frequency. So, the maximum harvested power will also drop with the excitation frequency going away from the natural frequency, but at a slower rate compared to the passive technique. The active technique shows its advantage over the semi-active technique in that it can apply arbitrary boundary conditions to the piezoelectric device and can always emulate the optimal load impedance for all the excitation frequencies, and so the impedance matching condition of the piezoelectric system is always satisfied. Therefore the power harvested by the active technique is always maximized to the maximum available power of the system and is kept that value for all the frequencies, as will be seen in the next chapter.

Chapter 4

Active Energy Harvesting for Piezoelectric Dynamic Systems

In this chapter, we will study the active energy harvesting for a piezoelectric dynamic system described in Fig. 2.2. In the following, we will analyze the active energy harvesting technique for a piezoelectric dynamic system, discuss the adaptive control algorithms that maximize the harvested energy, and compare the active technique to the parallel SSHI technique.

4.1 Active Energy Harvesting Technique for Dynamic Vibration Systems

The constitutive equations for the piezoelectric dynamic system are rewritten here for convenience.

$$\begin{aligned} I &= -\dot{Q} = -C'\dot{V} - kd\dot{\delta}, \\ F &= m\ddot{\delta} + b\dot{\delta} + k\delta - kdV. \end{aligned} \tag{4.1}$$

Taking displacement and velocity as states, we can rewrite the second equation

in (4.1) as follows

$$\begin{gathered}\dot{\delta} = v, \\ \dot{v} = -\frac{k}{m}\delta - \frac{b}{m}v + \frac{1}{m}F + \frac{kd}{m}V, \\ \Rightarrow \\ \begin{bmatrix} \dot{\delta} \\ \dot{v} \end{bmatrix} = \begin{bmatrix} 0 & 1 \\ -\frac{k}{m} & -\frac{b}{m} \end{bmatrix} \begin{bmatrix} \delta \\ v \end{bmatrix} + \begin{bmatrix} 0 \\ \frac{1}{m} \end{bmatrix} F + \begin{bmatrix} 0 \\ \frac{kd}{m} \end{bmatrix} V.\end{gathered} \tag{4.2}$$

The above system can be shown to be controllable, hence we can arbitrarily set the eigenvalues of the system. By making the real part of the eigenvalues negative and large, we cause the mechanical vibrations to quickly decay, corresponding to electrical energy conversion. Taking state feedback as the control voltage input V to the device, $V = k_\delta \delta + k_v v$, the state equation becomes

$$\begin{bmatrix} \dot{\delta} \\ \dot{v} \end{bmatrix} = \begin{bmatrix} 0 & 1 \\ \frac{k_\delta kd - k}{m} & \frac{k_v kd - b}{m} \end{bmatrix} \begin{bmatrix} \delta \\ v \end{bmatrix} + \begin{bmatrix} 0 \\ \frac{1}{m} \end{bmatrix} F. \tag{4.3}$$

Inspection reveals that, while the displacement gain k_δ will affect the natural frequency of the system, the velocity gain k_v will create a damping term that will affect the rate of energy conversion. In chapter 1 we mentioned that the actual ambient excitation may differ from the natural frequency of the system, and so by setting k_δ appropriately, we may be able to shift the natural frequency of the system to the excitation frequency, leading to the largest mechanical energy input. The new natural frequency is given by

$$\omega_s = \sqrt{\frac{k - k_\delta kd}{m}}. \tag{4.4}$$

From (3.2) we also learn that the energy conversion depends upon the product of the voltage and device velocity. Under the feedback control, the converted

energy is given by

$$\begin{aligned} W_{conv} &= -kd \int V\dot{\delta} dt \\ &= -kd \int (k_\delta \delta + k_v v) v dt \\ &= -kd \int (k_\delta \delta v + k_v v^2) dt. \end{aligned} \tag{4.5}$$

Since δ and v have a 90° phase shift, the first integral in (4.34) is zero, and so the converted energy is then

$$W_{conv} = -k_v kd \int v^2 dt. \tag{4.6}$$

To determine the optimal control voltage, we need to determine the optimal displacement gain k_δ and velocity gain k_v. Written in phasor form, the second equation in (2.7) becomes

$$\tilde{F} = (k - \omega^2 m + j\omega b)\tilde{\delta} - kd\tilde{V}, \tag{4.7}$$

where the notation $\sim$ denotes the phasor parameter. By substituting the control voltage, (4.7) becomes

$$\begin{aligned} \tilde{F} &= (k - \omega^2 m + j\omega b)\tilde{\delta} - kd(k_\delta \tilde{\delta} + k_v \tilde{v}) \\ &= (k - \omega^2 m - kdk_\delta)\tilde{\delta} + (b - kdk_v)\tilde{v}. \end{aligned} \tag{4.8}$$

As mentioned before, the mechanical input energy to the system will be maximized if the actual excitation frequency ω matches the natural frequency of the system. So for an optimal control voltage that maximizes the harvested energy, the displacement gain k_δ is always trying to shift the natural frequency of the system to the excitation frequency. From (4.4) such a k_δ is given by

$$k_\delta = \frac{k - \omega^2 m}{kd}, \tag{4.9}$$

and equation (4.8) becomes

$$\tilde{F} = b\tilde{v} - kdk_v \tilde{v}. \tag{4.10}$$

The issue left is to determine the velocity gain k_v that maximizes the output energy given in equation (4.6). From (4.10), assuming a constant-magnitude force excitation, it is obvious that (4.6) will be maximized when $b\tilde{v} = -kdk_v\tilde{v}$, and so the optimal velocity gain is given by

$$k_v = -\frac{b}{kd}. \tag{4.11}$$

Hence, the optimal control voltage that maximizes the harvested energy is given by

$$\begin{aligned} \tilde{V}_{opt} &= \frac{k - \omega^2 m}{kd}\tilde{\delta} - \frac{b}{kd}\tilde{v} \\ &= (\frac{k - \omega^2 m}{kd} - j\omega\frac{b}{kd})\tilde{\delta}, \end{aligned} \tag{4.12}$$

Combining (4.12) and (4.7), we can then express the optimal control voltage in terms of the excitation force:

$$\tilde{V}_{opt} = \frac{-\omega b - j(k - \omega^2 m)}{2kd\omega b}\tilde{F}. \tag{4.13}$$

Assuming the excitation force has a fixed constant magnitude F_m, the optimal magnitude of the control voltage can be determined as

$$V_{mag} = \sqrt{\omega^2 b^2 + (k - \omega^2 m)^2}\frac{F_m}{2kd\omega b}. \tag{4.14}$$

The optimal phase angle of the control voltage can be determined by using the excitation force as the reference signal, and the optimal phase difference between the control voltage and the excitation force is given by

$$\phi = 180 - arctan(\frac{k - \omega^2 m}{\omega b}). \tag{4.15}$$

Under certain excitation force, there always exists an optimal control voltage that maximizes the energy harvesting.

Under the optimal control voltage, the corresponding maximum harvested en-

ergy is given by

$$W_{max} = -k_v kd \int v^2 dt = \frac{1}{4b} \int F^2 dt, \tag{4.16}$$

and the time averaging of W_{max} gives us the maximum harvested power:

$$P_{max} = \frac{1}{T}\frac{1}{4b} \int F^2 dt = \frac{F_m^2}{8b}, \tag{4.17}$$

where T is the excitation period. Since we assume the magnitude of the excitation force to be constant, the above equation indicates that the maximum harvested power will be constant under any excitation frequency by applying the proposed control voltage, because the system always operates at resonance.

Particularly, if the excitation frequency is the natural frequency of the system, we have $k - \omega^2 m = 0$, and so we do not need a displacement gain and the optimal control voltage will be proportional to the velocity. In this case, we have

$$\tilde{V}_{opt} = -\frac{b}{kd}\tilde{v} = \frac{-\tilde{F}}{2kd}, \tag{4.18}$$

so the optimal control voltage will have the opposite phase with the device velocity and excitation force, and the voltage transition instants correspond to the maximum or minimum displacement, as introduced in [43] [46]. etc. However, for off-resonance frequencies, the voltage transition instants may not occur at the peak values of the displacement, and so the control scheme proposed by Guyomar et. al. for the SSHI technique is no longer valid for dynamic systems operating at off-resonance frequencies.

The maximum power harvested by the active technique is also the absolute maximum power that can be harvested from the dynamic system, as mentioned in (2.9), and so the active energy harvesting technique can always harvest the maximum available power of a dynamic system. We can also consider this from the impedance matching point of view. For the active energy harvesting technique, we apply a sinusoidal control voltage across the vibrating piezoelectric device with certain voltage amplitude and phase angle. Under a constant-magnitude sinusoidal excitation force, the frequency of the control voltage is the same as the excitation frequency, and the corresponding piezoelectric current flowing out of the piezoelectric device will also be sinusoidal with the same frequency. Considering the applied

control voltage in together with the generated output current, this is equivalent to applying a certain electrical impedance to the piezoelectric system, and the optimal control voltage will be equivalent to the optimal electrical impedance. Thus by using the active energy harvesting technique in which we can apply control voltage with arbitrary magnitude and phase angle, we can always find the control voltage that results in the optimal electrical impedance, and so maximum power can always be harvested. The maximum harvested power is independent of the excitation frequency, independent of the material's coupling coefficient, and only depends on the excitation force F_m and the mechanical damping coefficient b.

To verify this, the following analysis is made. Under the optimal control voltage, the device displacement can be derived from (4.13) as,

$$\tilde{\delta} = \frac{kd}{k - \omega^2 m - j\omega b}\tilde{V}_{opt}. \tag{4.19}$$

Substituting (4.19) into the first equation of (4.1), the output current and the equivalent electrical impedance under optimal control voltage can be obtained:

$$\begin{aligned} \tilde{I} &= \frac{\omega^2 C'b - j\omega(\omega^2 C'm - Ck)}{\omega^2 m - k + j\omega b}\tilde{V}_{opt}, \\ &\Rightarrow \\ Z = \frac{\tilde{V}_{opt}}{\tilde{I}} &= \frac{\omega^2 m - k + j\omega b}{\omega^2 C'b - j\omega(\omega^2 C'm - Ck)}. \end{aligned} \tag{4.20}$$

Equation (4.20) is exactly the same as (2.15), which means that the equivalent electrical load impedance under the optimal control voltage is indeed the optimal load impedance that matches the internal electrical impedance of the system, and so the maximum power can always be obtained by the active energy harvesting technique by applying the proposed optimal control voltage.

To verify the above theory, we perform a phasor simulation in MATLAB. In the simulation we simulate the piezoelectric dynamic system as shown in Fig. 2.2. The parameters of the system can be found in Table. 4.1, which were experimentally determined, as will be discussed in Chapter 6. The excitation is a variable-frequency sinusoidal force with magnitude of $F_m = 0.364N$ and phase angle of 0, and the natural frequency can be calculated to be $121Hz$. The MATLAB code can be

found in Appendix A.1.

Table 4.1. System Parameters

$m(g)$	$k(N/m)$	$b(Ns/m)$	$d(\mu m/V)$	$C(\mu F)$	$C'(\mu F)$	ζ	k_e^2
7	4046	0.4635	1.86	0.18	0.166	0.0435	0.0844

In the simulation, for excitation frequencies from $105Hz$ and $145Hz$, we vary the magnitude and the phase angle of the applied control voltage to find the maximum power that can be harvested. The corresponding voltage that results in the maximum harvested power is then recorded. The maximum harvested power is shown in Fig. 4.1, and the magnitude and phase angle of the corresponding optimal control voltage are shown in Figs. 4.2 (a) and 4.2 (b), respectively. All the simulation results are compared to the theoretical values calculated by (4.16), (4.13), and(4.15). To show the benefit of the active energy harvesting technique, the power harvested by the active technique is also compared with the theoretical maximum power harvested by the passive AC-DC diode-bridge rectifier circuit and the semi-active parallel SSHI circuit calculated by (3.6) and (3.9), respectively. For (3.6) and (3.9), we vary the load resistance values until the maximum power is reached. For the power calculation of the parallel SSHI circuit, we assume the quality factor of the inductor to be infinite, which means that the inversion of the voltage is ideal. The results are also shown in Fig. 4.1.

From Fig. 4.1, for a wide range of excitation frequency, the maximum harvested power is almost constant and equals the theoretical absolute maximum power that can be harvested, as predicted previously. Compared to the passive technique, since the simulated piezoelectric dynamic system is a relatively strongly-coupled system, the harvested power by the active technique is not significantly larger than that of the passive technique near resonance frequencies. However, at off-resonance frequencies, the power harvested by the active technique is much larger because it is essentially a constant and will not be affected by the excitation frequencies, while the power harvested by the passive technique becomes much smaller when the excitation frequency is far away from the resonance. Also for the parallel SSHI technique, although the maximum harvested power is the same as the active technique at resonance frequency assuming ideal voltage inversion ($q = 1$), it drops dramatically as the excitation frequency goes away from the resonance frequency.

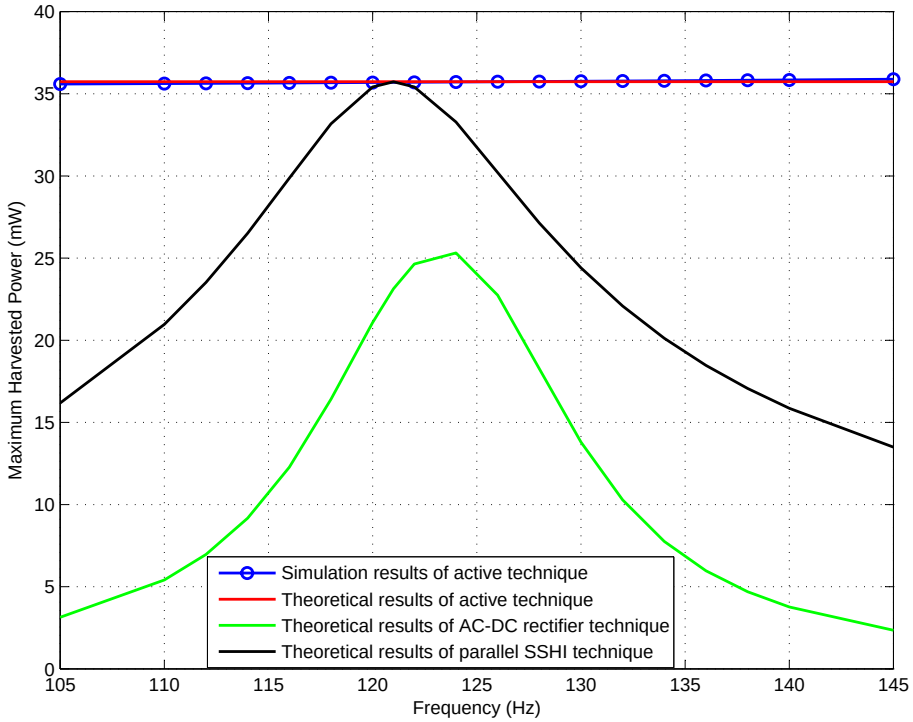

Figure 4.1. Comparison of maximum power harvesting of active, AC-DC rectifier, and parallel SSHI technique

The advantages of the active technique over the passive and semi-active techniques are clearly shown. Also for the active technique, the actual optimal voltage matches the theoretical value very well both in magnitude and phase angle, hence the proposed control voltage indeed maximizes the output power.

In the above analysis and simulation, we did not take the circuit efficiency into account for simplicity. The analysis will be much more complicated when we consider the circuit efficiency. If a constant circuit efficiency η is assumed, then during the whole energy harvesting process, when there is energy flowing out of the device, the actual harvested energy should be multiplied by the efficiency η, and when there is energy flowing into the device, the actual consumed energy from the output should be divided by the efficiency η. Therefore the net energy flow

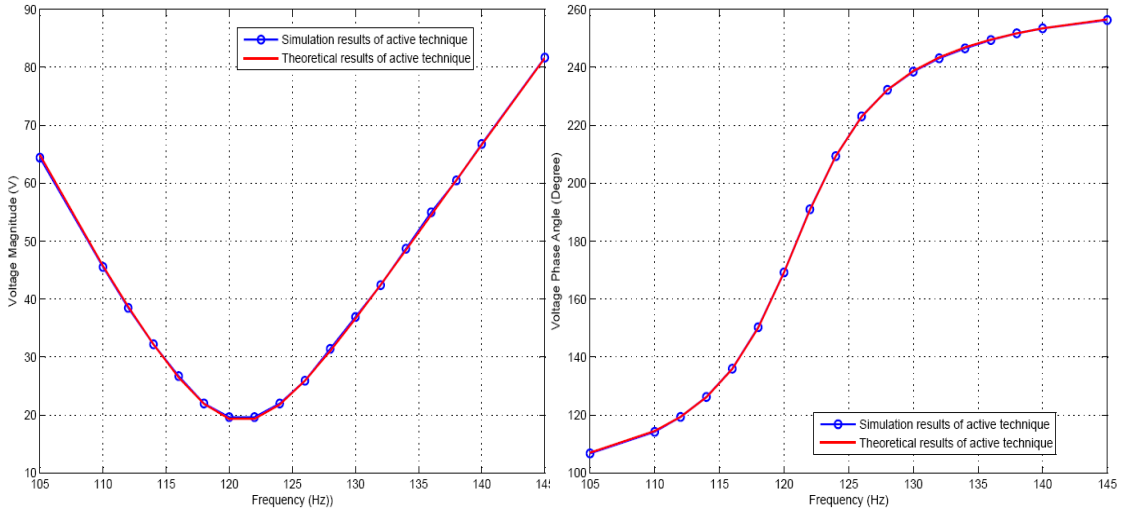

Figure 4.2. Optimal control voltage of the active technique: (a) voltage magnitude, (b) voltage phase angle

per energy conversion cycle is given by

$$W_{net} = \eta W_{out} - \frac{1}{\eta} W_{in}, \tag{4.21}$$

where W_{out} is the output energy per cycle and W_{in} is the input energy per cycle.

To study the effect of the circuit efficiency on energy harvesting, we re-perform the phasor simulation for the dynamic system with the same parameters and excitation as before considering different circuit efficiencies. Again, we vary the excitation frequency and find the optimal voltage that maximize the harvested power at each excitation frequency. The simulation results of the maximum harvested power, optimal voltage magnitude, and optimal voltage phase angle, are shown in Figs. 4.3, 4.4 (a), and 4.4 (b), respectively.

Fig. 4.3 indicates that the maximum harvested power decreases with decreasing efficiencies, and the harvested power is no longer a constant for different excitation frequencies if the efficiency is not unity. Generally the harvested power will be larger at near-resonance frequencies, because the optimal voltage magnitude will be larger at frequencies further away from the natural frequency, and the larger the voltage magnitude is, the larger the power loss will be. The optimal voltage magnitude is therefore lower at lower circuit efficiencies. Also, the voltage phase

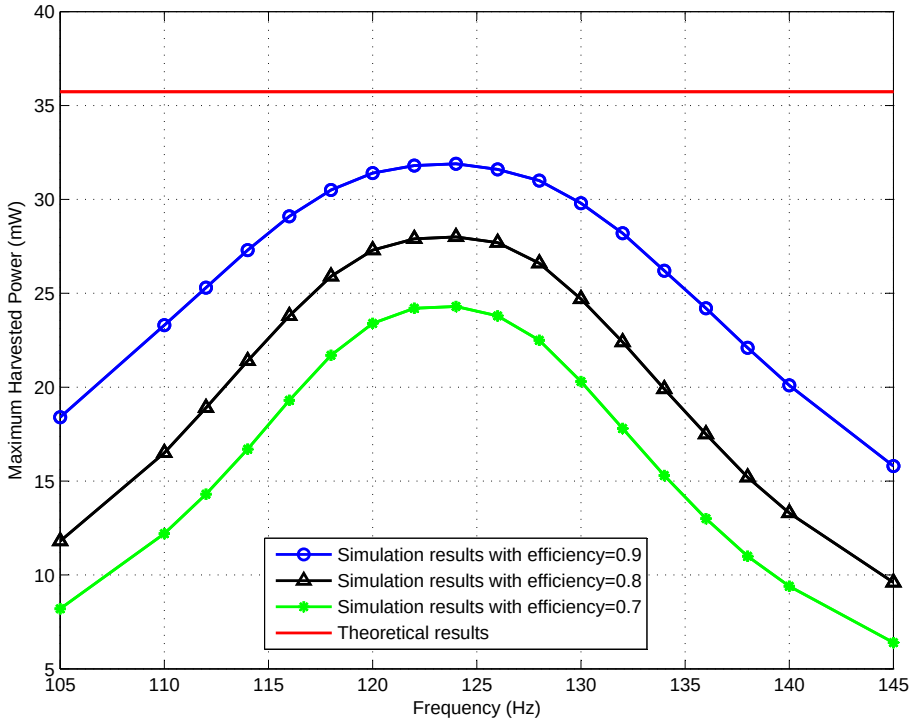

Figure 4.3. Maximum harvested power of the active technique for different circuit efficiencies

angle is different from what we obtained for unity efficiency before.

In practical implementation, because of the effect of the efficiency on energy harvesting, we need to perform numerical simulation to determine the optimal control voltage and transition instant, but the complexity of the actual efficiency of the circuit may make the results incorrect. Furthermore, the deviations and changes of the actual device parameters (stiffness, piezoelectric constant, .etc) from estimated values will also lead to suboptimal performance. This is specially true when the system is excited near the natural frequency of the system. For example, assuming the system is excited at $120Hz$ (natural frequency of $121Hz$) with previous simulation parameters, and considering the circuit efficiency of 100%, the optimal control voltage magnitude and phase angle are calculated by (4.14) and (4.15) as $V_m = 19.64V$, $\phi = 169.2°$, respectively. Then assuming the actual stiffness k is 10% greater than the estimated value, using the previous optimal control voltage, the harvested power is calculated as $P = 19.2mW$, while the actual

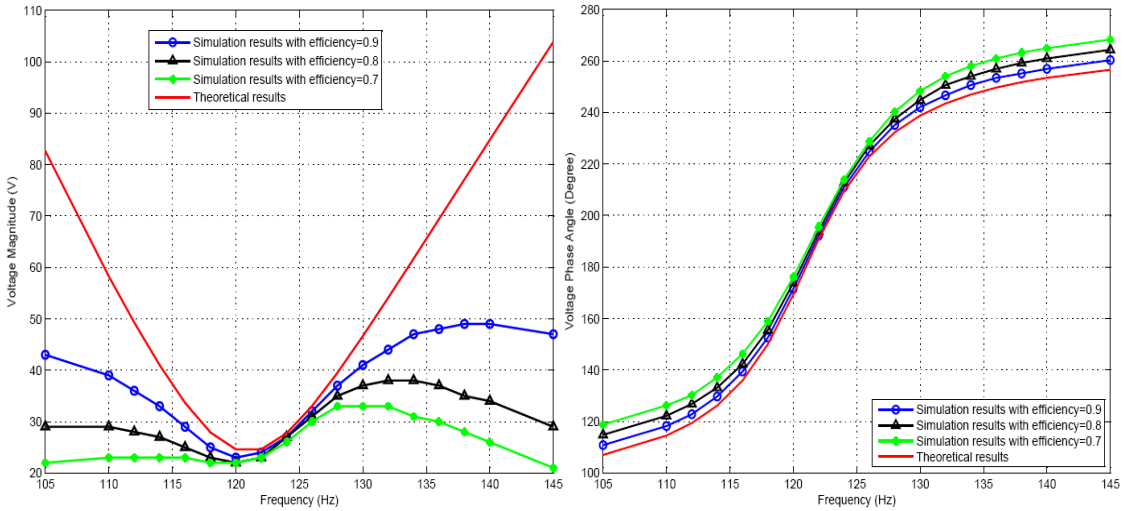

(a) (b)

Figure 4.4. Optimal control voltage of the active technique for different circuit efficiencies: (a) voltage magnitude, (b) voltage phase angle

optimal control voltage is $V_m = 29.06V$, $\phi = 126.8°$, and the actual maximum power is $P_{max} = 35.7mW$. Therefore, a small derivation of device parameter has a very significant effect on the optimal control voltage and harvested power; hence, we need to develop certain control algorithms to adaptively determine the optimal control voltage, as discussed in the next section.

4.2 Adaptive Control Algorithm for Active Energy Harvesting

The goal is to build a control algorithm to find the optimal control voltage magnitude and transition instant (or phase angle) that results in maximum energy harvesting with the information that can be easily obtained from the circuit. Such information includes the excitation force and average harvested power. Assuming we use a constant-voltage battery as the load, the average harvested power is then determined by measuring the current flowing into the battery.

As mentioned previously, under certain excitation force, the harvested power is a function of the magnitude and phase angle of the applied control voltage. Under an excitation force of natural frequency with $0.364N$ magnitude and 0 phase angle,

using parameters in Table. 4.1, and assuming a unity circuit efficiency, the contour plot of the harvested power as a function of voltage magnitude and phase angle is shown in Fig. 4.5. The contour curves are looser in density near the peak power, which indicates that the harvested power will be close to the peak value for a fairly wide range of voltage magnitude and phase angle.

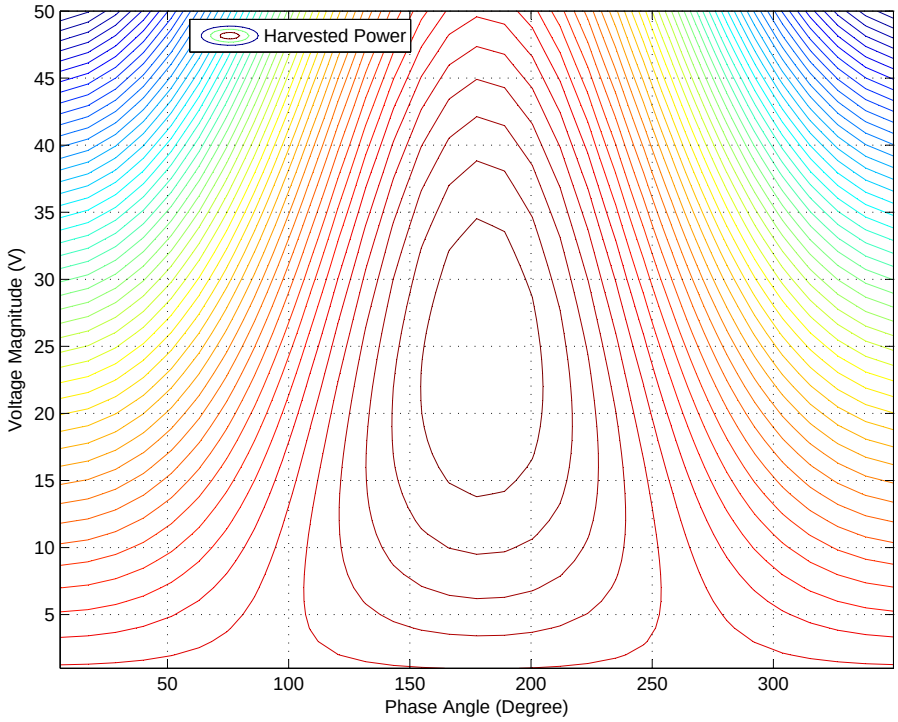

Figure 4.5. Harvested power as a function of voltage magnitude and phase angle, peak power value of $35.7mW$, with $6.57mW$ decay per contour curve

From Fig. 4.5, it is apparent that the most efficient way to find the optimal control voltage is to vary the magnitude and phase angle simultaneously with the gradient direction of the power function for a given initial value. The difficulty here is that we do not know an explicit expression of the harvested power function when we take the circuit efficiency into account, and also the device parameters are hard to estimate. We propose a two-dimensional quadratic interpolation method similar to the one dimensional sequential quadratic interpolation [61] [62].

In the algorithm, we first pick up an initial value for voltage magnitude and phase angle (V_{m1} and ϕ_1), which can be determined by (4.14) and (4.15), respec-

tively. Then we choose 4 other points around the initial point (V_{m2} and ϕ_2, V_{m3} and ϕ_3, V_{m4} and ϕ_4, V_{m5} and ϕ_5 and construct a quadratic surface to fit the local surface around the initial point. If we choose the 4 points close enough to the center initial point, we consider this interpolation accurate enough. To get a unique solution, the simplified interpolating quadratic is given by

$$\begin{aligned} P &= \frac{1}{2}\vec{x}^T A\vec{x} + \vec{b}^T\vec{x} \\ &= \frac{1}{2}\begin{bmatrix} V_m & \phi \end{bmatrix}\begin{bmatrix} a_1 & a_2 \\ a_2 & a_3 \end{bmatrix}\begin{bmatrix} V_m \\ \phi \end{bmatrix} + \begin{bmatrix} b_1 & b_2 \end{bmatrix}\begin{bmatrix} V_m \\ \phi \end{bmatrix}, \end{aligned} \tag{4.22}$$

and the gradient of P is then given by

$$\frac{dP}{d\vec{x}} = A\vec{x} + \vec{b}. \tag{4.23}$$

We then measure the harvested power for the 5 points(P_1 to P_5). The parameters of the above quadratic expression can be determined as follows:

$$\begin{bmatrix} a_1 \\ a_2 \\ a_3 \\ b_1 \\ b_2 \end{bmatrix} = \begin{bmatrix} \frac{1}{2}V_{m1}^2 & V_{m1}\phi_1 & \frac{1}{2}\phi_1^2 & V_{m1} & \phi_1 \\ \frac{1}{2}V_{m2}^2 & V_{m2}\phi_2 & \frac{1}{2}\phi_2^2 & V_{m2} & \phi_2 \\ \frac{1}{2}V_{m3}^2 & V_{m3}\phi_3 & \frac{1}{2}\phi_3^2 & V_{m3} & \phi_3 \\ \frac{1}{2}V_{m4}^2 & V_{m4}\phi_4 & \frac{1}{2}\phi_4^2 & V_{m4} & \phi_4 \\ \frac{1}{2}V_{m5}^2 & V_{m5}\phi_5 & \frac{1}{2}\phi_5^2 & V_{m5} & \phi_5 \end{bmatrix}^{-1} \begin{bmatrix} -P_1 \\ -P_2 \\ -P_3 \\ -P_4 \\ -P_5 \end{bmatrix}. \tag{4.24}$$

Since the power function is a concave set, the negative power will be a convex set, and so we use the negative harvested power in (4.24). We can then calculate the gradient direction by (4.23) for the initial point, and move along that direction by a certain amount to reach a new operating point. Then we repeat this process until convergence is attained. Under an excitation force of natural frequency, the simulation result is compared with the contour plot of the power function in Fig. 4.6. To illustrate the convergence of the method, we choose two initial conditions far away from the optimal point. The lines in the figure represent the searching paths to the optimal control voltage, and for both initial conditions the optimal operating point is reached. Actually, global convergence is assured as the cost function (negative harvested power) is a convex set. The MATLAB code for the

simulation can be found in Appendix A.2.

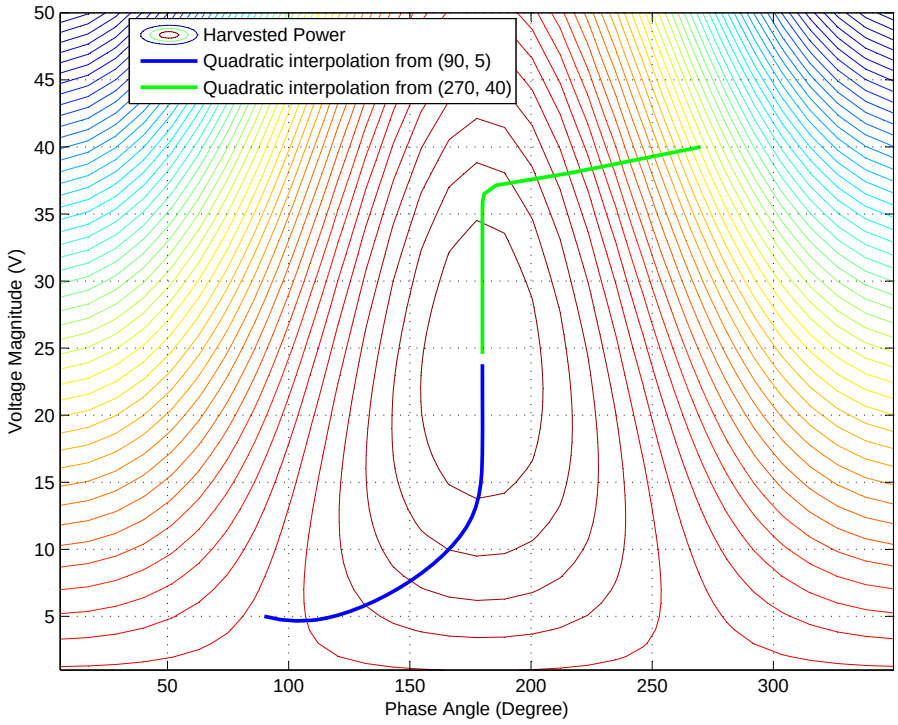

Figure 4.6. Searching paths of the quadratic interpolation method, peak power value of $35.7mW$, with $6.57mW$ decay per contour curve

For the quadratic interpolation method, we only need to know the average harvested power for every operating point, and we can control both the voltage magnitude and phase angle simultaneously. The drawback of this method is that it is computationally intensive because we need to do the interpolation and find the gradient. A simpler algorithm is also developed for comparison. This algorithm is the so called "two-step" algorithm, in which we first pick up an initial value for the voltage magnitude and phase angle (V_{m1} and ϕ_1), and record the harvested power P_1; then we increase one condition with certain increments and keep the other condition unchanged. For example, we increase the voltage magnitude V_{m1} to $V_{m1} + V_{step}$, and compare the harvested power P_2 to P_1. If $P_2 > P_1$, we keep the new voltage magnitude; otherwise, we make the new magnitude to be $V_{m1} - V_{step}$, and the power under the new magnitude and original phase angle is recorded as $P3$. Then we increase the other condition, in this example, voltage phase angle

to $\phi_1 + \phi_{step}$, and keep the voltage magnitude unchanged. The power is recorded as P_4 and compared with P_3. Again, if $P_4 > P_3$, we keep the new voltage phase angle, otherwise, we make the new phase angle to be $\phi_1 + \phi_{step}$. By repeating this process, the optimal operating point can also be reached. The simulation result of the "two-step" algorithm is compared with the quadratic interpolation in Fig. 4.7. The searching path of the "two-step" method is not as smooth as the quadratic interpolation method because it can not control the voltage magnitude and phase angle simultaneously. Also for the "two-step" method, the initial point can not be too far away from the optimal operating point, while there is no such problem for the quadratic interpolation method. The MATLAB code for the simulation can be found in Appendix A.3.

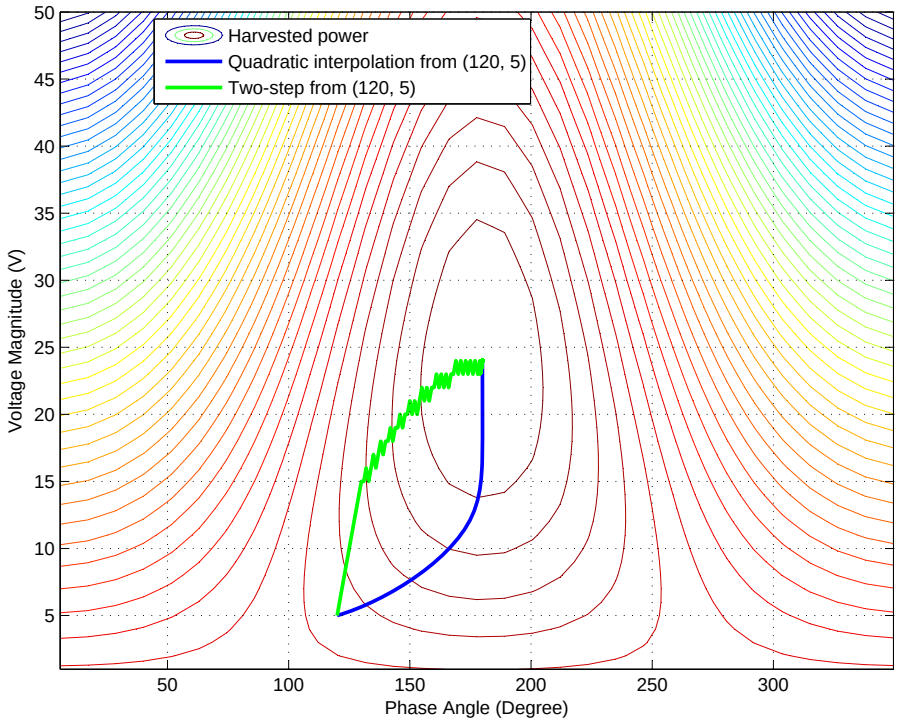

Figure 4.7. Comparison of searching paths of the two-step method and quadratic interpolation method, peak power value of $35.7mW$, with $6.57mW$ decay per contour curve

4.3 Piecewise-constant Control Voltage

In the above analysis, we assume the control voltage is sinusoidal under a sinusoidal excitation force, but the generation of the sinusoidal voltage is complicated and inefficient in actual implementation, because a sinusoidal duty cycle is needed for a typical full-bridge converter, which would require constant switching. At the low power levels associated with energy harvesting, the resulting switching losses are significant and reduce the effectiveness of the active technique dramatically. Hence we propose a bipolar square-wave piecewise-constant control voltage whose fundamental component is the same as the optimal sinusoidal control voltage. Since the magnitude of the fundamental component is larger than that of a square-wave, the actual voltage magnitude can be reduced to $\frac{\pi}{4}$ of the original voltage magnitude. The voltage transition instant of the piecewise-constant control voltage corresponds to the phase angle of its fundamental component. So if we have the information of the excitation force, we can calculate the appropriate phase angle at which we do the voltage transition according to (4.15). In practical implementation where the circuit efficiency is not unity, the harmonic components of the piecewise-constant voltage will have an effect on the energy harvesting, and so both the voltage magnitude and transition instant of the control voltage should be determined adaptively. This piecewise-constant control voltage can be easily generated by a full-bridge converter, and during the period where the voltage is constant, we do not need to perform switching at all, and so the circuit is much more efficient.

To see the results under the piecewise-constant control voltage, a simulation is also performed in MATLAB Simulink, with block diagrams shown in Fig. 4.8. The parameters and excitation are all the same as the previous phasor simulation. Since the instant transition of the voltage will cause large current spikes when charging and discharging the capacitor, a rate limiter is added.

The typical waveforms of the applied voltage, device output current, instantaneous power, and excitation force are shown in Fig. 4.9 when the maximum power is harvested with an optimal control voltage under the excitation frequency of the natural frequency ($121Hz$) and circuit efficiency of unity.

Under a piecewise-constant control voltage, there exists a charging/discharging

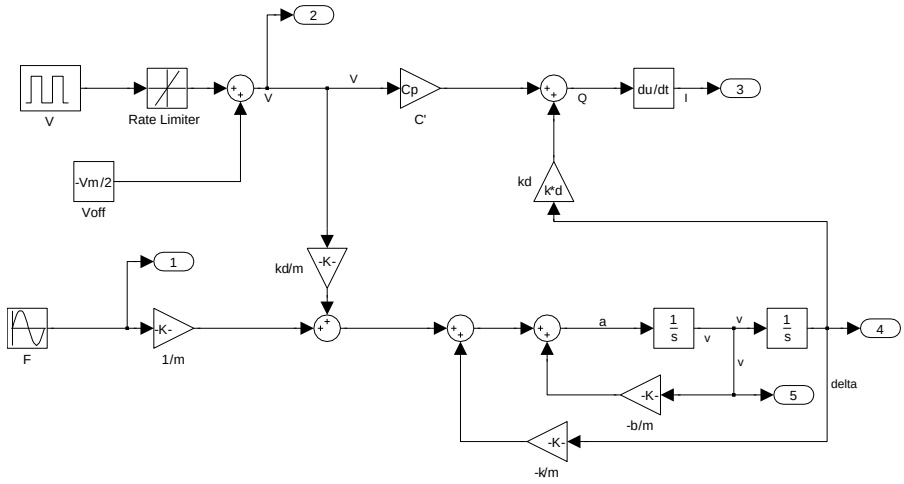

Figure 4.8. MATLAB Simulink model for the piezoelectric dynamic system with piecewise-constant control voltage

current during the voltage transition period, which is undesired. A large value of the charging/discharging current may cause non-negligible I^2R losses. However, in actual implementation, we can control the charging and discharging process through pulse width modulation (PWM) of the switches to make this process more smooth so that the losses can be reduced dramatically. In particular, we can use a current regulator to regulate the actual charging/discharging current to a reference signal.

During the charging and discharging process, there exists bidirectional power flow. Assume we are charging the device voltage from $-V_m$ to V_m, then from $-V_m$ to 0, the energy is flowing out of the device with the amount $\frac{1}{2}C'V_m^2$, and from $-V_m$ to 0, the energy is flowing into the device with the same amount of $\frac{1}{2}C'V_m^2$. There will be no net energy transfer during this process if the circuit efficiency is unity, however, in practice the efficiency can not achieve unity, and so certain amount of energy will be lost during this process. Generally, the circuit efficiency during the voltage transition period will be lower than that during the continuous conduction period, because during the voltage transition period, there is a large charging/discharging current resulting in large conduction losses, and also there will be switching losses associated with the PWM-controlled switches. While during the continuous conduction period, the piezoelectric current is usually very low, and there is no action of the switches.

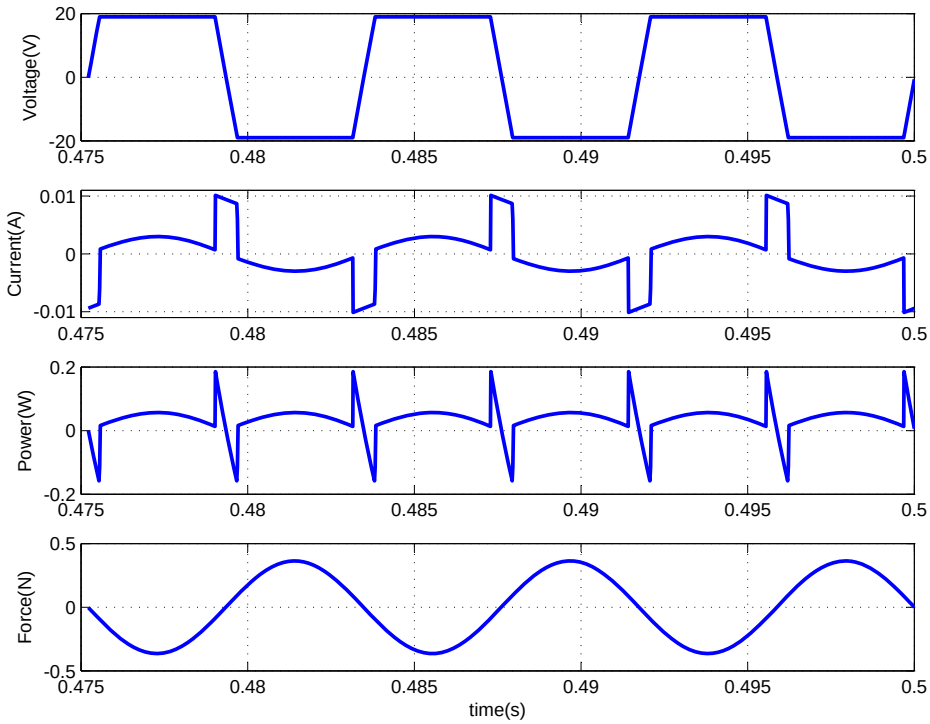

Figure 4.9. Waveforms of voltage, current, instantaneous power, and force

4.4 Comparison of Active Technique with Parallel SSHI Technique

The active technique has certain similarity with the parallel SSHI technique in that at natural frequency of the system, both the techniques control the applied voltage in the same way that they both perform voltage transition at the peak values of the device displacement, as mentioned previously. And we also showed that the maximum power harvested by parallel SSHI technique will be the same as that of the active technique at natural frequency if the inductor is ideal. Therefore, someone may wonder what is the benefit of the active technique compared to the parallel SSHI technique for systems operating exactly at the natural frequency, as will be discussed in the following.

We have mentioned that for the SSHI circuits, when the switch is turned on, the inductance and the device capacitance establish an L-C oscillation circuit for a

half period, resulting in a fast voltage sign inversion on the piezoelectric element. In practice, the inductor in the parallel SSHI circuit can not be ideal, so that the voltage inversion is not perfect, and certain amount of power will be lost on the series resistor of the inductor. A model of the LC oscillation circuit is shown in Fig. 4.10.

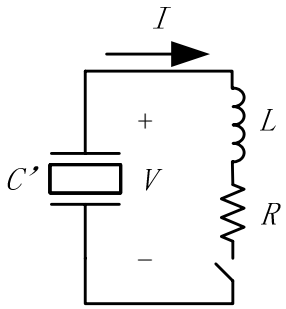

Figure 4.10. LC oscillation circuit for parallel SSHI circuit

When the switch is on, we have the following dynamic equation

$$LC\frac{d^2V}{dt^2} + RC'\frac{dV}{dt} + V = 0. \tag{4.25}$$

The general solution of (4.25) is

$$V(t) = e^{-\alpha t}(V_C cos\omega_d t + V_S sin\omega_d t), \tag{4.26}$$

where $\alpha = \frac{R}{2L}$, $\omega_r = \frac{1}{\sqrt{LC'}}$ is the LC resonance frequency, $\epsilon = \frac{\alpha}{\omega_r}$, and $\omega_d = \sqrt{1-\epsilon^2}\omega_r$. Assuming the displacement of the device will remain the same during the LC oscillation, the corresponding current flowing out of the piezoelectric device is then given by

$$I(t) = -C'\frac{dV}{dt} = -C'e^{-\alpha t}[-\alpha(V_C cos\omega_d t + V_S sin\omega_d t) + \omega_d(-V_C sin\omega_d t + V_S cos\omega_d t)]. \tag{4.27}$$

Since the initial current $I_{t=0} = 0$, from (4.27) we have

$$-\alpha V_C + \omega_d V_S = 0 \;\Rightarrow\; V_s = \frac{\alpha}{\omega_d}V_C. \tag{4.28}$$

So the piezoelectric voltage becomes

$$V(t) = e^{-\alpha t} V_0 (cos\omega_d t + \frac{\alpha}{\omega_d} sin\omega_d t), \tag{4.29}$$

where V_0=V_C is the initial value of the piezoelectric voltage at $t = 0$, which is also the bus voltage of the diode-bridge. And the output current will then becomes

$$I(t) = e^{-\alpha t} \frac{V_0}{Z_0} sin\omega_d t, \tag{4.30}$$

where $Z_0 = \frac{1}{C(\omega_d + \frac{\alpha^2}{\omega_d})} \approx \sqrt{\frac{L}{C}}$.

The switch will be reopened after half the resonance cycle, and the time interval will be $\frac{\pi}{\omega_n}$. The resulting reversed voltage is given by

$$V_r = V(\frac{\pi}{\omega_n}) = V_0 e^{-\alpha \frac{\pi}{\omega_n}} = V_0 e^{-\frac{\pi}{2Q_f}}, \tag{4.31}$$

where Q_f is the quality factor of the inductor. The reversed voltage then needs to be charged up to the bus voltage before the diode-bridge can conduct. The voltage difference is

$$\Delta V = V_0 - V_0 e^{-\frac{\pi}{2Q_f}} = V_0 (1 - e^{-\frac{\pi}{2Q_f}}). \tag{4.32}$$

As referred in [43], the optimal bus voltage is given by

$$V_{opt} = \frac{V_{OC}}{1 - e^{-\frac{\pi}{2Q_f}}}. \tag{4.33}$$

By substituting V_{opt} as V_0 in (4.32), we have $\Delta V = V_{OC}$, and so a voltage value of V_{OC} needs to be charged up after the voltage inversion.

During the charging process of the piezoelectric capacitor, Q remains constant, and so from $Q = C'V + kd\delta$, the change of the device displacement will be δ_m, which is the magnitude of the displacement. Since the displacement will be at its peak values during voltage inversion, so it will take a quarter of the cycle for the displacement to change δ_m. During this time, no energy is harvested. In contrast, in the active technique, the voltage is always fully reversed through the full-bridge converter, and so there will be energy flowing out of the device all the time except the voltage transition interval. The comparison of the piezoelectric voltage

and current waveforms of the active technique and the parallel SSHI technique is shown in Fig. 4.11. The waveforms of the DC voltage and current of the active technique are also compared with that of the parallel SSHI technique in Fig. 4.12. Therefore, if we assume the same energy transfer and same DC voltage for the two techniques, the active technique will have lower conduction loss, because the longer the current conducts, the lower the current magnitude will be, and so the smaller the conduction loss will be.

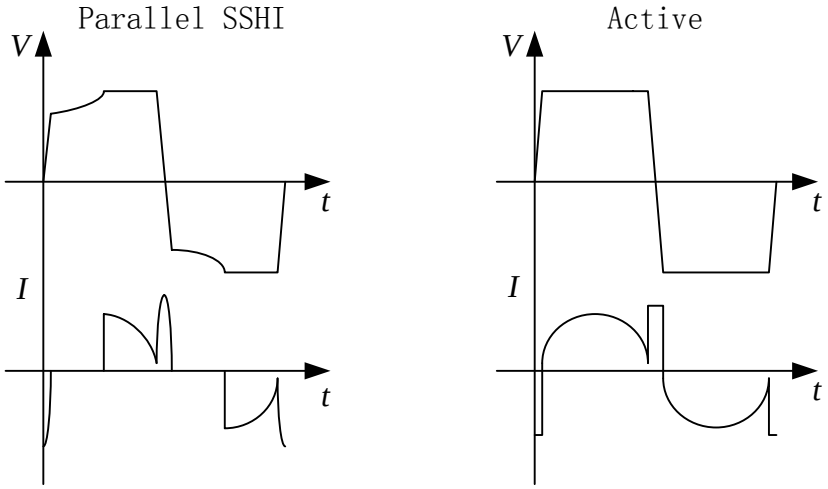

Figure 4.11. Waveforms of piezoelectric voltage and current for parallel SSHI and active techniques

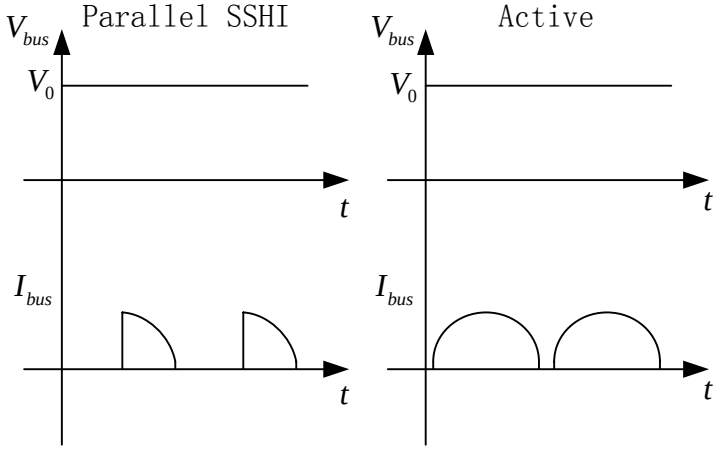

Figure 4.12. Waveforms of DC bus voltage and current for parallel SSHI and active techniques

The I^2R losses during the voltage inversion of the parallel SSHI technique is

also a big concern because, during LC oscillation, the peak current may be high enough to cause a large amount of power loss in the series resistance of the inductor. Neglecting the change in current magnitude, the energy consumption during the voltage inversion interval can be expressed as

$$\begin{aligned} W_{SSHI} &= \int_0^{\frac{\pi}{\omega_r}} I(t)^2 R dt \\ &= \int_0^{\frac{\pi}{\omega_r}} (e^{-\alpha t}\frac{V_0}{Z_0} sin\omega_d t)^2 R dt \\ &= \int_0^{\frac{\pi}{\omega_r}} (\frac{V_0}{Z_0} sin\omega_r t)^2 R dt \\ &= \frac{\pi R C' V_0^2}{2\omega_r L}. \end{aligned} \tag{4.34}$$

The associated power loss is then given by

$$P_{SSHI} = 2fW_{SSHI} = \frac{f\pi R C' V_0^2}{\omega_r L}, \tag{4.35}$$

where f is the excitation frequency.

In the active technique, we can limit the charging/discharging current by PWM control of the low-side switches in the full-bridge converter, as mentioned. Assuming the same bus voltage as the parallel SSHI technique, the total electrical charge during the voltage transition period is $Q = 2V_0C'$. By applying the PWM control, we can potentially control the time interval Δt during which this amount of charge is transferred. Ideally, if we assume the charging/discharging current is constant during the time interval, the current will be

$$I = \frac{Q}{\Delta t} = \frac{2V_0 C'}{\Delta t}. \tag{4.36}$$

Assuming the same equivalent resistance R as the parallel SSHI technique, the I^2R energy loss during this process can be calculated by

$$W_{Active} = I^2 R \Delta t = \frac{4V_0^2 C'^2 R}{\Delta t}, \tag{4.37}$$

and the associated power consumption is given by

$$P_{Active} = 2fW_{Active} = \frac{8fV_0^2C'^2R}{\Delta t}. \tag{4.38}$$

The ratio of the power loss of the parallel SSHI technique during voltage inversion to that of the active technique during the voltage transition period is then calculated as

$$Ratio = \frac{\pi}{8}\omega_n\Delta t = \frac{\pi\Delta t}{8\sqrt{LC'}}. \tag{4.39}$$

In our application, $C' = 0.166\mu F$, the natural excitation frequency is $f = 121Hz$, and if we assume the time interval $\Delta t = \frac{1}{20f} = 413\mu s$ and the inductor in parallel SSHI technique is $L = 10mH$, the ratio is approximately 4. Therefore, by controlling the time interval Δt, the I^2R loss of the active technique during the voltage transition period could be much smaller. It should be noted that, by controlling the voltage transition, the switching loss of the active technique will be larger than that of the parallel SSHI technique.

Finally, the typical circuit implementation of the parallel SSHI technique is shown in Fig. 4.13, in which 2 MOSFETs and 2 diodes are needed for the switch in parallel with the piezoelectric device, and so there are 6 diodes and 2 MOSFETs in total for the parallel SSHI circuit. Diode $D5$ and $D6$ can potentially be removed by closing and opening the switches properly, but they are often necessary to simplify the control of the switches. The diodes in the bridge can also be replaced by MOSFETs with synchronous rectification, but the control will be more complicated. So generally, during the voltage inversion, there will be 1 MOSFET and 1 diode in operation, while during the conduction period, there will be 2 diodes in the diode-bridge in operation. In contrast, for the active technique, the circuit only consists of 4 MOSFETs, and there will be 2 MOSFETs in operation during both the voltage transition period and the continuous conduction period. For piezoelectric energy harvesting, the output current level is usually very low, and so the MOSFET has much lower voltage drop than the diode according to Fig. 4.14. Hence, the active technique should be much more efficient than the parallel SSHI technique.

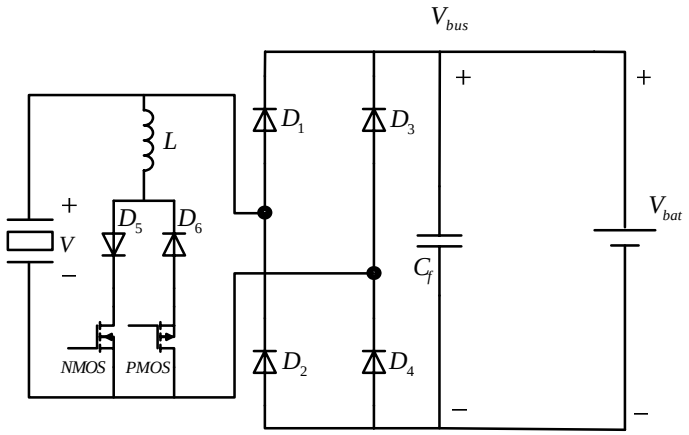

Figure 4.13. Circuit implementation of parallel SSHI circuit

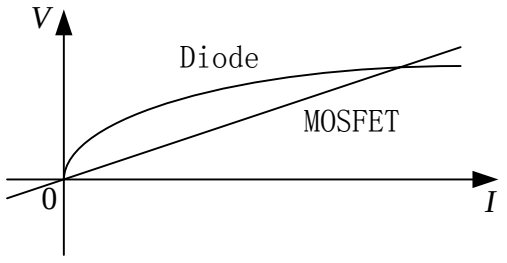

Figure 4.14. $V - I$ characteristic of MOSFET and diode

Chapter 5

Circuit Implementation and Loss Analysis

The active energy harvesting technique needs to be realized in a stand-alone circuit board for real application. In the following sections, the circuits used to implement the active energy harvesting technique are proposed and the selection of circuit components are discussed. The loss mechanisms associated with the power electronic interface circuit are also analyzed.

5.1 Circuit Implementation

The main interface circuit is designed to be a power electronic bidirectional full-bridge converter followed by a flyback DC-DC converter, as shown in Fig. 5.1. The flyback converter is used to generate the bus voltage of the full-bridge converter. The optimal voltage magnitude determined by the mentioned adaptive control algorithm is used as the bus voltage and is then used to determine the duty cycle of the transistor T, which was a N-channel MOSFET $IRF7853$ by $International\ Rectifiers$ in the implementation. Since the power levels associated with energy harvesting are relatively low, discontinuous conduction mode (DCM) of the flyback converter is assumed. The model of the flyback converter is well known by modeling the transformer as an ideal transformer with a magnetizing inductance L [53]. We denote the duty cycle as D, the current decrease time as Δ_1, the optimal bus voltage as V_{opt}, the battery voltage as V_{bat}, the switching

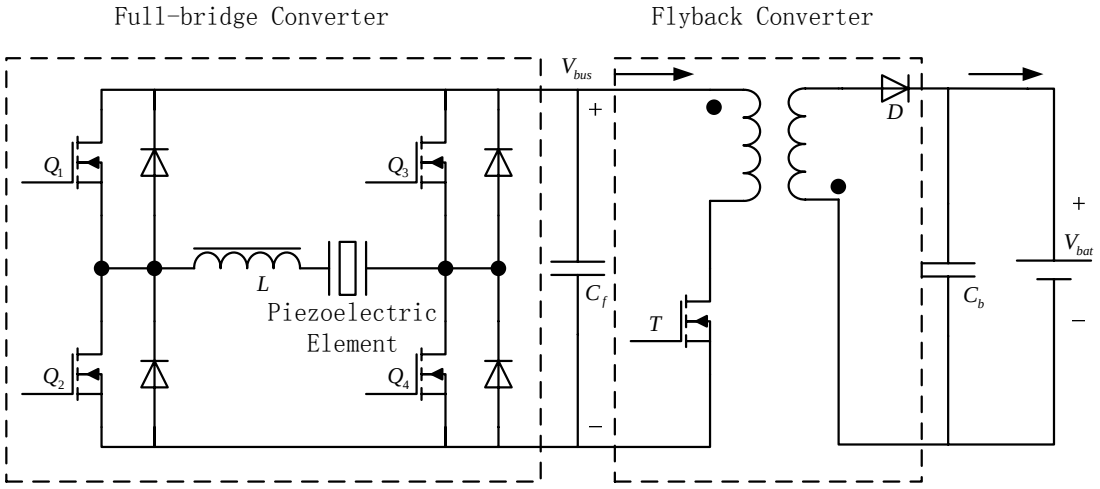

Figure 5.1. Bidirectional full bridge inverter with flyback converter

frequency as f_s, and the turns ratio of the transformer as N_1/N_2, then by applying the voltage-second balance for the magnetizing inductor, we have

$$V_{opt}DT_s - \frac{N_1}{N_2}V_{bat}\Delta_1 T_s = 0 \Rightarrow D = \frac{V_{bat}}{V_{opt}}\frac{N_1}{N_2}\Delta_1. \tag{5.1}$$

The average output current I_o is equal to the average diode current I_D since there is no DC capacitor current, and so we can relate the average output current with the peak magnetizing inductor current $i_{L(peak)}$ as

$$\begin{aligned} i_{L(peak)} &= \frac{N_1}{N_2}\frac{V_{bat}}{L}\Delta_1 T_s \\ I_o = I_D &= \frac{1}{2}\frac{N_1}{N_2}i_{L(peak)}\Delta_1 \\ &\Rightarrow \\ \Delta_1 &= \sqrt{\frac{2I_o f_s L}{V_{bat}}}\frac{N_2}{N_1}. \end{aligned} \tag{5.2}$$

By substitute (5.2) into (5.1), the duty cycle is given by

$$D = \frac{\sqrt{2I_o f_s L V_{bat}}}{V_{opt}}, \tag{5.3}$$

noting that the duty cycle is independent of the transformer turns ratio.

In actual implementation, however, the optimal duty cycle is hard to accurately estimate because the circuit efficiency is not unity, and so it is often experimentally determined. But (5.3) can still provide us some guidance on the approximate value of the optimal duty cycle. A PWM generation circuit with variable duty cycle was developed to experimentally find the optimal duty cycle, as shown in Fig. 5.2. Assuming the comparator is powered by a single DC source V_C and ground, which

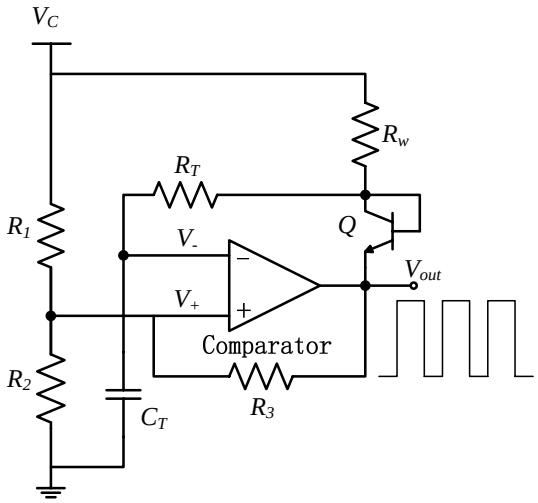

Figure 5.2. PWM generation circuit

means the comparator output will be either V_C or 0. The threshold voltage of the comparator is determined by the combination of resistors R_1, R_2 and R_3. When the output is $0V$, the threshold voltage V_+ is

$$V_{+1} = \frac{R_2||R_3}{R_1 + R_2||R_3} V_C. \tag{5.4}$$

When the output is V_C, then the threshold voltage is

$$V_{+2} = \frac{R_2}{R_1 + R_2||R_3} V_C, \tag{5.5}$$

noting that $V_{+1} < V_{+2}$. Assuming the initial condition of the capacitor is $V_{C_T} = 0$, which yields $V_{out} = V_C$. Thus the transistor Q is off, the capacitor C_T is charged through resistor R_1 and R_w, and the time constant is $\tau_1 = (R_T + R_w)C_T$. When the voltage of the capacitor exceeds the value $V_+ = V_{+2}$, the output voltage flips ($V_{out} = 0$) and the transistor Q is on. Now $V_+ = V_{+1}$, and the capacitor is

discharging through resistor R_T with a time constant $\tau_2 = (R_T + R_Q)C_T$, where R_Q is the equivalent resistance of the transistor Q, until the voltage drops to V_{+1}. Resulting waveform of the PWM generator is shown in Fig 5.3. Since R_Q is very

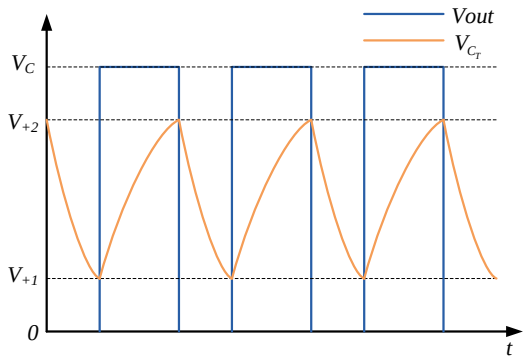

Figure 5.3. PWM Generator Waveform

small, generally we have $\tau_1 >= \tau_2$, and so the duty cycle of the PWM is always larger than 50%. To achieve a small duty cycle, R_w should be made much larger than R_T, and then the generated PWM with very large duty-cycle is fed into a inverter to obtain the desired small duty-cycle PWM. Through careful design and selection of components, especially the low power comparator, power consumption of this circuit can be extremely low. In the implementation, $TS3021$ by ST was chosen as the comparator for its high speed ($33ns$ propagation delay) and low power consumption ($64\mu A$ quiescent supply current). $DSS4320$ by $Diodes\ Incorporated$ was chosen as the NPN transistor. For the resistances, $R_1 = R_2 = R_3 = 100k\Omega$, $R_w = 10k\Omega$, and R_T was a potentiometer used to tune the duty-cycle of the PWM. The power consumption was measured to be $1.8mW$. It should be noted that although the duty-cycle of the circuit can be manually changed by tuning the parameters, it can not be adaptively changed. For cases where the optimal duty-cycle needs to be adaptively achieved, a dSPACE system or microcontroller will be used for generating the PWM signal, as will be discussed later.

The full-bridge converter is used to apply a piecewise-constant control voltage to the piezoelectric device. A filter inductor is placed in series with the piezoelectric device to smooth the current. Since we need to deal with high frequency switching, MOSFETs were chosen as the switches. Particularly, N-channel MOSFETs $ZVN3320$ by $ZETEX$ were applied. The switching of the four MOSFETs

in the full-bridge converter are controlled by the optimal voltage phase angle determined by the active technique, and complementary square-wave signals are needed to drive the MOSFETs. Generally, $Q1$ and $Q4$ need to be simultaneously on to apply a positive voltage to the piezoelectric device, while $Q2$ and $Q3$ need to be simultaneously on to apply a negative voltage to the piezoelectric device. The complementary square-wave drive signals can be generated from a single main drive signal. If we use the excitation force as the reference, the main drive signal can be generated by the circuit shown in Fig. 5.4. In Fig. 5.4, the non-inverting and

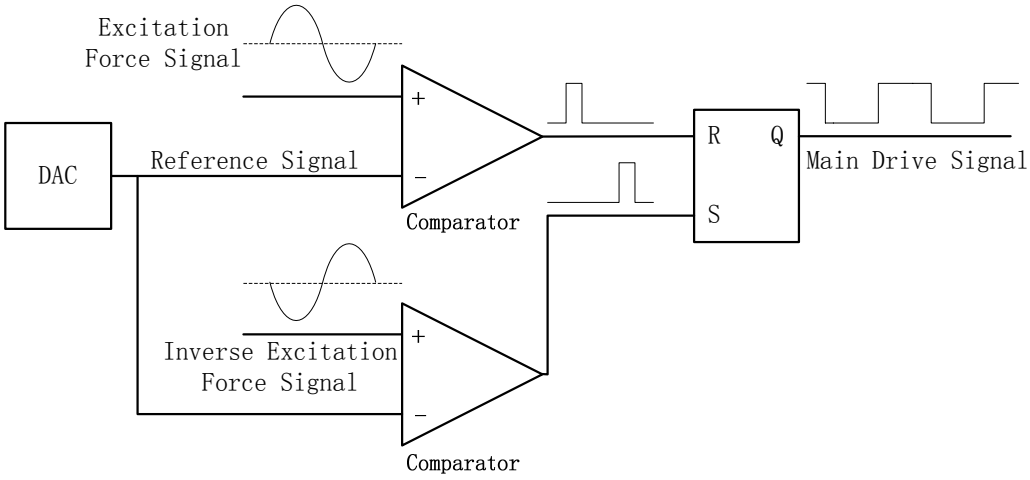

Figure 5.4. Circuit to generate the main drive signal

inverting excitation force signals are compared with a reference signal to generate two pulse signals that are 180° out of phase. These two pulse signals are then fed into an RS trigger to generate the square-wave main drive signal. The excitation force signal can be obtained from the base acceleration, which can be measured by accelerometers. The phase angle between the main drive signal and the excitation force is determined by the reference signal, which can be generated by a digital-to-analog converter (DAC) by pre-programming it with the desired value. The optimal phase angle can be calculated by (4.15), but in practice it is often experimentally determined by changing the reference voltage until the maximum power is harvested. The optimal phase angle can also be adaptively achieved by connecting and programming the DAC with a microcontroller, as will be discussed in the next chapter. In the implementation, a $TS862$ by ST was chosen as the comparator for its ultra-low power consumption ($6\mu A$ quiescent supply current),

an $AD5300$ by *Analog Devices* was chosen as the DAC for its simplicity and low power consumption ($140\mu A$ quiescent supply current), and a dual-NOR gate $SN74LVC2G02$ by *Texas Instruments* was used to build the RS trigger. The power consumption of the circuit was measured to be $2mW$.

To avoid the simultaneous turn-on of the two switches in the same bridge arm, an extra circuit is needed to provide dead-time insertion to the complementary square-wave drive signals, as shown in Fig. 5.5. Typical waveforms at every output port are also shown in the figure. The diode-R-C circuit at the first stage of the

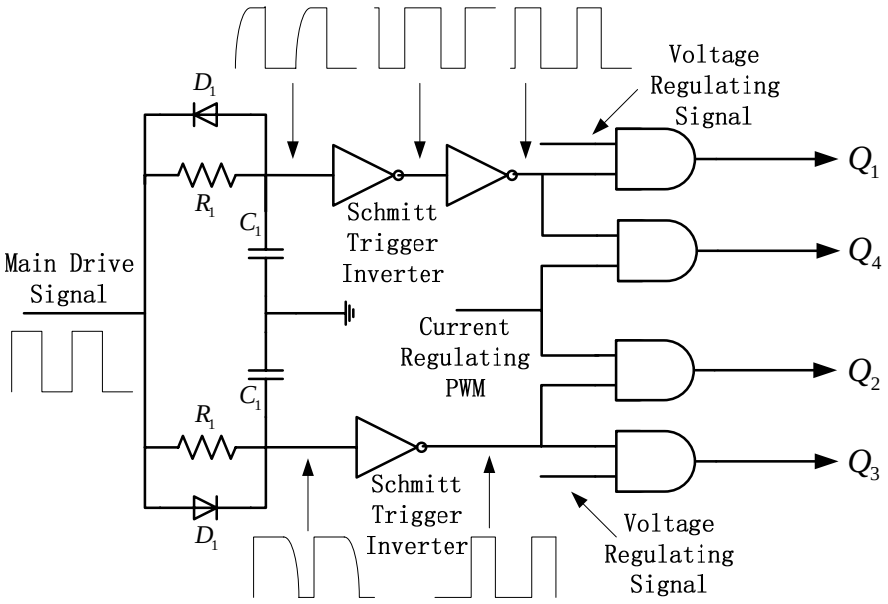

Figure 5.5. Dead-time generation circuit

circuit is inserted to provide a time delay for the input signals. The time interval between the input signal and the output signal is determined by the RC time constant and the threshold voltage of the Schmitt trigger inverter, noticing that the output voltage of the Schmitt trigger inverter is established after the voltage of the capacitor reaches the threshold value. This time delay will be the dead time between the MOSFET switches and can be calculated as

$$t_{dead} = -\tau \cdot \ln\left(1 - \frac{V_{th}}{V_s}\right), \tag{5.6}$$

where $\tau = R_1 \cdot C_1$ is the time constant of the RC pair, V_{th} is the threshold voltage of the Schmitt trigger inverter, and V_s is the magnitude of the input

drive signal. In the implementation, a $SN74LVC3G14$ and a $SN74AHCT08$ by $Texas\ Instruments$ were chosen as the Schmitt-trigger inverter and the AND gate, respectively. The resistance value was $R_1 = 100k\Omega$, the capacitance value was $C_1 = 1nF$, and the threshold voltage of the Schmitt-trigger inverter was about $V_{th} = 3V$, giving a dead-time of about $0.1ms$. The power consumption of this circuit was measured to be about $1mW$. A typical experimental result is shown in Fig. 5.6, in which the black line is the original main drive signal, the blue line is the non-inverting drive signal, and red line is the inverting drive signal. The result shows that there is no overlap of the non-inverting and inverting square-wave drive signal waveforms, and so the two switches in each half-bridge will not be simultaneously on.

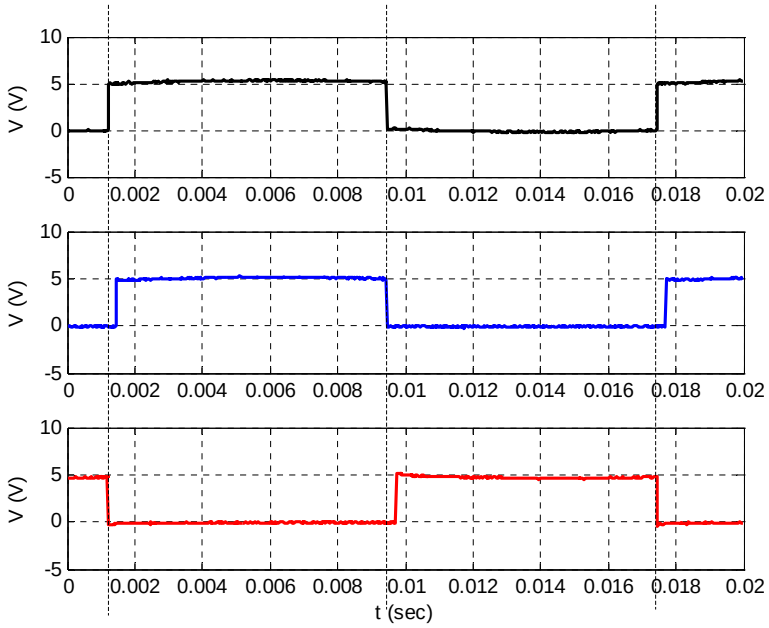

Figure 5.6. Experimental result of dead-time generation circuit, from top to bottom: main drive signal, non-inverting drive signal, and inverting drive signal

In Fig. 5.5 the current regulating PWM is used to control the voltage transition rate on the piezoelectric device. As mentioned in Chapter 4, there may be a large charging/discharging current during the voltage transition process resulting in large I^2R loss, so we seek to limit the charging/discharging current through a current regulator.

A simple hysteresis current regulator was first developed, as shown in Fig. 5.7.

Similar to the comparator in Fig. 5.2, the threshold voltage of the comparator is determined by the combination of resistors R_1, R_2 and R_3. When the output is $0V$, the threshold voltage V_+ is

$$V_{+1} = \frac{R_2||R_3}{R_1 + R_2||R_3} V_C, \tag{5.7}$$

and when the output is V_C, then the threshold voltage is

$$V_{+2} = \frac{R_2}{R_1 + R_2||R_3} V_C. \tag{5.8}$$

During the continuous conduction period, the output current is usually very low, and so the comparator outputs a high-level signal and ensures that the low-side MOSFETs are always on. During the voltage transition period, once the actual current reaches the threshold V_{+2}, the comparator outputs low, and the corresponding low side MOSFET will be turned off, resulting in the decrease of the current until the current hits the lower threshold V_{+1}. The output of the comparator will then be high again and the MOSFET is turned on again. The advantage of the current regulator is that it is simple and has very low power consumption. By choosing a $TS3022$ by ST as the comparator, the power consumption was measured to be $0.7mW$. The drawback is that the switching frequency is not fixed and the performance relies on the comparator.

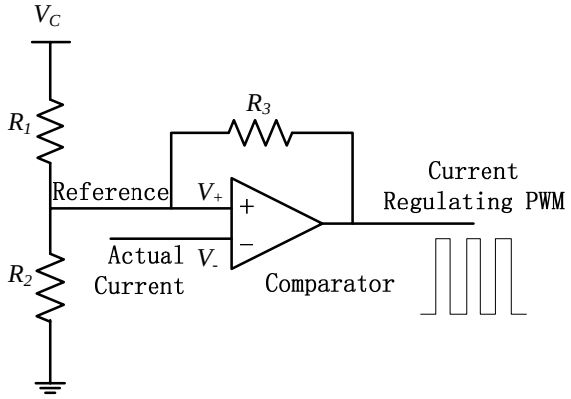

Figure 5.7. Hysteresis current regulator

A standard peak-current regulator with stabilizing ramp was also built to limit the charging/discharging current during voltage transition, as shown in Fig. 5.8.

A 555 timer was used to generate both a trigger signal for the RS trigger and a

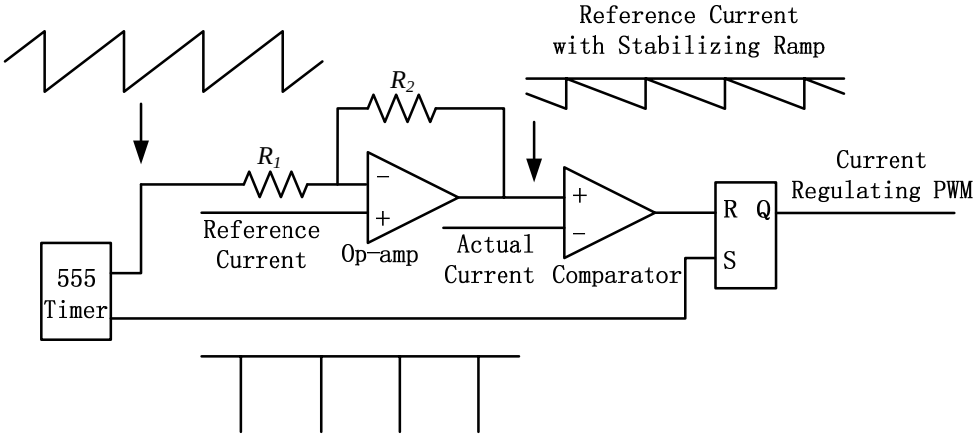

Figure 5.8. Peak current regulator with stabilizing ramp

sawtooth wave was used to generate the stabilizing ramp to stabilize the control. During the operation, the trigger signal will periodically make the output of the RS trigger high to turn on the MOSFET, so that we can control the switching frequency of the MOSFET by controlling the frequency of the trigger signal. At the continuous conducting period, the output piezoelectric current will be less than the reference and so the output of the RS trigger will stay high and the MOSFET is continuously on; while at the voltage transition period, once the charging/discharging current is higher than the reference, the comparator will generate a low signal, which will make the output of the RS trigger low, and the MOSFET is then turned off, until the next trigger signal comes. In the implementation, a NAND gate $SN74AHCT00$ by *Texas Instruments* was used to construct the RS trigger, a $TS3022$ by ST was chosen as the comparator, and a $TL062$ by ST was chosen as the op-amp for its lower power consumption ($200\mu A$ quiescent supply current) and high slew-rate ($3.5V/\mu s$). $R_1 = 100k\Omega$ and $R_2 = 10k\Omega$ gives a ratio of 0.1 for the stabilizing ramp. The drawback of this design is that the 555 timer is consuming a significant amount of power (about $18mW$). The current regulating PWM signal is then combined with the complementary square-wave drive signals as in Fig. 5.5 and fed into the low side MOSFETs of the full-bridge converter.

The drive signal for high-side MOSFETs also needs to be regulated, because at the discharging process of the voltage transition, for example, the voltage is discharging from positive to zero, the square-wave drive signal for MOSFETs $Q1$

and $Q4$ will become low and the drive signal for MOSFETs $Q2$ and $Q3$ will become high. If we feed the square-wave drive signal directly to $Q3$, there will be a short-circuit path consisting of the parallel diode of $Q1$ and MOSFET $Q3$ between the positive and negative side of the piezoelectric device. This short path will cause a very large discharging current of the piezoelectric device until the voltage across the device becomes zero. To avoid this, we need to regulate the drive signal to $Q3$ so that it will only be turned on when the voltage across the piezoelectric device drops to some value close to zero. The similar control also needs to be applied to MOSFET $Q1$ when the voltage changes from negative to positive. A comparator ($TS862$) can be used to compare the piezoelectric voltage to a reference signal (close to zero), as shown in Fig. 5.9, to generate the voltage regulating signal, which will only be high when the piezoelectric device discharges enough and the voltage is very low. This voltage regulating signal is then combined with the complementary square-wave drive signals to drive the high side MOSFETs. The measured power consumption of the voltage regulating circuit was $0.3mW$.

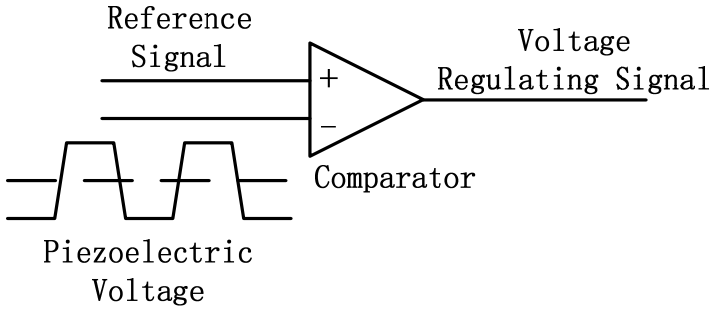

Figure 5.9. Voltage regulation circuit

A gate drive circuit was then developed to drive the MOSFETs in the full-bridge converter. For the low-side MOSFETs, the output signal from the logic gates can be directly used to drive the MOSFETs. However, for the high-side MOSFETs, the drive is a bit complicated. The pulse-transformer-based high-side gate driver referred by Tian in [2] was first developed and tested, as shown in Fig. 5.10. The principle of the circuit can be found in [2], and in short, when the input drive signal is high, the capacitor C_{out} will have a high voltage to turn on the MOSFET, and when the input drive signal is low, the capacitor C_{out} will discharge to turn off the MOSFET. However, the capacitance C_{out} needs to be

large enough to make the diode-bridge output voltage stable to turn on the high-side MOSFET while the input signal is high, but when the drive signal becomes low, it will then take a very long time for the capacitor C_{out} to discharge, and so the MOSFET can not be turned off properly and short-circuit may happen for each bridge branch of the full-bridge converter. The decrease of the resistor R may shorten the discharging time, but the voltage of the capacitor when charged will have more ripple. Hence in our design we still use a half-bridge gate driver IC ($IRS2003$ by $International\ Rectifiers$) with an isolated power supply ($VBSD1-S5-S5$ by $V-infinity$). The power consumption of the isolated power supply is very high (about $300mW$). Currently our focus is on realizing the active energy harvesting idea, and in the future we will focus on developing a better gate drive circuit.

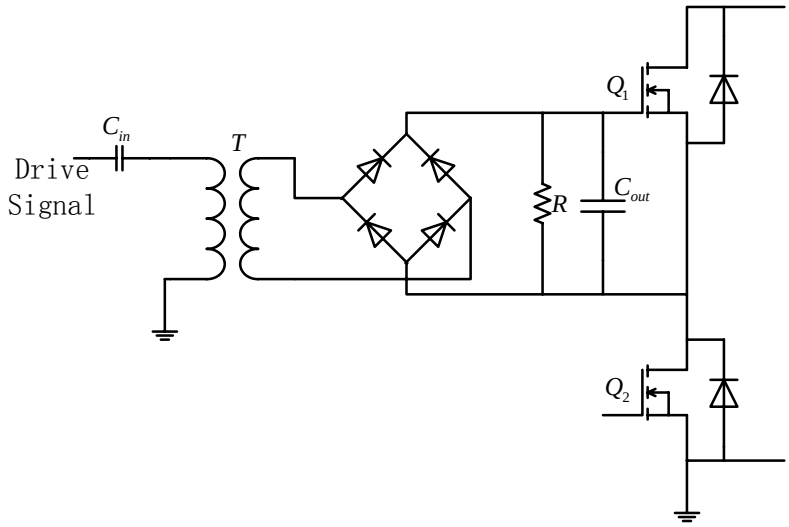

Figure 5.10. Pulse transformer based gate drive circuit for high-side MOSFETs

By applying the above control strategy, the typical waveform of the piezoelectric voltage is shown in Fig. 5.11. The waveforms can be divided into 6 stages for one period. Stages 1 and 4 are called the continuous conduction periods, and stages 2, 3, 5, and 6 are called the voltage transition periods.

At stage 1, MOSFETs $Q1$ and $Q4$ are on, $Q2$ and $Q3$ are off, the voltage across the piezoelectric device will be positive and equal to the bus voltage. At stage 2, MOSFETs $Q1$, $Q3$, and $Q4$ are off, and $Q2$ is PWM-controlled. When $Q2$ is on, the piezoelectric device is discharging through $Q2$ and the diode in parallel

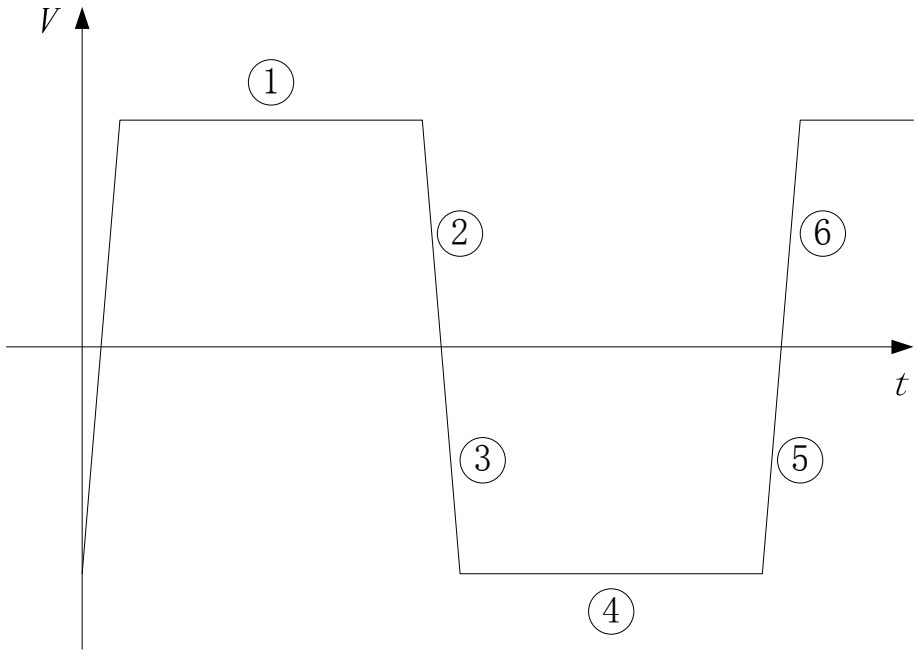

Figure 5.11. Typical voltage waveform of the piezoelectric device

with $Q4$ until the discharging current reaches a certain reference. $Q2$ will then be turned off, and the discharging current decreases through the diodes in parallel with $Q1$ and $Q4$. At stage 3, MOSFETs $Q1$ and $Q4$ are off, $Q3$ is on, and $Q2$ is PWM-controlled. When $Q2$ is on, the piezoelectric device is charged from the bus through $Q2$ and $Q3$ until the charging current reaches a certain reference. $Q2$ will then be turned off, and the charging current decreases through $Q3$ and the diode in parallel with $Q1$. Similarly, at stage 4, $Q2$ and $Q3$ are on, $Q1$ and $Q4$ are off, the voltage across the piezoelectric device will be negative and equal to the bus voltage. At stage 5, MOSFETs $Q1$, $Q2$, and $Q3$ are off, and $Q4$ is PWM-controlled, and the piezoelectric device is discharging. Finally, at stage 6, MOSFETs $Q2$ and $Q3$ are off, $Q1$ is on, and $Q4$ is PWM-controlled, and the piezoelectric device is charged from the bus. The status of the MOSFETs and the current flow path for each stage is shown in Fig. 5.12, in which switches represent MOSFETs and arrows represent the current flow path.

To measure both the output battery current and piezoelectric current, a current sense circuit is necessary, and can be simply built by a differential amplifier with a sense resistance. A current sense IC was also considered; however, the power consumption of the chip might be a problem whereas a low-power op-amp is much

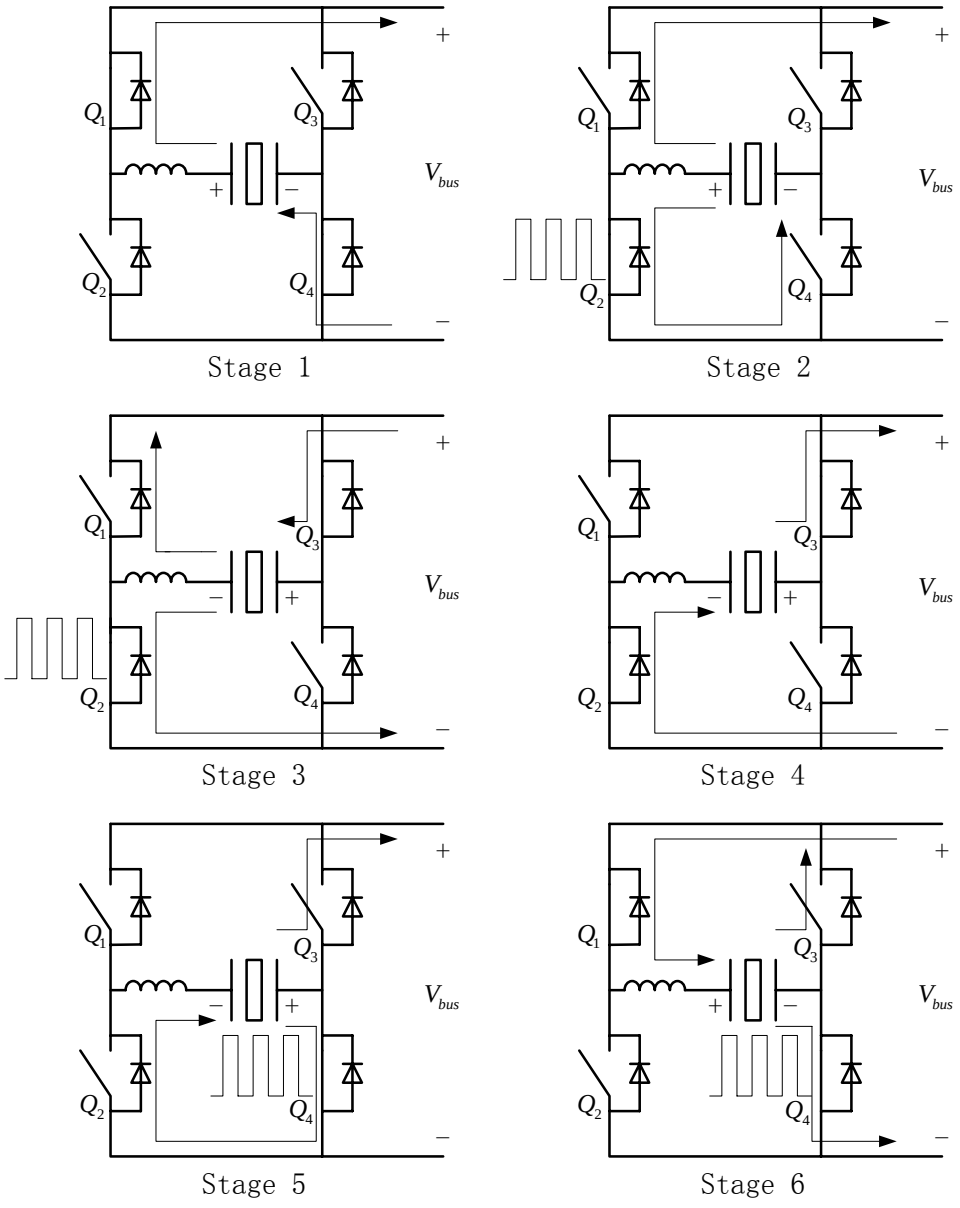

Figure 5.12. Status of MOSFETs and current flow path for each stage

easier to find. The piezoelectric voltage can also be measured through a differential amplifier. The circuit for sensing the piezoelectric output current is shown in Fig. 5.13 as an example, where the resistance values R_1 and R_2 must be chosen such that the voltages at the input pins of the op-amp do not exceed the positive or negative supply voltage of the op-amp. The relationship between the output voltage signal

u_o of the differential amplifier and the current I is then given by

$$u_o = \frac{R_2}{R_1} R_{sense} I. \tag{5.9}$$

In our implementation, a $TL062$ was again chosen as the op-amp for its low power

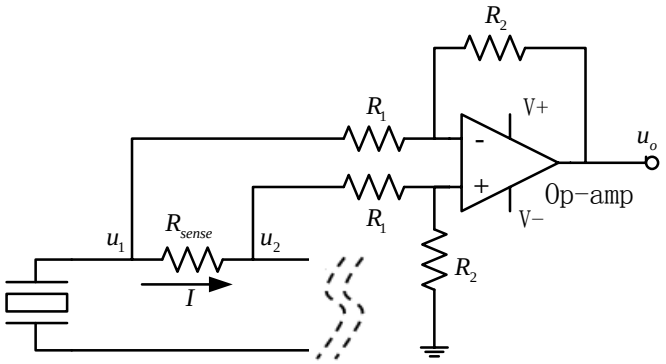

Figure 5.13. Differential amplifier for current sensing

consumption, and the total power consumption of the current and voltage sensing circuit was measured to be $15mW$. It should be noted that this part of the power consumption can be further reduced to a very low value through careful design.

A stand-alone PCB board was fabricated to implement the power electronic interface circuit and the associated control circuits, as shown in Fig. 5.14. Each functional circuit is also illustrated in the figure. The board is $4.2inches \times 3.4inches \times 1.0inches$ is size, and weights $57.2g$.

5.2 Power Loss Analysis of the Power Electronic Interface

The power loss of the full-bridge converter is an important factor that affects the energy harvesting ability of the circuit, as mentioned in Chapter 4. The MOSFETs of the full-bridge inverter are key components; besides satisfying the voltage and current rating, the parameters such as gate charge Q_g, rise and fall time t_r,t_f are also critical. An N-channel MOSFET $ZVN3320$ was chosen for the full-bridge because it has a voltage rating of $200V$ and current rating of $60mA$, perfect for

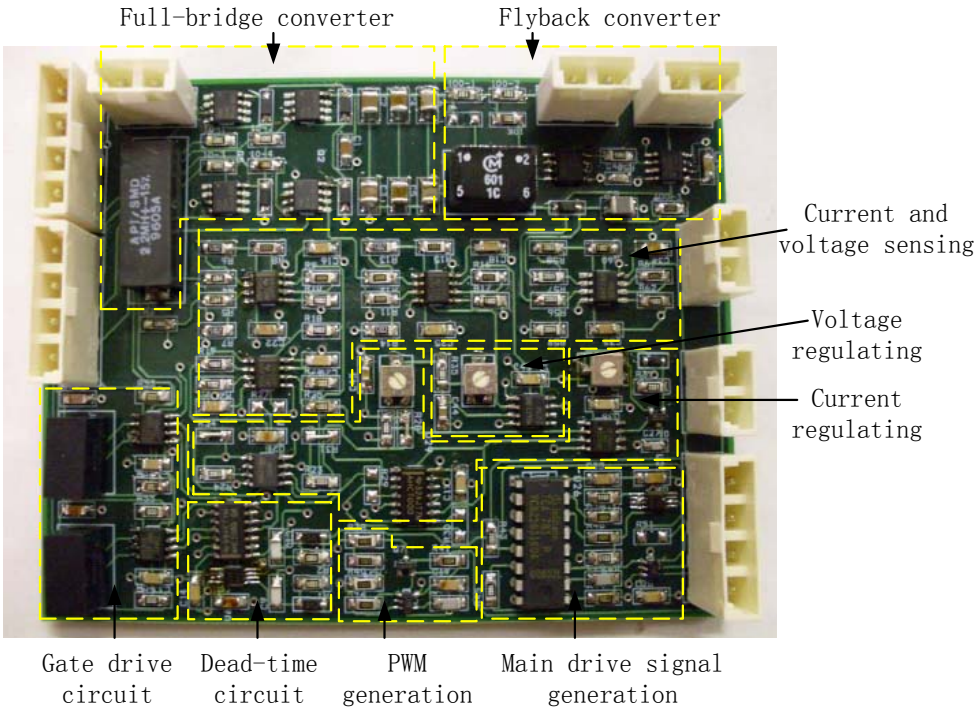

Figure 5.14. Stand-alone PCB board for active energy harvesting

our application, and it also features very fast turn-on and turn-off time and low input impedance.

The losses associated with the full-bridge converter mainly consist of the switching loss and conduction loss. Switching loss imposes an upper limit on the switching frequencies of practical converters. During the switching transitions, the MOSFET's voltage and current are simultaneously large. In consequence, the MOSFET experiences high instantaneous power loss. The switching loss of the power MOSFET is estimated as

$$P_{sw} = \frac{1}{2} f_s V_{DS} I_D (t_r + t_f), \tag{5.10}$$

where f_s is the switching frequency, V_{DS} is the drain to source voltage of the MOSFET when off, I_D is the current flowing through the drain-source of the MOSFET when on, and t_r, t_f are the voltage rise and fall time.

For our application, the four MOSFETs in the full-bridge converter are continuously "on" or "off" at the continuous conduction period, and so there is no switching loss most of the time. The switching loss will only be generated during the voltage transition period at which the charging/discharging current of the

piezoelectric device needs to be PWM regulated. The switching frequency for the low-side MOSFETs was set to $50kHz$ during voltage transition. The turn-on time of the MOSFET was measured to be $150ns$ and the turn-off time was measured to be $25ns$. So the switching frequency can be determined with the voltage and current waveforms during the voltage transition period.

Conduction loss can be separated into two parts; one is the resistive heat dissipation during a switch turn-on state, the other is due to the diode forward voltage drop. The on-state conduction loss of the power MOSFET is calculated as

$$P_{con1} = f_s I_D^2 R_{on} t_{on}, \tag{5.11}$$

where R_{on} is the total resistance between the source and drain during the on state, and t_{on} is the turn-on time in one cycle. The power loss due to diode forward voltage drop is calculated as,

$$P_{con2} = f_s V_{DS} I_D t_d, \tag{5.12}$$

where t_d is the diode conducting time in one cycle.

For our application, at the continuous conduction period, the conduction loss is dissipated in two MOSFETs. The on-state resistance of $ZVN3320$ is evaluated to be 25Ω, and so the total resistance during the continuous conduction period is 50Ω. At the voltage transition period, from the previous analysis of the 6 stages, it can be shown that at the discharging period, when the low-side MOSFET is on, the conduction loss will be dissipated in the MOSFET and a diode, and when the MOSFET is off, the conduction loss will be dissipated in two diodes; at the charging period, when the low-side MOSFET is on, the conduction loss will be dissipated in two MOSFETs, and when the MOSFET is off, the conduction loss will be dissipated in the high-side MOSFET and a diode. To minimize the conduction loss, additional Schottky diodes were added in parallel with the four MOSFETs, and the forward voltage drop is estimated to be $V_{DS} = 0.35V$. Then with the current waveforms, the conduction loss can be calculated.

There are some other losses associated with the full-bridge converter. First, the resistor used to sense the output current and resistors in the differential amplifiers used to obtain the piezoelectric voltage and output current will also consume a

portion of power during operation. Since the current level associated with the piezoelectric device is pretty low (usually several mA), the sense resistor can not be very small. In our setup the resistance value was $R_{sense} = 10\Omega$, and so the power consumption can be evaluated by

$$P_{sense} = I_c^2 R_{sense}, \tag{5.13}$$

where I_c is the current flowing through it. The power consumed by the resistors in the differential amplifiers is determined by the voltage levels of the points they are connected to, and can be expressed as

$$P_{res} = \frac{V^2}{R_{res}}, \tag{5.14}$$

where V is the voltage, and R_{res} is the equivalent resistors in the differential amplifiers.

Secondly, there are losses associated with the filter inductor. A $2.7mH$ chip inductor was chosen for our application, which has a current rating of $250mA$ and a DC resistance of $R_{DC} = 5.8\Omega$. Since the current level of our application is much lower than the current rating, the core loss can be omitted, and so we only need to estimate by

$$P_{ind} = I_c^2 R_{DC}. \tag{5.15}$$

In our application the excitation frequency is around $120Hz$, and so there will not be too much of an increase of the inductor resistance during operation due to skin and proximity effect, and the DC resistance is therefore used for power loss estimation.

Finally, during the voltage transition period, when the piezoelectric capacitor is discharging, ideally the discharging power goes back to the bus. However, since the inductor is not ideal, there is a certain amount of power dissipated. When the piezoelectric capacitor is charged, the capacitor is always absorbing power from the bus, so that the output power is less than the input power during the voltage transition period, and the lost power is denoted as P_{cap}.

Hence the total power consumption associated with the full-bridge converter

can be estimated as

$$P = P_{sw} + P_{con1} + P_{con2} + P_{sense} + P_{res} + P_{ind} + P_{cap}. \tag{5.16}$$

Denoting P_{out} as the total output power, the overall efficiency of the full-bridge converter can be expressed as

$$\eta = \frac{P_{out}}{P_{out} + P}. \tag{5.17}$$

Especially, the circuit efficiency during the continuous conduction period can be evaluated by

$$\eta_{con} = \frac{P_{out}}{P_{out} + P_{con1} + P_{sense} + P_{res} + P_{ind}}, \tag{5.18}$$

noting that the above power loss terms are only associated with the loss during continuous conduction period.

Since there are two charging cycles and two discharging cycles per excitation frequency, the power transfer during voltage transition period can be expressed as

$$P_{tran} = f \times 4 \times \frac{1}{2} C' V^2, \tag{5.19}$$

in which f represents the excitation frequency and V is the capacitor voltage. And so the circuit efficiency during the voltage transition period can be evaluated by

$$\eta_{tran} = \frac{P_{tran} - P_{sw} - P_{con1} - P_{con2} - P_{sense} - P_{res} - P_{ind} - P_{cap}}{P_{tran}}, \tag{5.20}$$

again here the power loss terms are the loss during the voltage transition period. The power consumption of the full-bridge converter is extremely important because it is the bidirectional power flow interface, and its efficiency will greatly affect the power harvesting ability of the full-bridge converter.

For the flyback converter connected to the full-bridge converter, a transformer which has a turns ratio of $1:1$ and an inductance value of $L = 0.5mH$ was wound on a ferrite core. The current increasing rate of the primary side of the transformer can then be calculated by the bus voltage. The switching frequency was set to $f_s = 8kHz$, and depending on different duty-cycles the peak current will be different. An N-channel MOSFET $IRF7853$ was chosen as the transistor for its small on-

state resistance ($18m\Omega$) and large voltage and current ratings ($100V, 8.3A$), so the conduction loss associated with the MOSFET should be much smaller than the switching loss. The power loss associated with the flyback converter consists of the loss of the MOSFET, the loss of the transformer and the loss of the diode in the secondary side. The loss of the MOSFET and the diode can be estimated by using (5.10), (5.11), and (5.12). The loss associated with the transformer is a little complicated and can be determined by experiment.

Chapter 6

Experimental Results

6.1 Parameter Identification

The piezoelectric dynamic system was constructed by a commercial piezoelectric bimorph (QuickPack $QP20W$, *Midé Technology*) with a mini-shaker ($ES020$, *KCF Technologies*), as shown in Fig. 6.1. One end of the piezoelectric device was clamped to a shaker to form a base-driven cantilever, and an evenly-distributed proof mass ($m = 7g$) was mounted at the other end of the bimorph. To minimize the end effect of the clamp, the clamp piece was made much more massive compared to the end mass. A sinusoidal signal through a stereo amplifier was fed into the shaker to generate the excitation force. Three MEMS accelerometers ($ADXL78$ by *Analog Devices*) were attached to the shaker base, the clamp, and the end mass, respectively, to measure accelerations. The MEMS accelerometer is better than other types of measuring instruments because it is very light and inexpensive. The base acceleration of the piezoelectric system was measured by subtracting the clamp acceleration signal from the shaker base acceleration signal, and the relative acceleration of the end mass with respect to the clamp was evaluated by subtracting the end mass acceleration signal from the clamp acceleration signal. The natural frequency of the system was tuned to near $120Hz$ frequency, and the magnitude of the base acceleration was maintained at $B_a = 52m/s^2$ for all the excitation frequencies in all the experiments to emulate a sinusoidal force with constant-magnitude $F_m = mB_a = 0.364N$.

Short-circuit and open-circuit tests were first performed to obtain the param-

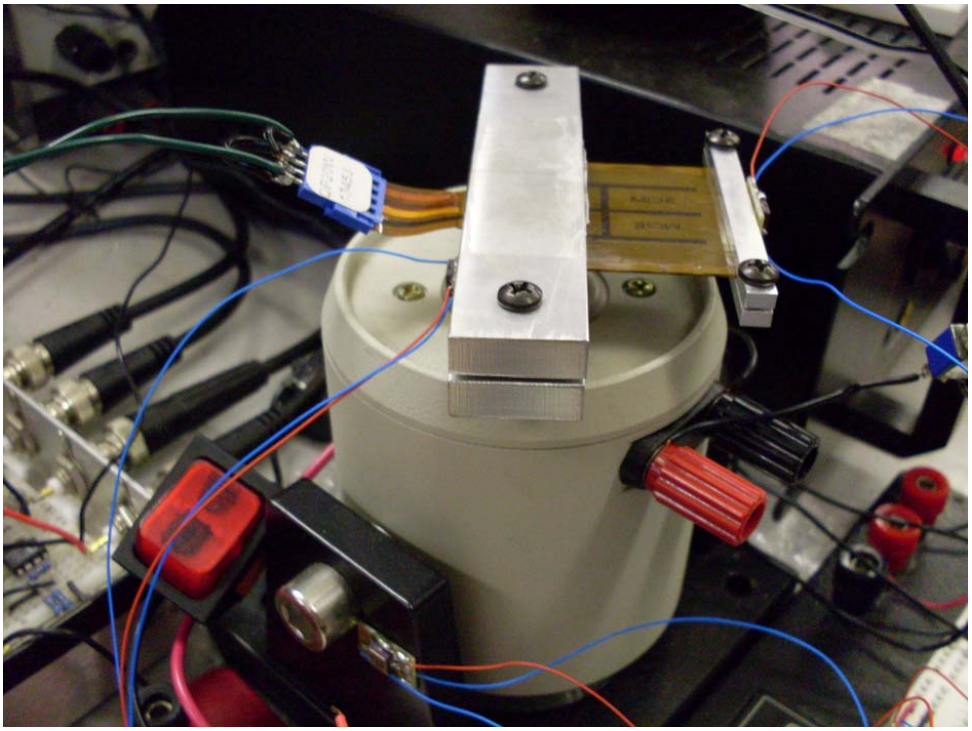

Figure 6.1. Experimental setup of the piezoelectric dynamic system

eters of the system. The peak value of relative acceleration of the tip mass with respect to the end clamp over a frequency range at the short-circuit and open-circuit conditions is shown in Fig. 6.2. The short-circuit resonance frequency can be read to be $121Hz$, and the peak value of relative acceleration is $597m/s^2$. The open-circuit resonance frequency is $126Hz$. The waveforms of base acceleration and relative acceleration at short-circuit resonance frequency are also shown in Fig. 6.3. The phase angle between the base acceleration and relative acceleration is $90°$, as expected.

According to Chapter 2, the ratio of the magnitude of relative displacement and base displacement is needed to get the damping ratio. Since the displacement can be obtained by double integration of the acceleration, and the relative displacement and base displacement have the same frequency, this ratio can also be obtained by using the magnitude of acceleration. The end mass was measured to be $7g$. For the piezoelectric bimorph, the two layers are connected in parallel and the capacitance under zero force was measured to be $0.18\mu F$. So all the parameters of the system can then be calculated, as listed in Table. 4.1.

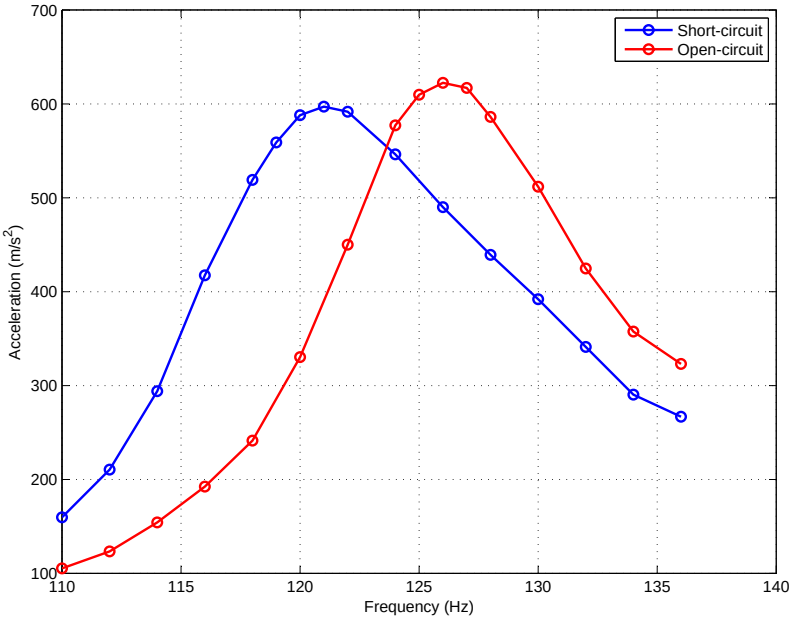

Figure 6.2. Short-circuit and open-circuit response of relative acceleration

To verify the estimated parameters, the theoretical short-circuit current and open-circuit voltage of the system can be calculated by (2.13) and (2.12) using the calculated parameters, which are then compared with the actual short-circuit current and open-circuit voltage obtained by the experiments, as shown in Figs. 6.4 (a) and 6.4 (b), respectively. The experimental results match the theoretical values very well, which indicates that the calculated parameters are reasonably accurate.

The theoretical maximum power that can be harvested from the system can be calculated to be $\frac{F_m^2}{8b} = 35.7mW$. The ratio $\frac{k_e^2}{\zeta}$ is about 2, which means this system is a relatively strongly-coupled system.

6.2 Full-bridge Converter with Resistive Load

To evaluate the potential energy harvesting ability of the active energy harvesting circuit, an experiment was first performed for the full-bridge converter with a resistive load connected, as shown in Fig. 6.5. The load resistance value was fixed to be $R_{load} = 10k\Omega$ and a power supply was used to establish the bus voltage. A

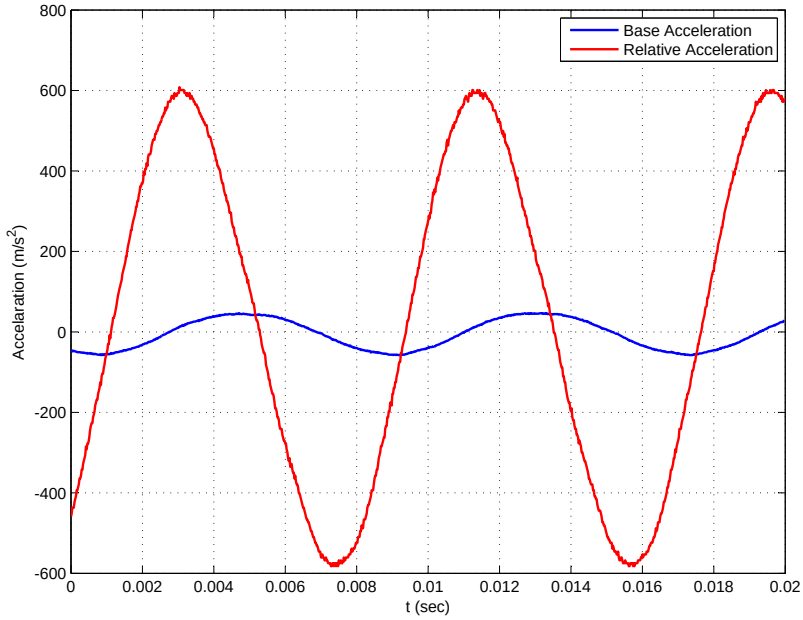

Figure 6.3. Waveforms of base acceleration and relative acceleration at short-circuit resonance frequency

sense resistor $R_{sense} = 100\Omega$ was placed in series with power supply to measure the output current, and so the harvested power can be estimated by

$$P_{harvested} = V_{bus}\frac{V_{bus} - V_{source}}{R_{sense}}. \tag{6.1}$$

In the experiment, the excitation frequency to the system was varied from $105Hz$ to $145Hz$, and since for practical application the theoretical optimal voltage magnitude and phase angle may not be the actual optimal condition due to the effect of circuit efficiency, we manually tuned the bus voltage and phase angle to find the maximum power harvesting at each frequency. The maximum harvested power at different frequencies is shown in Fig. 6.6. The power harvested by the active technique is not constant for all frequencies as predicted in the theory because the circuit efficiency is not 100%. The maximum power is measured to be $31.65mW$ at $124Hz$, compared to the theoretical maximum value of $35.7mW$; the total power loss of the full-bridge converter is about $4.05mW$ and the overall efficiency of the full-bridge converter is calculated to be $\eta = 88.7\%$.

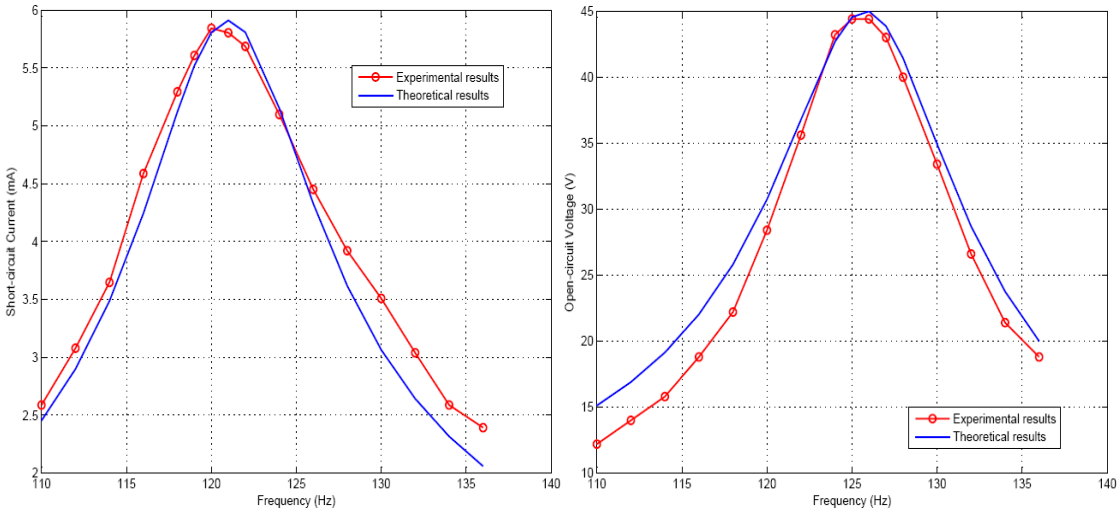

Figure 6.4. Comparison of experimental and theoretical results of: (a) short-circuit current, (b) open-circuit voltage

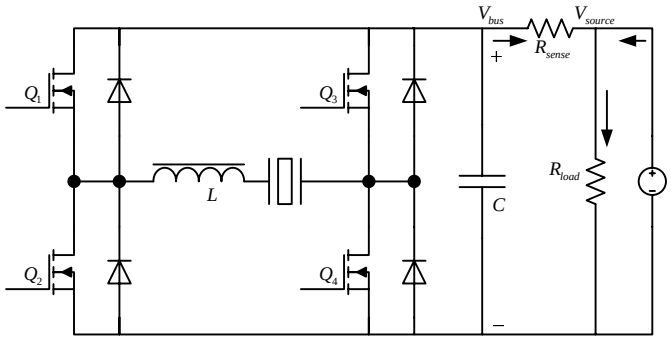

Figure 6.5. Full-bridge converter with resistive load

At the frequency of $124Hz$, the experimental waveforms of the piezoelectric device voltage and output current are shown in Fig. 6.7, and the voltage and current waveforms during voltage transition are highlighted in Fig. 6.8. The charging/discharging current is fairly smooth because of the PWM regulation, and this accounts for the high efficiency of the circuit.

The power loss associated with the full-bridge converter can be further calculated by equations (5.10) to (5.16) from the voltage and current waveforms in Fig. 6.7 and Fig. 6.8. During continuous conduction period, the conduction loss is calculated to be $0.44mW$, and the loss associated with the filter inductor, sense resistor and resistors in the voltage and current measuring differential amplifier is

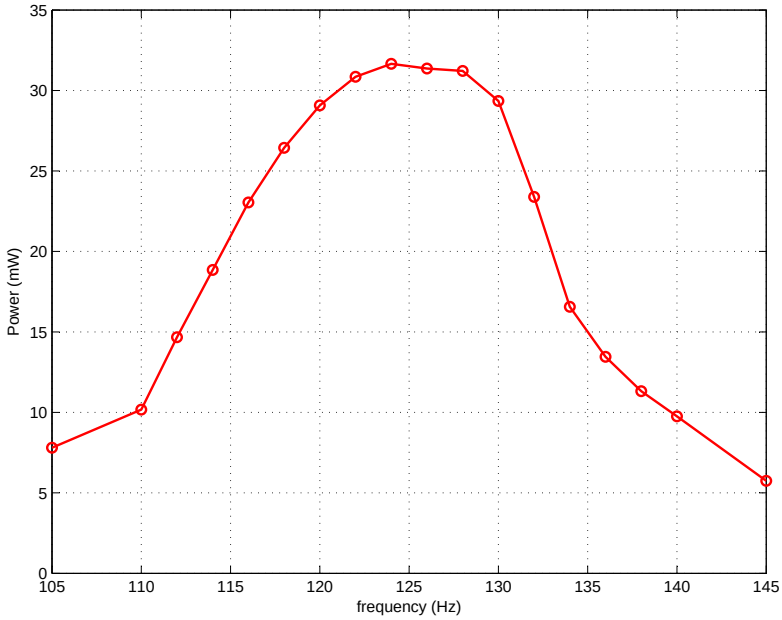

Figure 6.6. Maximum power harvested by active circuit with resistive load under different frequencies

calculated to be $1.91mW$. During voltage transition period, the conduction loss is calculated to be $0.70mW$, the switching loss is calculated to be $0.07mW$, and the loss associated with the filter inductor, sense resistor and resistors in the voltage and current measuring differential amplifier is calculated to be $0.38mW$. By adding all these power losses together, the total power consumption associated with the power electronic circuit is about $3.5mW$. Since the total power consumption is $4.05mW$, the power loss associated with the discharging process is estimated to be $0.55mW$.

The efficiency of the circuit can be calculated by (5.17), (5.18) and (5.20). During the continuous conduction period, the power consumption is about $2.35mW$ and the circuit efficiency is calculated as 93.1%; while during the voltage transition period, the power consumption is about $1.7mW$ and the circuit efficiency during voltage transition is about 87.0%.

Simulations based on piecewise-constant control voltage are also performed to compare with the experimental results. The simulation results of the maximum harvested power for different circuit efficiencies are plotted and compared with

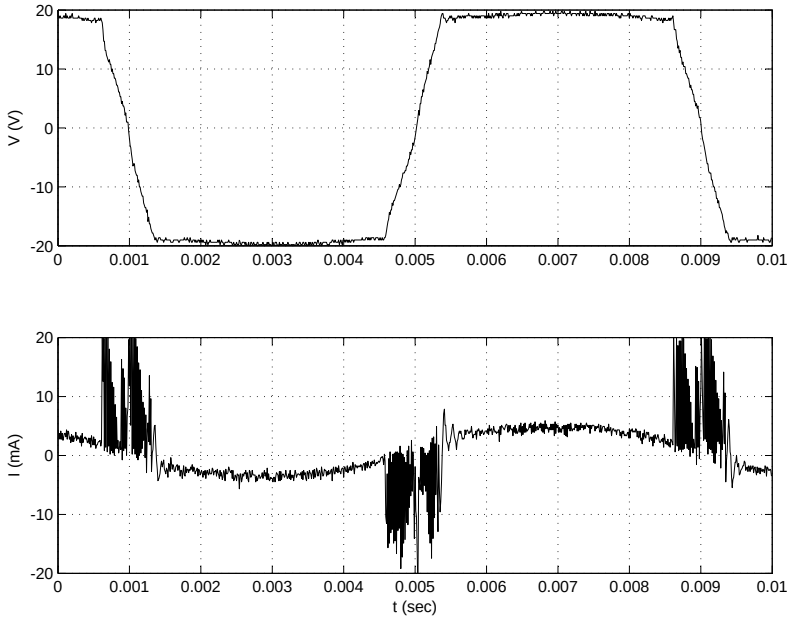

Figure 6.7. Waveforms of piezoelectric device voltage and output current

the experimental data in Fig. 6.9. The optimal voltage magnitude and phase angle are also simulated and compared with the experimental values, as shown in Figs. 6.10 (a) and 6.10 (b), respectively. The experimental results are close to the simulation results of higher efficiencies at near-resonance frequencies, and are close to the simulation results of lower efficiencies at off-resonance frequencies, which indicates that the circuit efficiency will drop with the frequency deviating away from the resonance. The circuit efficiency will be lower at off-resonance frequencies because, the optimal voltage magnitude will be higher at those frequencies, and so the switching loss and other losses will be larger. The experimental results generally match the simulation results, which indicates the validity of the proposed active energy harvesting theory.

For comparison, we also performed an experiment for a standard passive AC-DC diode-bridge rectifier circuit with a tunable resistive load, as shown in Fig. 6.11. The diode bridge is constructed by Schottky diodes to minimize power consumption. At each frequency, we tuned the resistance value to find the maximum power, and the power can be calculated by $P_{harvested} = \frac{V_{bus}^2}{R_{load}}$. The theoretical maximum power harvested by the diode-bridge rectifier circuit and optimal load

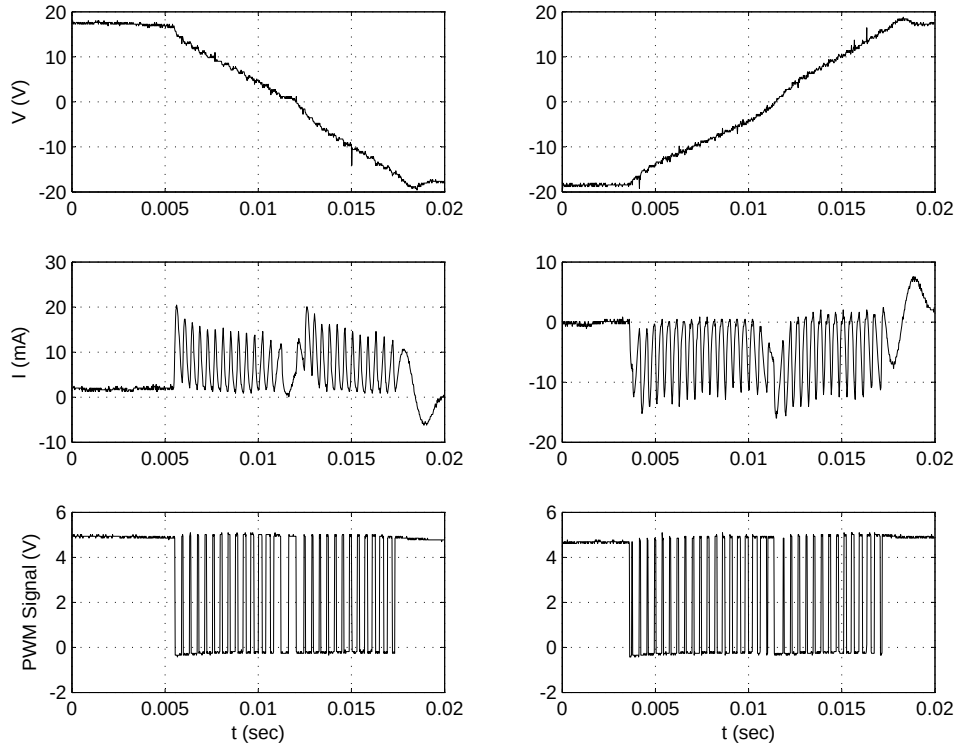

Figure 6.8. Waveforms of piezoelectric device voltage and output current during voltage transition, from left top clock-wise: voltage during positive transition, voltage during negative transition, current during negative transition, PWM signal to $Q4$ during negative transition, PWM signal to $Q2$ during positive transition and current during positive transition

resistance can also be obtained by (3.6), and the results are compared with the experimental results in Figs. 6.12 (a) and 6.12 (b), respectively. A very good agreement of the experimental results with the simulation results can be seen.

The power harvesting ability of the active circuit and passive circuit is then compared by the ratio of the power harvested by the active circuit with resistive load to that harvested by the passive circuit with resistive load, as shown in Fig. 6.13. Because the investigated piezoelectric dynamic system is a relatively strongly-coupled system, the maximum harvested power obtained by the active technique is only about 25% larger than that obtained by the passive technique. However, at off-resonance frequencies, the power harvested by the active technique is as much as 5 times larger. Hence the active technique shows the wide-bandwidth

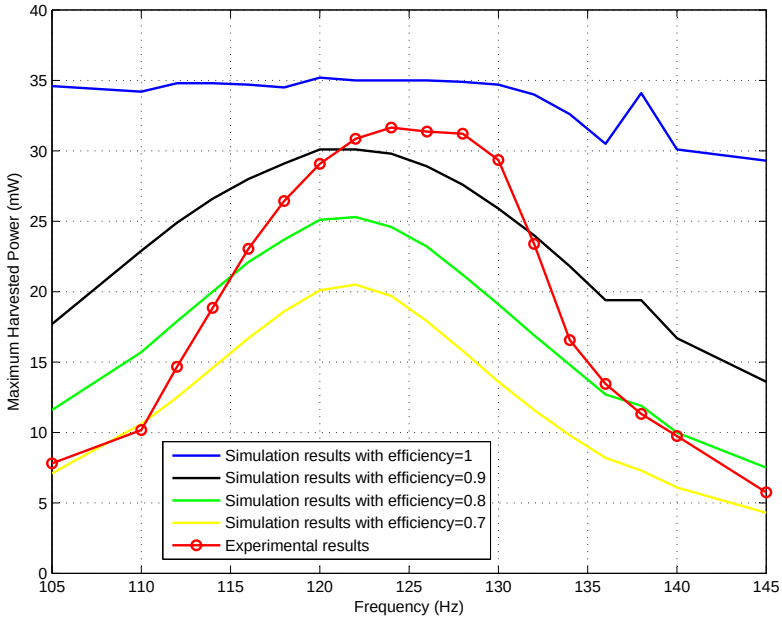

Figure 6.9. Comparison of experimental and simulation results of maximum harvested power for active circuit with resistive load

advantage over the passive technique. In practical implementation, it is often difficult to maintain the system operating at the resonance frequency, and so the active technique is more suitable for these applications.

6.3 Full-bridge with Flyback Converter

In practical applications the harvested power should not be dissipated in a resistor, and so the next experiment is using the active energy harvesting circuit to charge a battery through a flyback converter. The experimental circuit is shown in Fig. 6.14. The battery is a Li-ion rechargeable battery ($ER - C520$ by $Energizer$) with the voltage of $V_{bat} = 7.7V$. An $R_{sense} = 100\Omega$ sense resistor is placed in series with the battery to sense the current flowing into the battery, and so the power obtained by the battery can be calculated by

$$P_{harvested} = V_{bat}\frac{V_{DC} - V_{bat}}{R_{sense}}. \tag{6.2}$$

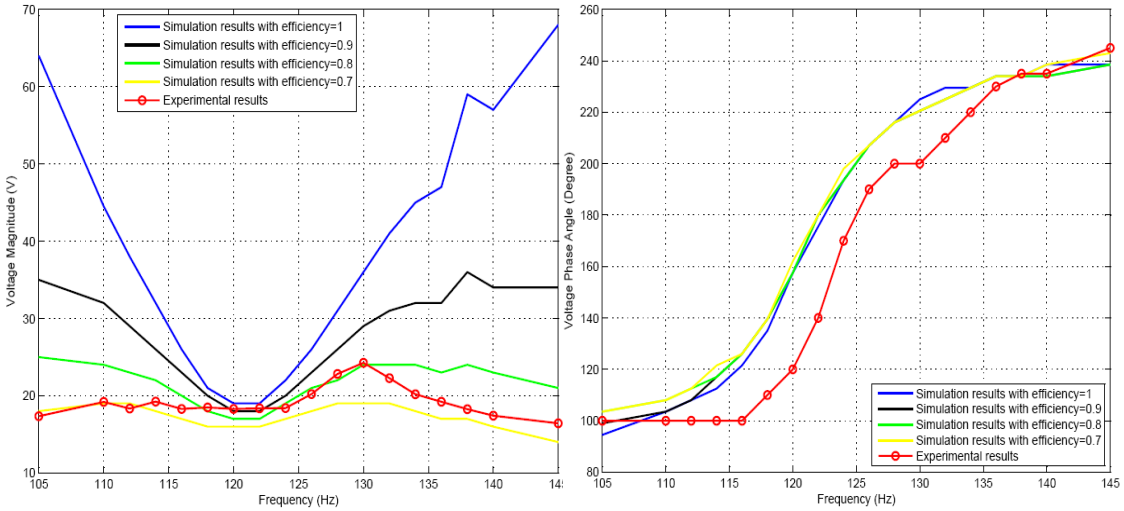

Figure 6.10. Comparison of experimental and simulation results of optimal control voltage for active circuit with resistive load: (a) voltage magnitude, (b) voltage phase angle

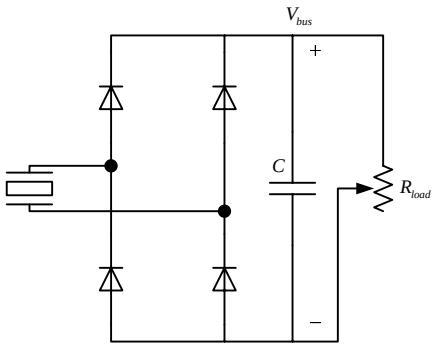

Figure 6.11. AC-DC diode-bridge rectifier with resistive load

In the experiment the duty cycle of MOSFET T and the phase angle were manually tuned to find the maximum power at each frequency. The result is plotted and compared with the maximum power harvested by the active circuit with a resistive load, as shown in Fig. 6.15. The power obtained by the battery is lower than the maximum power that can be harvested by the active circuit because of the flyback converter. The maximum power to the battery is $27.13mW$ also at $124Hz$, and the efficiency of the flyback converter is then evaluated to be approximately 85.7%.

A passive AC-DC diode-bridge rectifier circuit with a flyback converter was also built for comparison, as shown in Fig. 6.16. Again a 100Ω sense resistor is inserted

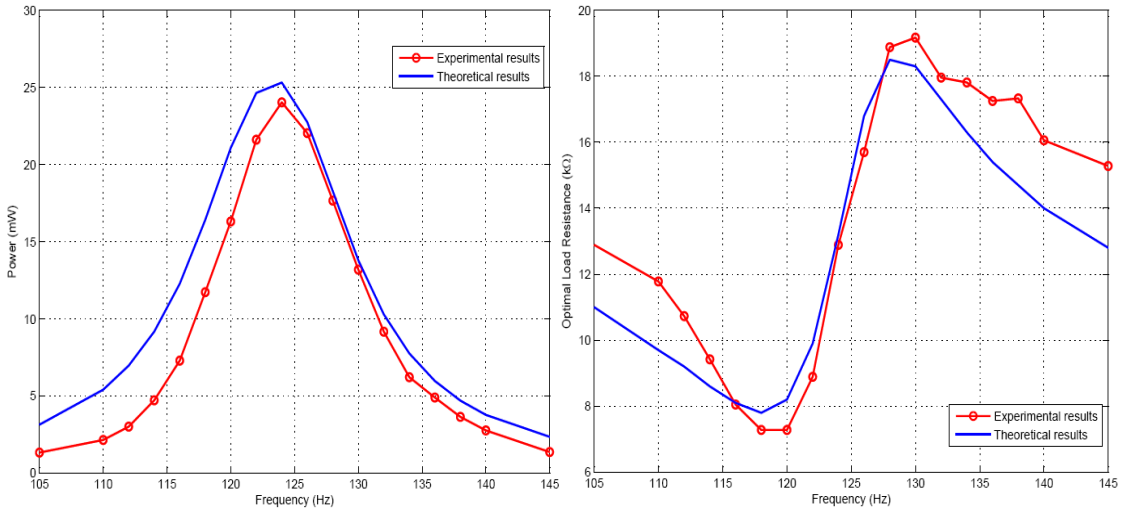

Figure 6.12. Comparison of experimental and theoretical results for passive AC-DC rectifier with resistive load: (a) maximum harvested power, (b) optimal load resistance

to measure the output current, and the maximum power is also measured by (6.2). In the experiment the duty cycle of MOSFET T was varied to find the maximum power harvesting at each frequency. The result is compared with the maximum power harvested by the diode-bridge rectifier circuit with resistive load in Fig. 6.17, and also compared with the maximum harvested power of the active circuit with a flyback converter by the ratio of harvested power in Fig. 6.18. The result in Fig. 6.18 is similar to that in Fig. 6.13. Again, the active energy harvesting technique shows advantage over the passive technique in wide-bandwidth for a piezoelectric dynamic system.

6.4 Adaptive Technique Implementation

As mentioned in Chapter 4, an appropriate control scheme must be implemented to adaptively find the optimal operating point for the active energy harvesting technique because of the effect of circuit efficiency on the energy harvesting, and the parameter changes due to the environmental changes in practical implementation.

We first implement the two-dimensional quadratic interpolation algorithm in dSPACE 1104 system. The dSPACE controller board is designed to meet the requirements of modern function prototyping. It provides 4 A/D channels, 8 D/A

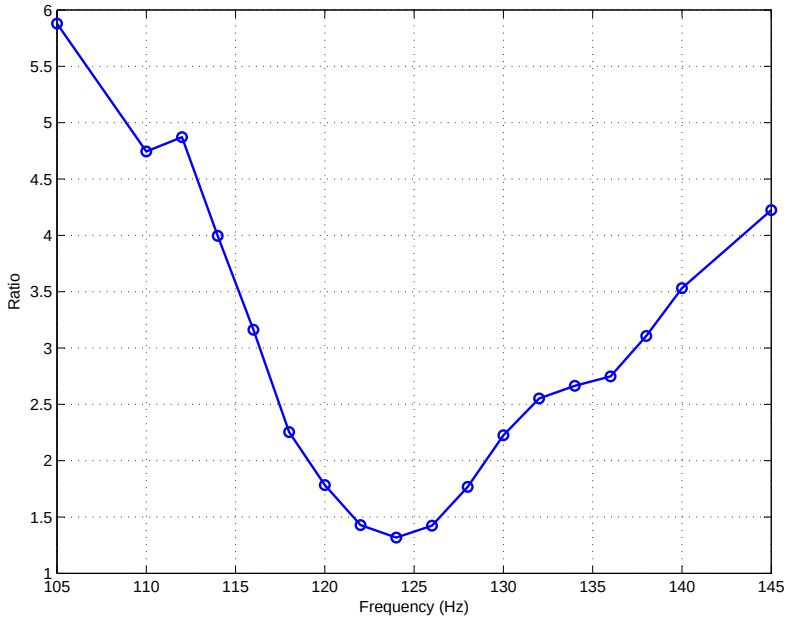

Figure 6.13. Ratio of the power harvested by active circuit with resistive load to passive circuit with resistive load

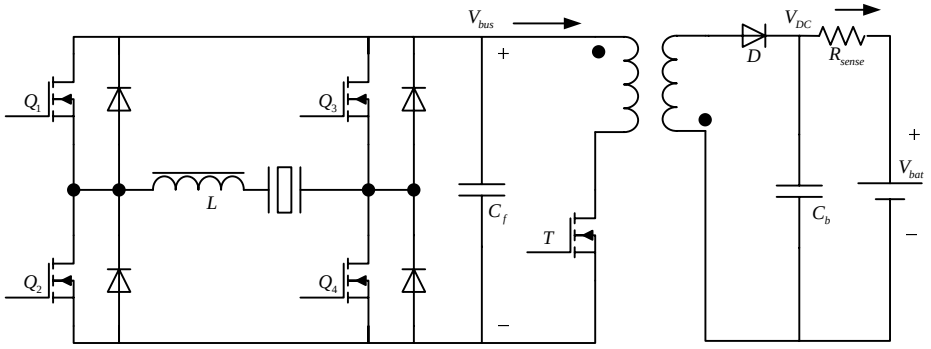

Figure 6.14. Full-bridge converter with flyback converter

channels, and PWM generation block. The adaptive controller was written in MATLAB Simulink, and the dSPACE 1104 board interfaces the controller with the power electronic circuit, transferring measured signals (output voltage, output current. etc.) to the controller through the A/D channels and sending drive signals and PWM signals to the full-bridge converter and flyback controller, respectively, through the D/A channels.

For this adaptive algorithm, we need to give an initial operating point first,

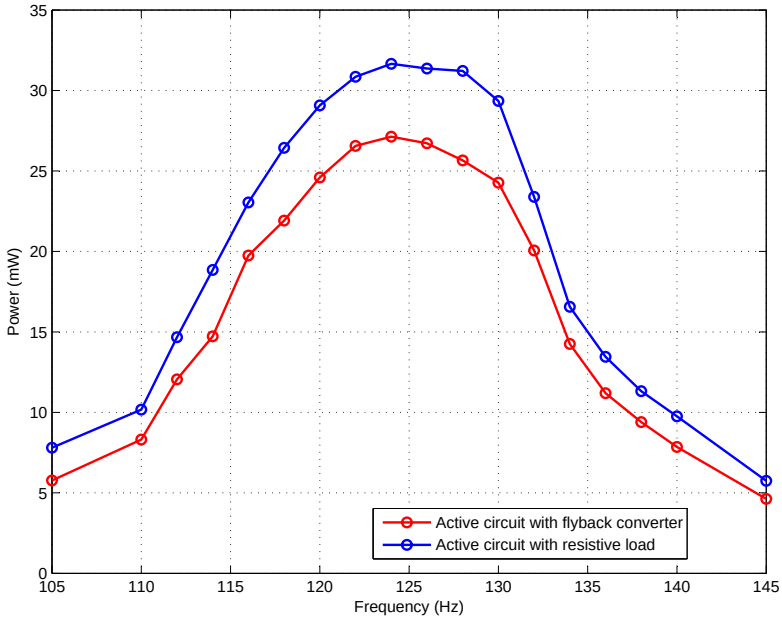

Figure 6.15. Comparison of power harvested by active circuit with flyback converter and resistive load

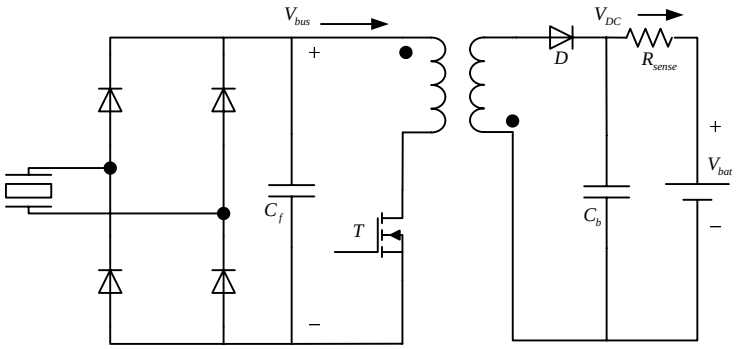

Figure 6.16. AC-DC rectifier with flyback converter

and then perturb the initial point to 4 other operating points around the initial point, and record the output power for each initial point, and finally we need to perform quadratic interpolation for the five operating points and find the next operating point in the gradient direction. Since the adaptive control algorithm needs to be implemented in real-time, and the controller board is continuously calling the Simulink model, we can not use arrays to store the power values, nor can we run a "for loop" to determine the operating points, as we usually do in the

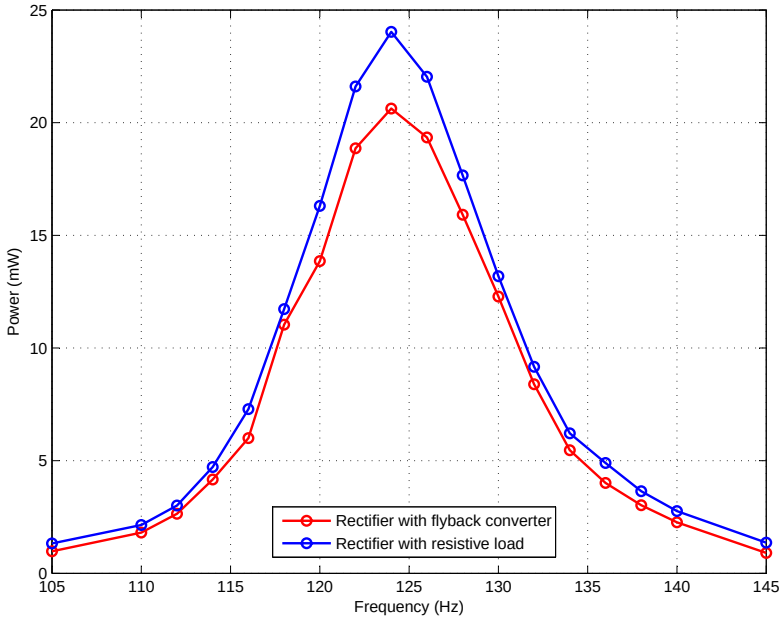

Figure 6.17. Comparison of power harvested by AC-DC rectifier with flyback converter and resistive load

m-file program. Instead, we need to use a sample/hold block to store the data, and use a counter to set the time sequence for giving each operating point, and also for performing the quadratic interpolation algorithm. The block diagram is shown in Fig. 6.19.

In the model, when the counter equals 0 to 4, we apply five different operating points to the actual circuit through the PWM block. *Phase* is used to generate the main drive signal for the full-bridge converter, and *Duty* is used to generate the PWM for the flyback converter. The harvested power is fed into several sample/hold blocks. At the falling edge of the trigger signals, the power values will be sampled and held. Rate transition blocks are needed between the input/output analog signal and the input/output of the sample/hold blocks, which will cause a unit delay of the input power value, and so at the end of counter state 1, the actual harvested power under the operating point given at counter state 0 will be recorded. So an additional state 5 is added to record the last power value. Then at counter state 6, we perform the quadratic interpolation algorithm to find the next operating point. The program is written in the embedded MATLAB function

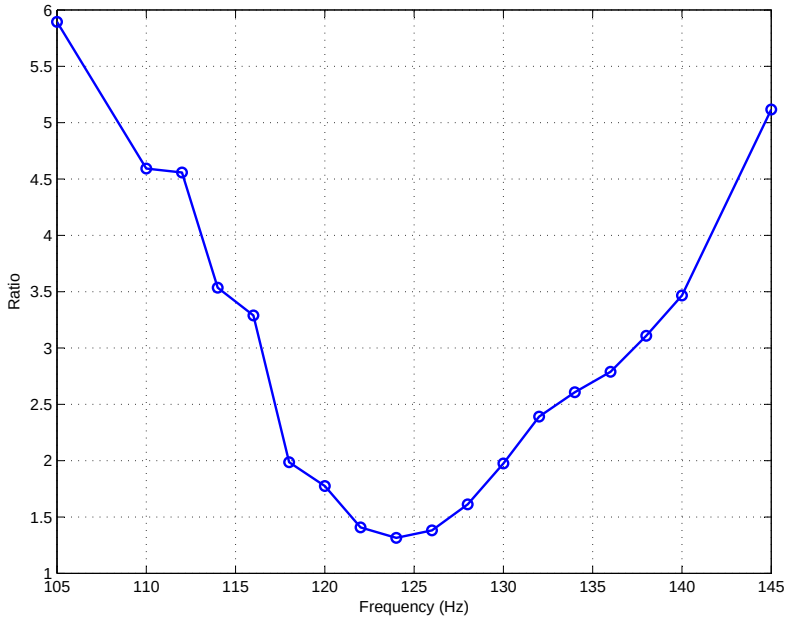

Figure 6.18. Ratio of the power harvested by active circuit with flyback converter to passive circuit with flyback converter

block named "Adaptive" in the model, and the code can be found in Appendix A.4.

Experiments were performed to verify the adaptive model. The piezoelectric system was excited at a frequency of $120Hz$ starting from an initial duty cycle of 4% and phase angle of 180°. The duty cycle, phase angle, full-bridge bus voltage and harvested power in the following steps are listed in Table. 6.1. After 8 steps, the operating point was getting very close to the optimal voltage magnitude and phase angle, and the harvested power was almost maximized. After these steps, the adaptive algorithm was still running, which caused a small oscillation of the operating point and harvested power.

While the dSPACE system based adaptive algorithm gives us very good results, the power consumption of the dSPACE controller board is a big consideration, and so we want to implement the adaptive control algorithm on a microcontroller whose power consumption can be extremely low. However, since the quadratic interpolation algorithm needs complex calculation, the low power microcontrollers are often not fast enough to implement it, and so we hereby apply the "two-

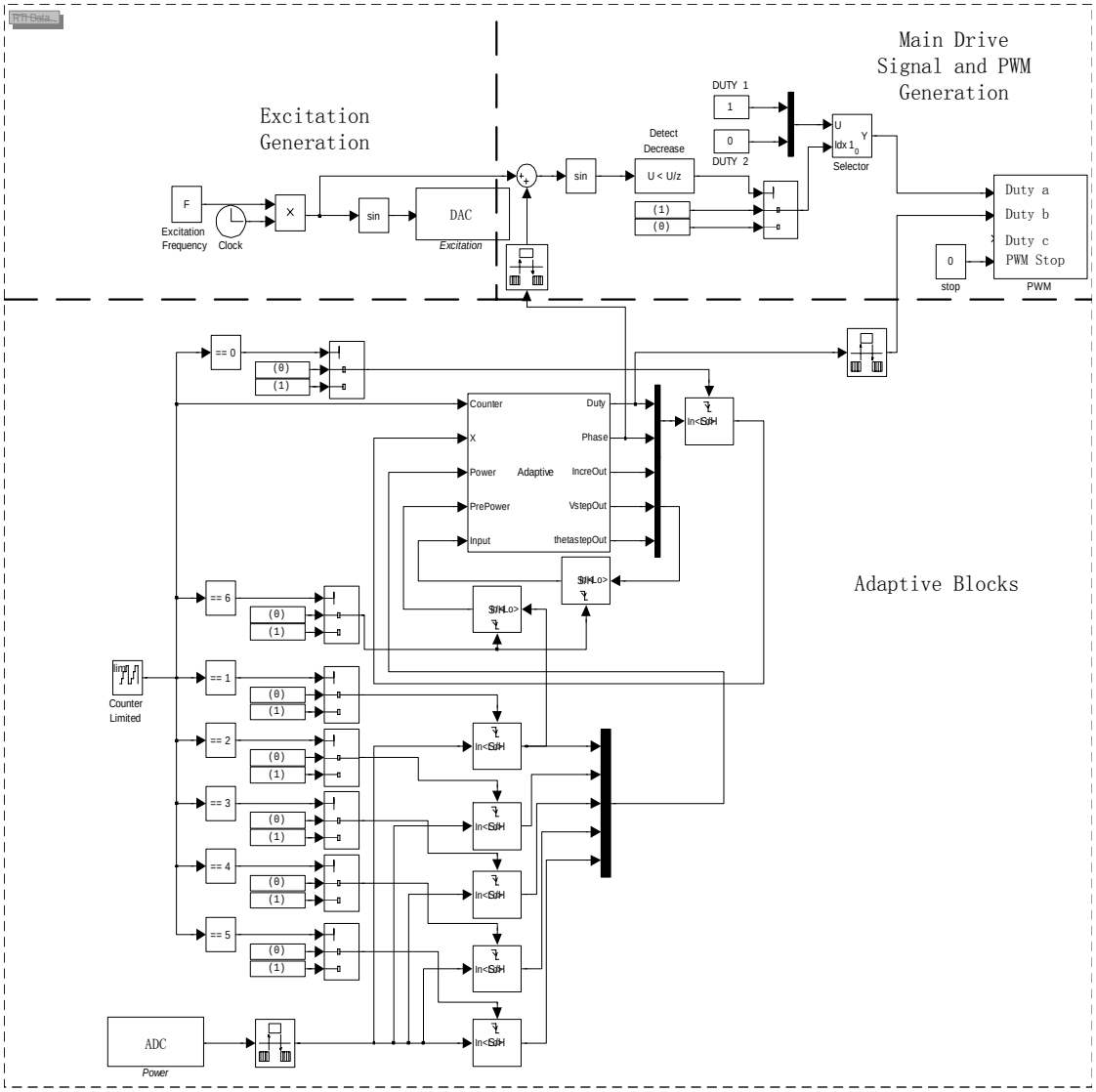

Figure 6.19. Simulink model for adaptive algorithm implemented on dSPACE

step" method, and the flow chart is shown in Fig. 6.20. In the flow chart, *Duty* represents the duty cycle of the PWM to the MOSFET of the flyback converter, *Phase* represents the phase angle of the control voltage, and *Power* represents the harvested power. Basically, we give an initial operating point, and then change one condition (duty cycle or phase angle). The power for these two operating points are then compared, and determine which direction the condition should go. Then we change to the other condition and perform the related comparison. This algorithm is not as fast as the quadratic interpolation algorithm, because the operating point

Table 6.1. Typical experimental results of adaptive control based on dSPACE 1104 system

$DutyCycle(\%)$	$PhaseAngle(degree)$	$BusVoltage(V)$	$Power(mW)$
4	180	7.08	9.14
3.88	168	8.18	11.53
3.38	143	10.05	16.36
3.20	136	13.18	19.95
2.81	132	15.86	21.76
2.34	120	19.81	23.41
2.10	116	21.8	22.58
2.40	115	18.5	23.41

is not moving along the steepest gradient direction, but it is simple to implement on a low-power microcontroller.

$ATmega48$ by $Atmel$ was chosen as the microcontroller for our application for its high performance and low power consumption ($250\mu A$ active current at $1.8V$ and $1MHz$ clock frequency) This 8-bit microcontroller features six PWM channels with programmable resolution from 2 to 16 Bits8-channels 10-bit Analog to Digital Converter (ADC), master/slave Serial Peripheral Interface (SPI), internal calibrated oscillator and 256 bytes of data EEPROM memory, and is good enough for our application. In the experiment, the PWM signal to the MOSFET of the flyback converter was directly generated from the microcontroller, and so $5V$ supply voltage was used for the microcontroller. A 8-bit digital data was transferred from the microcontroller to the DAC IC ($AD5300$) through the SPI to generate the desired analog voltage, which was then used as the reference signal to generate the main square-wave drive signal for the full-bridge converter with desired phase angle. The harvested power was fed into the microcontroller through the ADC of the microcontroller and converted into a digital value. The digital value of harvested power was then written and saved into the EEPROM data memory.

In the implementation, we had a counter running from 0 to 255 as the main time sequence. The counter frequency was set to $14.3Hz$, and so it takes about $18s$ to run one period. The internal clock frequency of the microcontroller is $8MHz$, and the PWM signal was set to 10-bit resolution, and so the switching frequency was $8kHz$. The program was written in C language and can be found in Appendix B. In the experiment, depending on the initial operating point, it takes

several minutes to get the optimal operating point. A typical experimental result is shown in Table. 6.2. The excitation frequency was $120Hz$, and the initial values were 4% duty cycle and 112° phase angle. The optimal operating point can be reached after 9 steps, which takes about 3 minutes.

Table 6.2. Typical experimental results of adaptive control based on *Atmega*48 Microcontroller

$PhaseAngle(degree)$	$BusVoltage(V)$	$Power(mW)$
111.7	5.3	7.40
114.6	6.2	8.42
117.5	7.5	11.20
120.0	8.2	13.84
122.9	10.7	16.67
125.8	12.1	19.77
128.6	13.5	21.99
131.2	16.6	25.05
128.6	19.4	25.55

Since the supply voltage was $5V$ and the microcontoller was running at $8MHz$ frequency, the actual power consumption of the microcontroller was measured to be $50mW$, still too much for our application. To realize a low power operation, the supply voltage and frequency must be reduced, but in this case the PWM signal generated by the microcontroller can not be directly used to drive the MOSFET, and so an extra PWM generation circuit with duty-cycle controlled by the microcontroller needs to be developed in the future.

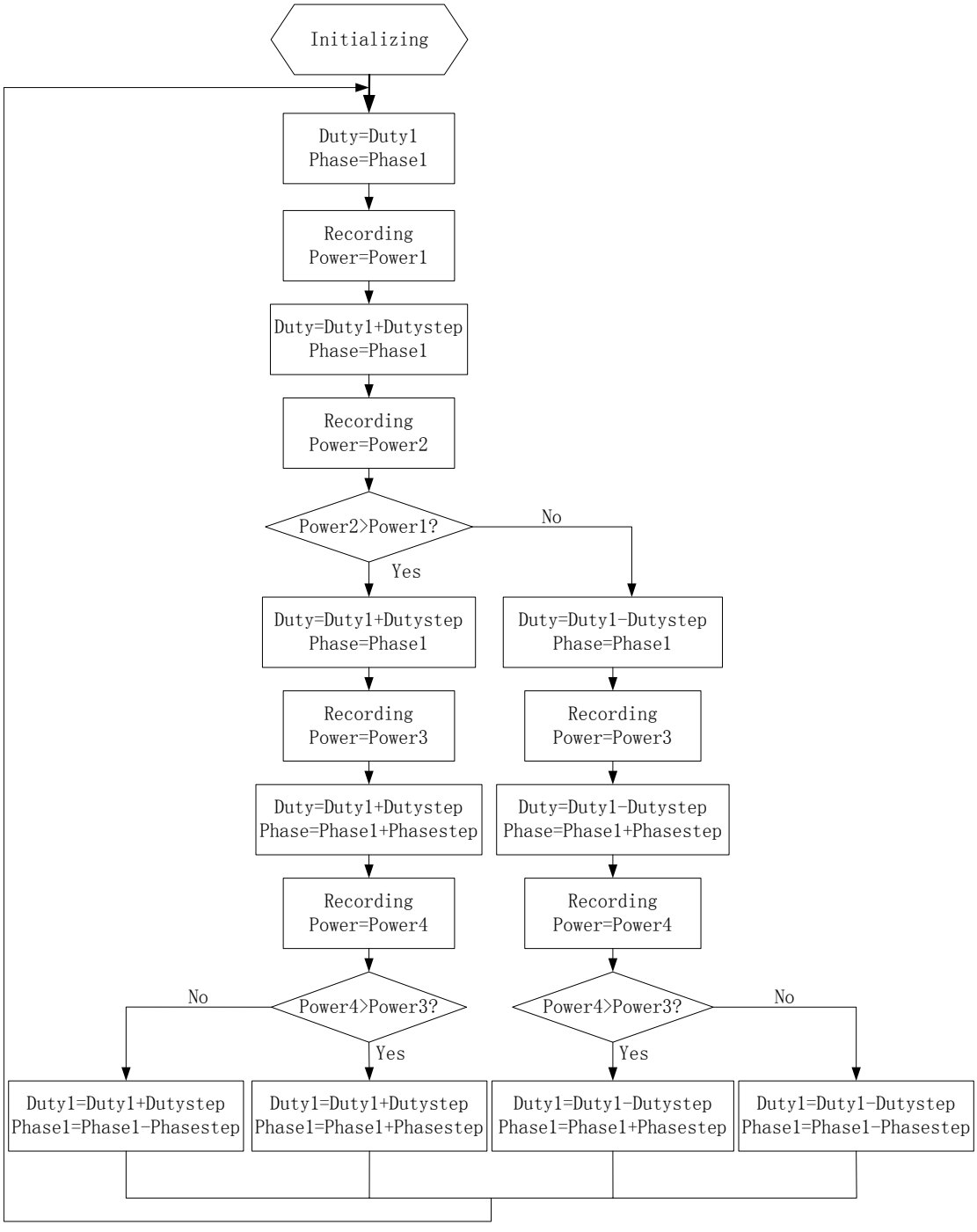

Figure 6.20. Flow chart of the adaptive algorithm implemented on microcontroller

Chapter 7

Conclusions and Future Work

7.1 Conclusions

In this dissertation, the model for a piezoelectric dynamic system is proposed and analyzed, an active energy harvesting technique is proposed for the system, the circuit to implement the active energy harvesting is developed, and experimental data is shown to verify the proposed theory.

The piezoelectric dynamic system can be modeled as a spring-mass-damper system. The electromechanical system can also be modeled as an electric circuit by using a transformer to represent the piezoelectric effect. The equivalent mechanical and electrical impedance was derived, and maximum power is harvested when the load impedance matches the internal impedance of the system. The parameters of the system were derived from the short-circuit and open-circuit tests.

The active energy harvesting technique was derived for a piezoelectric dynamic system under an external excitation force with constant magnitude. By applying an optimal control voltage to the piezoelectric device, the equivalent load impedance can always match the internal impedance of the system, and the maximum power can always be harvested for all frequencies. The simulation results have verified the derived optimal control voltage, and have shown that the active technique has significant advantage over the passive and semi-active techniques, especially at off-resonance frequencies.

The optimal control voltage is affected by the actual circuit efficiency and parameter deviations. Adaptive control algorithms were developed to adaptively

find the optimal control voltage for a piezoelectric dynamic system with the knowledge of excitation force and harvested power. By performing the two-dimensional quadratic interpolation to the power function, the optimal control voltage can be quickly reached from an initial point.

A full-bridge converter was developed to apply a piecewise-constant square-wave control voltage to the piezoelectric device, and to realize bidirectional power flow. A flyback converter was also applied following the full-bridge converter to charge a battery. Supporting circuitry was developed to insert dead-time to the full-bridge, regulate charging/discharging current, sense voltage and current, generate drive signals and so on. A completely stand-alone PCB board was built to implement all the power electronic interface and control circuitry.

Short-circuit and open-circuit tests were performed to identify the parameters of the system. The power harvested by the full-bridge converter with a resistive load was compared with the theory. It shows that the experimental results agree with the theoretical values very well, and the overall circuit efficiency is about 90%. The results of the active circuit were also compared with a passive AC-DC diode-bridge rectifier circuit with resistive load, and the power harvested by the active technique can achieve up to 5 times more than that of the passive technique at off-resonance frequencies. The full-bridge converter was then used to charge a battery through a flyback converter, and compared with a diode-bridge rectifier followed by a flyback converter. The results also show that the power obtained by the battery through the active technique is much more than that obtained through the passive technique.

Adaptive control algorithms were implemented in both a dSPACE 1104 controller board and an $ATmega48$ microcontroller. A Simulink model was built to implement the two-dimensional quadratic interpolation algorithm in dSPACE, and the experimental results show that the optimal control voltage can be quickly reached from an initial operation point. A simpler "two-step" adaptive algorithm was implemented on the microcontroller. It took a longer time to reach the optimal control voltage from the same initial point, but the power consumption of the microcontroller is much lower.

7.2 Future Work

The circuit efficiency, especially the efficiency during voltage transition significantly affects the power harvesting ability of the active circuit. Although the overall efficiency of the power electronic circuit is above 90%, the efficiency during voltage transition is only around 75%, and so further control need to be implemented to improve this efficiency.

The control circuitry is still powered by external power supplies. By applying a high-efficiency DC-DC converter to the battery, it is possible to generate the power for the control circuitry directly from the battery and remove the need of external power supplies. To realize this the power consumption of the control circuitry needs to be further reduced by better design and using low-power ICs. Particularly, the power consumption of the gate drive circuit needs to be significantly reduced, and a low power high-side gate drive circuit without using isolated power supplies needs to be developed. Another way to simplify the high-side gate drive is to use the P-channel MOSFETs for high-side switches. By making the gate drive signal to the high-side P-MOSFETs the ground or the bus voltage, the MOSFETs will be turned on or off, respectively. A gate drive IC is still needed to provide the high drive signal, and the supply voltage of the gate driver should be the same as the bus voltage so that the MOSFETs can be securely turned-off when the drive signal is high. The control circuitry for generating high-side gate drive signals also needs to be changed accordingly. The constraint of this circuit is that the bus voltage can not be too high, so that the maximum supply voltage of the gate drive IC or the maximum gate to source voltage of the P-MOSFETs will not be exceeded. A prototype of the full-bridge converter with P-channel MOSFETs as the high-side switches was also built for testing. In the implementation, $ZVN3320$ was still used as the low-side N-channel MOSFET, and P-channel MOSFETs $ZVP3310$ by $ZETEX$ were used as the high-side switches. $IRS2001$ by $International\ Rectifiers$ was chosen as the gate driver for its low power consumption ($150\mu A$ quiescent current). In our application, the optimal voltage magnitude is about $18V$ near resonance frequencies, lower than the maximum supply voltage of $IRS2001$ ($20V$) and the maximum gate-to-source voltage of $ZVP3310$ ($20V$), so the circuit worked fine and the performance was almost the same as the N-channel

MOSFETs based full-bridge converter. However, the circuit is not applicable to cases where the optimal voltage magnitude is larger than $20V$. The total power consumption of the circuit was measured to be $3.3mW$, much lower than the isolated power supply based high-side N-channel MOSFET gate drive circuit. Also the power consumption of the op-amps and the microcontroller needs to be further reduced to a much lower level. It is believed that with the improvement of piezoelectric materials and the active energy harvesting circuit, the active energy harvesting technique will be widely used in all kinds of applications, especially wide-bandwidth applications, in the near future.

Appendix A

MATLAB Code for Simulation and dSPACE System

A.1 Phasor Simulation

MATLAB code in m-file for performing phasor analysis on the piezoelectric dynamic system.

```
clear;
m=0.007; %end mass
Fm=0.364; %equivalent excitation force
C=0.18e-6; %piezoelectric capacitance under constant force
k=4046; %stiffness
d=1.86e-6; %piezoelectric constant
Cp=0.166e-6; %piezoelectric capacitance under fixed displacement
b=0.4635; %damping coefficient
n=0;
nw=0;
xs=0.01;
x=0:xs:2*pi-xs;
eff=1; %circuit efficiency
%find optimal voltage magnitude and phase angle for different frequencies
for w=2*pi*[105 110:2:140 145];
```

```
nw=nw+1;
n=0;
for Vm=5:1:105
    for theta=0.1:0.01:2*pi
        n=n+1;
        Fph=Fm;
        Vph(n)=Vm*cos(theta)+j*Vm*sin(theta);
        deltaph(n)=(Fph+k*d*Vph(n))/(k-w^2*m+j*w*b);
        vph(n)=j*w*deltaph(n);
        Iph(n)=-Cp*j*w*Vph(n)-k*d*vph(n);
        V=Vm*cos(x+theta);
        v=abs(vph(n))*cos(x+angle(vph(n)));
        I=abs(Iph(n))*cos(x+angle(Iph(n)));
        W=V.*I*xs;
        for ni=1:length(x)
            if W(ni)>=0
                W(ni)=W(ni)*eff;
            else
                W(ni)=W(ni)/eff;
            end
        end
        P(n)=sum(W)/(2*pi);
    end
end
Pmax(nw)=max(P); %maximum power
nn=find(P==max(P));
Vopt(nw)=Vph(nn); %optimal sinusoidal voltage
VoptBipolar(nw)=abs(Vph(nn))/(4/pi); %optimal voltage magnitude
%optimal phase angle
angleVopt(nw)=-angle(Vopt(nw))*180/pi;
if angleVopt(nw)<0
    angleVopt(nw)=angleVopt(nw)+360;
end
```

```
end

f=[105 110:2:140 145];
w=2*pi*f;
Ptheo=Fm^2/(8*b)*ones(1,length(f)); %theoretical maximum power
Vtheo=(-w*b-j*(k-w.^2*m))./(2*k*d*w*b)*Fm; %theoretical optimal control voltage
magVtheo=abs(Vtheo/4*pi); %theoretical voltage magnitude
%theoretical voltage phase angle
angleVtheo=-angle(Vtheo)*180/pi;
for n=1:length(f)
   if angleVtheo(n)<0
       angleVtheo(n)=angleVtheo(n)+360;
   end
end
```

A.2 Quadratic Interpolation Algorithm

MATLAB code in m-file for performing the quadratic interpolation algorithm on the piezoelectric dynamic system.

```
clear;
eff=1; %circuit efficiency.
w=2*pi*121; %excitation frequency
X1=[5;2*pi/3]; %Initial operating point
Vstep=0.5; %change step of voltage magnitude
thetastep=pi/2/100; %change step of voltage phase angle
P1(1)=0;
%Quadratic Interpolation Algorithm
for nn=1:10000
   X=[X1(1)-Vstep X1(1)-Vstep X1(1)+Vstep X1(1)+Vstep X1(1);
      X1(2)-thetastep X1(2)+thetastep X1(2)-thetastep X1(2)+thetastep X1(2)];
   Xmat(:,nn)=X1;
   for n=1:5
       Xn=X(:,n);
```

```
        P(n)=-harmonic(Xn(1),Xn(2),eff, w);
    end
    Q=[1/2*X(1,1)^2 X(1,1)*X(2,1) 1/2*X(2,1)^2 X(1,1) X(2,1);
       1/2*X(1,2)^2 X(1,2)*X(2,2) 1/2*X(2,2)^2 X(1,2) X(2,2);
       1/2*X(1,3)^2 X(1,3)*X(2,3) 1/2*X(2,3)^2 X(1,3) X(2,3);
       1/2*X(1,4)^2 X(1,4)*X(2,4) 1/2*X(2,4)^2 X(1,4) X(2,4);
       1/2*X(1,5)^2 X(1,5)*X(2,5) 1/2*X(2,5)^2 X(1,5) X(2,5)];
    Par=Q\P';
    Ax=[Par(1) Par(2);
       Par(2) Par(3)];
    bx=[Par(4);Par(5)];
    Xgrad=Ax*X(:,5)+bx; %gradient direction
    P1(nn+1)=P(5);
    if abs(P1(nn+1)-P1(nn))<=1e-6
        Pmax=-P1(nn+1);
        niter=nn+1;
        break;
    end
    Gamma=[400 0;0 8]; %gain
    X1=X1-Gamma*Xgrad; %new operating point
end

%function "harmonic", also be used in the next section.
function P=harmonic(Vm, phase, eff, w)
m=0.007; %end mass
Fm=0.364; %equivalent excitation force
C=0.18e-6; %piezoelectric capacitance under constant force
k=4046; %stiffness
d=1.86e-6; %piezoelectric constant
Cp=0.166e-6; %piezoelectric capacitance under fixed displacement
b=0.4635; %damping coefficient
n=0;
nw=0;
```

```
xs=0.01;
x=0:xs:2*pi-xs;

Fph=Fm;
Vph=Vm*cos(phase)+j*Vm*sin(phase);
deltaph=(Fph+k*d*Vph)/(k-w^2*m+j*w*b);
vph=j*w*deltaph;
Iph=-Cp*j*w*Vph-k*d*vph;
V=Vm*cos(x+phase);
v=abs(vph)*cos(x+angle(vph));
I=abs(Iph)*cos(x+angle(Iph));
W=V.*I*xs;
for ni=1:length(x)
   if W(ni)>=0
      W(ni)=W(ni)*eff;
   else
      W(ni)=W(ni)/eff;
   end
end
P=sum(W)/(2*pi);
```

A.3 "Two-step" Algorithm

MATLAB code in m-file for performing the "two-step" algorithm on the piezoelectric dynamic system.

```
clear;
eff=1; %circuit efficiency
V0=5; %initial voltage magnitude
phase0=2*pi/3; %initial phase angle
Vstep=1; %voltage magnitude incremental
phasestep=pi/180; %phase angle incremental
Vm=V0;
phase=phase0;
```

```
N=2000;
w=2*pi*121; %excitation frequency
Pini(1)=0;
for n=1:1:N
   Vvec(n)=Vm;
   phasevec(n)=phase;
   P1=harmonic(Vm,phase,eff,w);
   Pvec(n)=P1;
   Pini(n+1)=P1;
   if abs(Pini(n+1)-Pini(n))<1e-5
       break;
   end
   P2=harmonic(Vm+Vstep,phase,eff,w);
   if abs(P2-P1)<=1e-5;
       Vm=Vm;
   elseif P2>=P1;
       Vm=Vm+Vstep;
   else
       Vm=Vm-Vstep;
   end
   P3=harmonic(Vm,phase,eff,w);
   P4=harmonic(Vm,phase+phasestep,eff,w);
   if abs(P4-P3)<=1e-5;
       phase=phase;
   elseif P4>=P3;
       phase=phase+phasestep;
   else
       phase=phase-phasestep;
   end
end
```

A.4 Embedded Adaptive Function

MATLAB code for embedded function "Adaptive" to realize the quadratic interpolation method on dSPACE 1104 system.

```
function [Duty, Phase, IncreOut, VstepOut, thetastepOut] =
Adaptive(Counter, X, Power, PrePower, Input)
%initial condition
Duty=0;
Phase=0;
IncreOut=[0;0];
VstepOut=0;
thetastepOut=0;
%incremental and step of voltage magnitude and phase angle
IncreInV=Input(1);
IncreIntheta=Input(2);
Vstep=Input(3);
thetastep=Input(4);
%use counter to give operating points and perform quadratic interpolation
switch Counter
   case 0 %first operating point
       Duty=X(1)+IncreInV;
       Phase=X(2)+IncreIntheta;
   case 1 %second operating point
       Duty=X(1)-Vstep;
       Phase=X(2)-thetastep;
   case 2 %third operating point
       Duty=X(1)-Vstep;
       Phase=X(2)+thetastep;
   case 3 %fourth operating point
       Duty=X(1)+Vstep;
       Phase=X(2)-thetastep;
   case 4 %fifth operating point
       Duty=X(1)+Vstep;
```

```
    Phase=X(2)+thetastep;
case 5 %fifth operating point
    Duty=X(1)+Vstep;
    Phase=X(2)+thetastep;
case 6 %quadratic interpolation method
    Duty=X(1)+Vstep;
    Phase=X(2)+thetastep;
    if abs(Power(1)-PrePower)<=0.1
        IncreOut=[0;0];
        VstepOut=0;
        thetastepOut=0;
    elseif Vstep==0
        IncreOut=[5;10];
        VstepOut=1.5;
        thetastepOut=3;
    else
    Q=[1/2*X(1)^2 X(1)*X(2) 1/2*X(2)^2 X(1) X(2);
    1/2*(X(1)-Vstep)^2 (X(1)-Vstep)*(X(2)-thetastep)
    1/2*(X(2)-thetastep)^2 (X(1)-Vstep) (X(2)-thetastep);
    1/2*(X(1)-Vstep)^2 (X(1)-Vstep)*(X(2)+thetastep)
    1/2*(X(2)+thetastep)^2 (X(1)-Vstep) (X(2)+thetastep);
    1/2*(X(1)+Vstep)^2 (X(1)+Vstep)*(X(2)-thetastep)
    1/2*(X(2)-thetastep)^2 (X(1)+Vstep) (X(2)-thetastep);
    1/2*(X(1)+Vstep)^2 (X(1)+Vstep)*(X(2)+thetastep)
    1/2*(X(2)+thetastep)^2 (X(1)+Vstep) (X(2)+thetastep)];
    Par=Q\Power;
    Ax=[Par(1) Par(2);
        Par(2) Par(3)];
    bx=[Par(4);Par(5)];
    Xgrad=Ax*[X(1) X(2)]'+bx; %gradient direction
    if abs(Power(1)-PrePower)<=0.2
        Gamma=[5 0;0 70]; %gain
        IncreOut=-Gamma*Xgrad;
```

```
            VstepOut=0.5;
            thetastepOut=3;
        else
            Gamma=[15 0;0 70]; %gain
            IncreOut=-Gamma*Xgrad;
            VstepOut=1.5;
            thetastepOut=3;
        end
        end
end
```

Appendix B

C Code on Microcontroller

The C-code for implementing the "two-step" adaptive algorithm on $ATmega48$ microcontroller.

```
#include <avr/io.h>
#include "my_bit.h"

#define ADC_PRESCALE_MASK (BIT(ADPS2) | BIT(ADPS1)) // Prescale 8MHz
crystal to get ADC clock between 50-200kHz

#define ADC_NOT_DONE() (ADCSRA & BIT(ADSC)) // use ADSC to see the
finish of ADC
//Setup ADC
int setupADC(void){
  SET_BIT(ADMUX, BIT(REFS0); //Set reference to internal reference
  SET_BIT(ADMUX, BIT(REFS1));
  CLEAR_BIT(ADMUX, BIT(ADLAR)); //no left adjust of ADC data
  SET_BIT(ADMUX, BIT(MUX0)); //Enable ADC1
  // ADCSRA - ADC Control and Status Register A
  SET_BIT(ADCSRA, BIT(ADEN)); //Enable ADC
  CLEAR_BIT(ADCSRA, BIT(ADATE)); //Auto Trigger disable
  SET_BIT(ADCSRA, ADC_PRESCALE_MASK); //Set clock prescale
  SET_BIT(DIDR0, BIT(ADC1D));
  return 1;
```

```
}

void EEPROM_write(unsigned int uiAddress, unsigned char ucData) {
//Wait for completion of previous write
while(EECR & (1<<EEPE));
//Set up address and Data Registers
EEAR = uiAddress;
EEDR = ucData;
//Write logical one to EEMPE
EECR |= (1<<EEMPE);
//Start eeprom write by setting EEPE
EECR |=(1<<EEPE);
}

unsigned char EEPROM_read(unsigned int uiAddress) {
//Wait for completion of previous write
while(EECR & (1<<EEPE));
//Set up address registe
EEAR = uiAddress;
//Start eeprom read by writing EERE
EECR |= (1<<EERE);
//Return data from Data Register
return EEDR;
}

void SPI_MasterInit(void) {
//Set SS, MOSI and SCK output
DDRB = 0xff;
//Enable SPI, Master, set clock rate fck/16
SPCR = (1<<SPE)|(1<<MSTR)|(1<<SPR0)|(1<<CPOL);
}

void SPI_MasterTransmit(char cData1, char cData2) {
```

```
CLEAR_BIT(PORTB,BIT(PB0));
//Start transmission
SPDR = cData1;
//Wait for transmission complete
while(!(SPSR &(1<<SPIF)));
SPDR = cData2;
//Wait for transmission complete
while(!(SPSR & (1<<SPIF)));
SET_BIT(PORTB, BIT(PB0));
}

//main function
int main() {
 //external clock input, read
 DDRD=0x00;
 PORTD=0x00;
 //PWM output port, write
 DDRB=0xff;
 //ADC input port, read
 DDRC=0x00;
 PORTC=0x00;
 //externalclock,rising edge
 TCCR0A=0xa3;
 TCCR0B=0x07;
 //16 bit PWM setting
 TCCR1A=0xa2;
 TCCR1B=0x19;
 TCCR1C=0x00;
 //Top value
 ICR1H=0x03;
 ICR1L=0xff;
 //setting clock frequency to 8M
 CLKPR=0x80;
```

```
CLKPR=0x00;

SPI_MasterInit(); //SPI initialsetup
setupADC(); //ADC initialsetup

//intial setup
unsigned int Duty=40;
unsigned int Phase=180;
unsigned int PhaseNew=0;
unsigned int DutyNew=0;
unsigned int PhaseH;
unsigned int PhaseL;
unsigned int DutyStep=1;
unsigned int PhaseStep=4;
double b[5];

while(1) {
   switch (TCNT0){

   case 0:
   PhaseH=Phase/16;
   PhaseL=(Phase%16)<<4;
   SPI_MasterTransmit(PhaseH, PhaseL);
   OCR1AH=Duty/256;
   OCR1AL=Duty%256;
   break;

   case 60:
   SET_BIT(ADCSRA, BIT(ADSC));
   while(ADC_NOT_DONE());
   EEPROM_write(0x0000, ADC);
   EEPROM_write(0x0001, ADCH);
   break;
```

```
case 61:
OCR1AH=(Duty+DutyStep)/256;
OCR1AL=(Duty+DutyStep)%256;
break;

case 120:
SET_BIT(ADCSRA, BIT(ADSC));
while(ADC_NOT_DONE());
EEPROM_write(0x0002, ADC);
EEPROM_write(0x0003, ADCH);
break;

case 121:
b[0]=(EEPROM_read(0x0001)<<8)+EEPROM_read(0x0000);
b[1]=(EEPROM_read(0x0003)<<8)+EEPROM_read(0x0002);
if (b[1]-b[0]<=2 && b[0]-b[1]<=2)
    DutyNew=Duty;
else if (b[1]>b[0])
    DutyNew=Duty+DutyStep;
else
    DutyNew=Duty-DutyStep;
break;

case 122:
Duty=DutyNew;
OCR1AH=Duty/256;
OCR1AL=Duty%256;
break;

case 180:
SET_BIT(ADCSRA, BIT(ADSC));
while(ADC_NOT_DONE());
```

```
EEPROM_write(0x0004, ADC);
EEPROM_write(0x0005, ADCH);
break;

case 181:
PhaseH=(Phase+PhaseStep)/16;
PhaseL=((Phase+PhaseStep)%16)<<4;
SPI_MasterTransmit(PhaseH, PhaseL);
break;

case 240:
SET_BIT(ADCSRA, BIT(ADSC));
while(ADC_NOT_DONE());
EEPROM_write(0x0006, ADC);
EEPROM_write(0x0007, ADCH);
break;

case 241:
b[0]=(EEPROM_read(0x0005)<<8)+EEPROM_read(0x0004);
b[1]=(EEPROM_read(0x0007)<<8)+EEPROM_read(0x0006);
if (b[1]-b[0]<=2 && b[0]-b[1]<=2)
    PhaseNew=Phase;
else if (b[1]>b[0])
    PhaseNew=Phase+PhaseStep;
else
    PhaseNew=Phase-PhaseStep;
break;

case 242:
Phase=PhaseNew;
break;

default:
```

```
    break;
    };
 };
};
```

```
 //my_bit.h
 #ifndef __MY_BIT
 #define __MY_BIT

 #define SET_ALL  |= 0xFF;
 #define SET_BIT0 |= 0x01;
 #define SET_BIT1 |= 0x02;
 #define SET_BIT2 |= 0x04;
 #define SET_BIT3 |= 0x08;
 #define SET_BIT4 |= 0x10;
 #define SET_BIT5 |= 0x20;
 #define SET_BIT6 |= 0x40;
 #define SET_BIT7 |= 0x80;

 #define CLEAR_ALL  &= 0x00;
 #define CLEAR_BIT0 &= 0xFE;
 #define CLEAR_BIT1 &= 0xFD;
 #define CLEAR_BIT2 &= 0xFB;
 #define CLEAR_BIT3 &= 0xF7;
 #define CLEAR_BIT4 &= 0xEF;
 #define CLEAR_BIT5 &= 0xDF;
 #define CLEAR_BIT6 &= 0xBF;
 #define CLEAR_BIT7 &= 0x7F;
```

```
#define GET_BIT(TO_VAR, FROM_VAR, BIT_NUM)  {
   TO_VAR=FROM_VAR;
   TO_VAR>>=BIT_NUM;
   TO_VAR&=0x01;
}


#define BIT(x)                (1 << (x))

#define SET_BIT(var, mask)    ((var) |= (unsigned char)(mask))
#define CLEAR_BIT(var, mask)  ((var) &= (unsigned char)~(mask))
#define TOGGLE_BIT(var, mask) ((var) ^= (unsigned char)(mask))
#define READ_BIT(var, mask)   ((var) &  (unsigned char)(mask))

#define ASSIGN_BIT(var, val, mask) ((var) = (((var)&~(unsigned
char)(mask))|((val)&(unsigned char)(mask))))

#endif
```

Bibliography

[1] Liu, Y. (2006) *Active Energy Harvesting*, Ph.D. thesis, The Pennsylvania State University.

[2] Tian, G. (2008) *Active Energy Harvesting on Piezoelectric Materials: Experimental Demonstration and Standalone Circuit Implementation*, Master's thesis, The Pennsylvania State University.

[3] Kim, S. and W. W. C. A. Q. Wang (2005) "Piezoelectric Energy Harvesting with a Clamped Circular Plate: Experimental Study," *Journal of Intelligent Material Systems and Structures*, **16**, pp. 855–864.

[4] Joseph, A. D. (2005) "Energy Harvesting Projects," *IEEE Works in Progress*, pp. 69–71.

[5] Chalasani, S. and J. Conrad (2008) "A Survey of Energy Harvesting Sources for Embedded Systems," in *IEEE Southeastcon*, pp. 442–447.

[6] Mitcheson, P. D., E. M. Yeatman, G. K. Rao, A. S. Holmes, and T. C. Green (2001) "Energy Harvesting From Human and Machine Motion for Wireless Electronic Devices," *Proceedings of the IEEE*, **96**(9), pp. 1457–1486.

[7] Pereyma, M. (2007) "Overview of the Modern State of the Vibration Energy Harvesting Devices," in *MEMSTECH*, pp. 107–112.

[8] Niu, P., P. Chapman, R. Riemer, and X. Zhang (2004) "Evaluation of Motions and Actuation Methods for Biomechanical Energy Harvesting," in *IEEE Power Electronics Specialists Conference*, 35th Annual, pp. 2100–2106.

[9] Li, Q., V. Naing, J. Hoffer, D. Weber, A. Kuo, and J. M. Donelan (2008) "Biomechanical Energy Harvesting: Apparatus and Method," in *IEEE International Conference on Robotics and Automation*, pp. 3672–3677.

[10] Taylor, G. W., J. R. Burns, S. M. Kammann, W. B. Powers, and T. R. Welsh (2001) "The Energy Harvesting Eel: A Small Subsurface Ocean/River Power Generator," *IEEE Journal of Oceanic Engineering*, **26**(4), pp. 539–547.

[11] Mateu, L. and F. Moll (2005) "Optimum Piezoelectric Bending Beam Structures for Energy Harvesting using Shoe Inserts," *Journal of Intelligent Material Systems and Structures*, **16**, pp. 835–845.

[12] Priya, S. (2005) "Modeling of Electric Energy Harvesting Using Piezoelectric Windmill," *Applied Physics Letters*, **87**(184101), pp. 1–3.

[13] Vijayaraghavan1, K. and R. Rajamani (2008) "Active Control Based Energy Harvesting for Battery-Less Wireless Traffic Sensors: Theory and Experiments," in *American Control Conference*, pp. 4579–4584.

[14] Elme, J., V. Gaydarzhiev, and A. Mensah (2007) "Maximum Energy Harvesting Control for Oscillating Energy Harvesting Systems," in *IEEE Power Electronics Specialists Conference*, pp. 2792–2798.

[15] Sohn, J. W., S. B. Choi, and D. Y. Lee (2005) "An Investigation on Piezoelectric Energy Harvesting for MEMS Power Sources," in *Proceedings of IMechE*, vol. 219, pp. 429 – 436.

[16] Yuan, D., W. Zhiyu, L. Haiyang, and W. Zhongquan2 (2007) "Power Self-Regulation Circuit of Piezoelectric Multi-Shaker Micro-Generator," in *The Eighth International Conference on Electronic Measurement and Instruments*, vol. 1, pp. 656–660.

[17] Rahimi, M., H. Shah, G. S. Sukhatme, J. Heideman, and D. Estrin (2003) "Studying the Feasibility of Energy Harvesting in a Mobile Sensor Network," in *IEEE International Conference on Robotics and Automation*, vol. 1, pp. 19–24.

[18] Fleming, A. J., S. Behrens, and S. O. R. Moheimani (2003) "An Autonomous Piezoelectric Shunt Damping System," in *Proceedings of SPIE - The International Society for Optical Engineering*, vol. 5052, pp. 207–216.

[19] Lefeuvre, E., A. Badel, L. Petit, C. Richard, and D. Guyomar (2006) "Semi-passive Piezoelectric Structural Damping by Synchronized Switching on Voltage Sources," *Journal of Intelligent Material Systems and Structures*, **17**, pp. 653–659.

[20] Lesieutre, G. A. (1998) "Vibration Damping and Control Using Shunted Piezoelectric Materials," *The Shock and Vibration Digest*, **30**(3), pp. 187–195.

[21] Davis, C. L. and G. A. Lesieutre (2000) "An Actively Tuned Solid-State Vibration Absorber Using Capacitive Shunting of Piezoelectric Stiffness," *Journal of Sound and Vibration*, **232**(3), pp. 601–617.

[22] Liu, Y., K. L. Ren, H. Hofmann, and Q. Zhang (2005) "Investigation of Electrostrictive Polymers for Energy Harvesting," *IEEE Transactions on Ultrasonics, Ferroelectrics, and Frequency Control*, **52**(12), pp. 2411–2417.

[23] Ren, K., Y. Liu, X. Geng, H. F. Hofmann, and Q. Zhang (2006) "Single Crystal PMN-PT/epoxy 1-3 Composite for Energy-harversting Application," *IEEE Transactions on Ultrasonics, Ferroelectrics, and Frequency Control*, **53**(3), pp. 631–637.

[24] Ting, R. Y. and Q. Zhang (2000) "New Electrostrictive PVDF Copolymers for Large-strain Actuator Application," in *Proceedings of SPIE - The International Society for Optical Engineering*, vol. 4073, pp. 48–58.

[25] Vladimir, J. and H. Miroslav (2006) "Electric energy harvesting inside self powered microsystem," in *International Conference on Advanced Semiconductor Devices and Microsystems*, pp. 271–274.

[26] Kim, S., W. W. Clark, and Q. Wang (2003) "Piezoelectric Energy Harvesting Using a Diaphragm Structure," in *The International Society for Optical Engineering*, vol. 5055, pp. 307–318.

[27] Minazara, E., D. Vasic, F. Costa, and G. Poulin (2006) "Piezoelectric Diaphragm for Vibration Energy Harvesting," *Ultrasonics*, **44**, pp. e699–e703.

[28] Yoon, H., G. Washington, and A. Danak (2005) "Modeling, Optimization, and Design of Efficient Initially Curved Piezoceramic Unimorphs for Energy Harvesting Applications," *Journal of Intelligent Material Systems and Structures*, **16**(10), pp. 877–888.

[29] Ericka, M., F. C. Dejan Vasic, and G. Poulain (2005) "Predictive Energy Harvesting from Mechanical Vibration Using a Circular Piezoelectric Membrane," in *IEEE Ultrasonics Symposium*, vol. 2, pp. 946–949.

[30] Kim, H., S. Priya, H. Stephanou, and K. Uchino (2007) "Consideration of Impedance Matching Techniques for Efficient Piezoelectric Energy Harvesting," *IEEE Transactions on Ultrasonics, Ferroelectrics, and Frequency control*, **54**(9), pp. 1851–1859.

[31] Paing, T. S., J. Shin, R. Zane, and Z. Popovic (2008) "Resistor Emulation Approach to Low-Power RF Energy Harvesting," *IEEE Transactions On Power Electronics*, **23**(3), pp. 1494–1501.

[32] Paing, T. S. and R. Zane (2006) "Resistor Emulation Approach to Low-Power Energy Harvesting," in *Power Electronics Specialists Conference*, pp. 1 – 7.

[33] Yen, B. C. and J. H. Lang (2006) "A Variable-Capacitance Vibration-to-Electric Energy Harvester," *IEEE Transactions On Circuits and Systems*, **53**(2), pp. 288–295.

[34] Guan, M. and W. hsin Liao (2008) "Energy Harvesting and Dissipation with Piezoelectric Materials," in *Proceedings of the IEEE International Conference on Information and Automation*, pp. 446–451.

[35] Dallago, E., G. Frattini, D. Miatton, G. Ricotti, and G. Venchi (2007) "Integrable High-Efficiency AC-DC Converter for Piezoelectric Energy Scavenging System," in *IEEE International Conference on Portable Information Devices*, pp. 1–5.

[36] Dallago, E., D. Miatton, G. V. nd G. Frattini, and G. Ricotti (2007) "Self-Supplied Integrable Active High-Efficiency AC-DC Converter for Piezoelectric Energy Scavenging Systems," in *IEEE International Symposium on Circuits and Systems*, pp. 1633–1636.

[37] Ottman, G. K., H. F. Hofmann, A. C. Bhatt, and G. A. Lesieutre (2002) "Adaptive Piezoelectric Energy Harvesting Circuit for Wireless Remote Power Supply," *IEEE Transactions on Power Electronics*, **17**(5), pp. 669–676.

[38] Ottman, G. K., H. F. Hofmann, and G. A. Lesieutre (2002) "Optimized Piezoelectric Energy Harvesting Circuit Using Step-down Converter in Discontinuous Conduction Mode," *PESC Record - IEEE Annual Power Electronics Specialists Conference*, **4**, pp. 1988–1994.

[39] Behrens, S. (2007) "Potential System Efficiencies for MEMS Vibration Energy Harvesting," in *Proceedings of SPIE - The International Society for Optical Engineering*, vol. 6414, pp. 64140D–1 – 64140D–8.

[40] Behrens, S., J. Ward, and J. Davidson (2007) "Adaptive Vibration Energy Harvesting," in *Proceedings of SPIE - The International Society for Optical Engineering*, vol. 6525, pp. 652508–1 – 652508–12.

[41] Scruggs, J. (2009) "An Optimal Stochastic Control Theory for Distributed Energy Harvesting Networks," *Journal of Soundand and Vibration*, **320**, pp. 707–725.

[42] Gnad, G. and R. Kasper (2004) "A Power Drive Control for Piezoelectric Actuators," in *IEEE International Symposium on Industrial Electronics*, vol. 2, pp. 963–967.

[43] Badel, A., A. Benayad, E. Lefeuvre, L. Lebrun, C. Richard, and D. Guyomar (2006) "Single Crystals and Nonlinear Process for Outstanding Vibration-Powered Electrical Generators," *IEEE Transactions on Ultrasonics, Ferroelectrics, and Frequency Control*, **53**(4), pp. 673–684.

[44] Guyomar, D., A. Badel, E. Lefeuvre, and C. Richard (2005) "Towards Energy Harvesting Using Active Materials and Conversion Improvement by Nonlinear Processing," *IEEE Transactions on Ultrasonics, Ferroelectrics, and Frequency Control*, **52**(4), pp. 584–595.

[45] Hu, Y., H. Xue, T. Hu, and H. Hu (2008) "Nonlinear Interface Between the Piezoelectric Harvesting Structure and the Modulating Circuit of an Energy Harvester with a Real Storage Battery," *IEEE Transactions on Ultrasonics, Ferroelectrics, and Frequency Control*, **55**(1), pp. 148–160.

[46] Lefeuvre, E., A. Badel, A. Benayad, L. Lebrun, C. Richard, and D. Guyomar (2005) "A Comparison Between Several Approaches of Piezoelectric Energy Harvesting," *Journa of Physics IV France*, pp. 177–186.

[47] Mehraeen, S., S. Jagannathan, and K. Corzine (2008) "Energy Harvesting Using Piezoelectric Materials and High Voltage Scavenging Circuitry," in *IEEE International Conference on Industrial Technology*, pp. 1–8.

[48] Lallart, M., L. Garbuio, L. Petit, C. Richard, and D. Guyomar (2008) "Double Synchronized Switch Harvesting (DSSH): A New Energy Harvesting Scheme for Efficient Energy Extraction," *IEEE Transactions on Ultrasonics, Ferroelectrics, and Frequency Control*, **55**(10), pp. 2119–2130.

[49] Liu, Y., G. Tian, Y. Wang, J. Lin, Q. Zhang, and H. F. Hofmann (2008) "Active Piezoelectric Energy Harvesting: General Principle and Experimental Demonstration," *Journal of Intelligent Material Systems and Structures, accepted*.

[50] Guan, M. and W. hsin Liao (2006) "On the Energy Storage Devices in Piezoelectric Energy Harvesting," in *Proceedings of SPIE*, vol. 6269, pp. 1–9.

[51] "IEEE standard on piezoelectricity 29 Jan 1988," .

[52] Priya, S. and D. J. Inman (2009) *Energy Harvesting Technologies*, 1 ed., Springer Inc.

[53] Mohan, Undeland, and Robins (2003) *Power Electronics: Converters, Applications, and Design*, 3 ed., John Wiley & Sons Inc.

[54] W.Erickson, R. and D. Maksimovie (2001) *Fundamentals of Power Electronics*, 2 ed., Kluwer Academic Publishers.

[55] Sun, J., D. M. Mitchell, M. F. Greuel, and R. Bass (2001) "Modeling of PWM Converters in Discontinuous Conduction Mode - A Reexamination," *IEEE Transactions on Power Electronics*, **16**, pp. 482–492.

[56] X.Zhou, T. Wang, and F. C. Lee (1997) "Optimizing Design for Low Voltage DC-DC Converters," in *Applied Power Electronics Conference and Exposition*, vol. 2 of *Twelfth Annual*, pp. 612–621.

[57] Ward, J. K. and S. Behrens (2008) "Adaptive Learning Algorithms for Vibration Energy Harvesting," *Smart Materials and Structures*, **17**, pp. 1–9.

[58] Shu, Y. C. and I. C. Lien (2006) "Analysis of power output for piezoelectric energy harvesting systems," *Smart Material and Structures*, **15**, pp. 1499–1512.

[59] Shu, Y. C., I. C. Lien, and W. J. Wu (2007) "An improved analysis of the SSHI interface in piezoelectric energy harvesting," *Smart Material and Structures*, **16**, pp. 2253–2264.

[60] Shu, Y. C. and I. C. Lien (2006) "An improved analysis of the SSHI interface in piezoelectric energy harvesting," *Journal of Micromechanics and Microengineering*, **16**, pp. 2429–2438.

[61] Polak, E. (1997) *Optimization: Algorithms and Consistent Approximations*, 1 ed., Springer Inc.

[62] Hofmann, H. F., S. R. Sanders, and A. EL-Antably (2004) "Stator-Flux-Oriented Vector Control of Synchronous Reluctance Machines With Maximized Efficiency," *IEEE Transactions on Industrial Electronics*, **51**(5), pp. 1066–1072.

Vita

Cheng Luo

Education

- Ph. D. Candidate, Electrical Engineering
  GPA: 3.93/4.0, The Pennsylvania State University, August 2006 to May 2010
- Mater of Science, Electrical Engineering
  GPA: 3.80/4.0, Tsinghua University, September 2003 to January 2006
- Bachelor of Science, Electrical Engineering
  GPA: 3.60/4.0, Tsinghua University, September 1999 to July 2003

Publications

- Cheng Luo, Matthew Whitehead, and Heath Hofmann, "Design and testing of a power electronic synthetic inductor", International Journal of Electronics, vol. 96, issue 12, pp. 1249-1264, 2009.
- Guanghui Wang, Cheng Luo, Lawrence Rome, and Heath Hofmann, "Power Electronic Circuitry for Energy Harvesting Backpack", Proceedings of ECCE 2009, San Jose CA, USA, SEP 2009.
- Cheng Luo, Matthew Whitehead, and Heath Hofmann, "Design and testing of a power electronic synthetic inductor", Proceedings of the Power Electronics Specialists Conference 2007 (PESC 2007), Orlando Fl, USA, JUN 2007.
- Cheng Luo, Xiangheng Wang, and Puqi Ning, "Analyzing and calculation of the loss in the rotor of a twelve-phase high-speed asynchronous generator", Journal of Tsinghua University (Sci and Tech), JAN 2006.
- Cheng Luo, Xiangheng Wang, and Puqi Ning, "The analysis of stator mmf and the calculation of rotor losses in a 12-phase high speed asynchronous generator", Proceedings of the 8th ICEMS, Nanjing Jiangsu, China, SEP 2005.
- Xinzhen Wu, Xiangheng Wang, and Cheng Luo, "Induction machine losses in rotor bar flowing through non-sinusoidal currents", Proceedings of the CSEE, SEP 2005.
- Xinzhen Wu, Xiangheng Wang and Cheng Luo, "Relationship between harmonic currents and corresponding harmonic magneto-motive forces of multiphase induction machines", Journal of Tsinghua University (Sci and Tech), JUL 2005.